

Granular Crystals: Controlling Mechanical Energy with Nonlinearity and Discreteness

Thesis by

Nicholas Sebastian Boechler

In Partial Fulfillment of the Requirements

for the Degree of

Doctor of Philosophy



California Institute of Technology

Pasadena, California

2011

(Defended April 22, 2011)

To my family and friends.

Acknowledgements

I would like to acknowledge and thank my advisor, Chiara Daraio. She gave me a chance, and made everything I have done in my graduate research possible. I have learned so many things in my time spent working for her. She always gave guidance when needed, listened to my ideas, and gave me great freedom and support in my research. I greatly appreciate it all.

I thank the members of my thesis committee: Guruswami Ravichandran, Michael Cross, Sergio Pellegrino, and Oskar Painter. Professor Ravichandran, thank you for all your guidance and perspective. I also thank the members of my candidacy committee: Greg Davis, Michael Ortiz, and Kaushik Bhattacharya.

With much love, I thank my my mom, my brother, and my dad, who always have been supportive in all my endeavours. I thank my mom for being Mom, and for reading articles in the Washington Post with me on buckyballs when I was in elementary school. I also thank Uncle Brian and Aunt Rachel: I glad we have recently had the chance to spend more time together.

To Peony Liu, you have been the best part of my time in LA, and I feel so incredibly lucky to have met you.

To Giorgos Theocharis, I do not think I can thank you enough. You have been like a brother to me, and have been an incredible collaborator, teacher, and friend.

I thank the friends that have been with me since high school: Chris Hannemann, Elizabeth Deems, Lindsay Claiborn, Nick Saldivar, and Scott Breunig. Somehow we have managed to stick together for this long. Chris, you are the best friend a person could ask for. Scott, I appreciate you taking the road trip and the Alaska trip when I needed it most. You all are my friends for life.

My deepest gratitude goes to my best friends at Caltech: Jon Mihaly, Mumu Xu, Andrew Richards, and Ian Jacobi. I would not have made it through the masters year without you. Jon, you have been an amazing friend and roommate. Mumu, I secretly do find your jokes humorous. Andy, thanks for always making the time to help everyone. Ian, I would not have passed quals without you, and I appreciate all the “Nick-safe” baked goods.

I thank my mentors from TJ and GT: Mr. Buxton, John Olds, Narayanan Komerath. Mr. Buxton, the skills I learned in all those hours in the prototyping lab have proven immensely valuable. Dr. Olds, thank you for giving me a chance to work at SpaceWorks Engineering while at Georgia Tech. I can not say how much I enjoyed my time there and how much I learned from you. Professor Komerath, I thank you for teaching me to not care what other people think, and for giving me the opportunity to dream of space solar power.

I thank my collaborators: Panayotis Kevrekidis, Mason Porter, Stephane Job, Andrew Shapiro, Peter Dillon, and Yan Man. Panos, I greatly appreciate your support, collaboration, and mentorship. Stephane, you are a great experimentalist, and I am forever grateful that I had the opportunity to learn from you. I thank my friends from Italy: Fernando Fraternali, Ada Amendola, Rossella Hobbes, Angelo Esposito, and Vincenzo Cianca. Fernando, thank you for giving me the opportunity to visit Salerno. Ada, thank you for introducing your family; that was the best part of an already wonderful trip.

A big thank you and jiayou goes to the folks at UCLA Wushu and LA Wushu, Chuck Hwong, and John Nguyen. I am so appreciative of how you took me in when I first came to LA. I thank my officemates and the Daraio lab group members, in particular: Ivan Szelengowicz, Andrea Leonard, Sebastian Liska, Duc Ngo, and Stephane Griffiths. I thank my friends from GT: Jason Pollan, Jonathan Marsh, Sam Fielden, Christy Fielden, Marianna Jewell, Jessica Jackson, Catherine Matthews, Fabian Mak, and the GT Wushu club members. I wish I could see you all more often. I thank all my friends at Caltech not yet mentioned: Francisco Lopez Jimenez, Francisco Montero, Nick Parziale, Olive Stohlman, Noel Du Toit, Leslie Lamberson, Phil Boettcher,

Jeff Lehew, Kawai Kwok, Vahe Gabuchian, Mike Mello, and anyone else that I am forgetting at the moment. I thank Mike and Vahe for their help with the laser vibrometer. Last but not least, I thank Joe Haggerty, Brad St. John, and Ali Kiani, Linda Miranda, Christine Ramirez, and Jennifer Stevenson for always coming through for me when I needed your help.

Abstract

The presence of structural discreteness and periodicity can affect the propagation of phonons, sound, and other mechanical waves. A fundamental property of many of the periodic structures and materials designed for this purpose is the presence of complete band gaps in their dispersion relation. Waves with frequencies in the band gap cannot propagate and are reflected by the material. Like the concept of a band gap, the functionality of these periodic structures has historically been based on concepts from linear dynamics. Nonlinear systems can offer increased flexibility over linear systems including new ways to localize energy, convert energy between frequencies, and tune the response of the system. Granular crystals are arrays of elastic particles that interact nonlinearly via Hertzian contact, and are a type of nonlinear periodic structure whose response to dynamic excitations can be tuned to encompass linear, weakly nonlinear, and strongly nonlinear regimes. Drawing on ideas from condensed matter physics and nonlinear science, this thesis focuses on how the nonlinearity and structural discreteness of granular crystals can be used to control mechanical energy. The dynamic response of one-dimensional granular crystals composed of compressed elastic spheres (or cylinders) is studied using a combination of experimental, numerical, and analytical techniques. The discovery of fundamental physical phenomena occurring in the linear and weakly nonlinear regimes is described, along with how such phenomena can be used to create new ways to control the propagation of mechanical wave energy. The specific mechanisms investigated include tunable frequency band gaps, discrete breathers, nonlinear localized defect modes, and bifurcations. These mechanisms are utilized to create novel devices for tunable vibration filtering, energy harvesting and conversion, and tunable acoustic rectification.

Contents

Acknowledgements	ii
Abstract	v
Contents	vi
List of Figures	x
List of Tables	xix
1 Introduction	1
1.1 Motivation	1
1.2 Significance of This Work	3
1.3 Wave Propagation in Periodic Structures	4
1.4 Periodic Phononic Structures	5
1.5 Nonlinear Lattices	8
1.6 Disorder in Periodic Structures	10
1.7 Granular Crystals	11
1.7.1 Granular Crystals Brief Historical Review	12
1.7.2 One-Dimensional Granular Crystals	15
1.7.3 Weakly Nonlinear Granular Crystal	17
1.7.4 Linear Granular Crystal	18
1.8 Experimental Setup	18
1.8.1 In-Situ Piezoelectric Sensors	21
1.8.2 Piezoelectric Actuator	24

1.8.3	Data Acquisition and Sampling	25
1.8.4	Data Analysis and Post Processing Tools	26
1.8.5	Boundary Conditions and Static Load Application and Measurement	27
1.8.6	Experimental Procedure	29
1.9	Numerical Tools	32
1.10	Conceptual Organization of This Thesis	33
2	Tunable Band Gaps in Diatomic Granular Crystals with Three-Particle Unit Cells	35
2.1	Introduction	35
2.2	Experimental Setup	37
2.3	Theoretical Discussion	39
2.3.1	Dispersion Relation	39
2.3.2	State-space Approach	43
2.4	Experimental Linear Spectrum	47
2.5	Conclusions	51
2.6	Author Contributions	52
3	Discrete Breathers in Diatomic Granular Crystals	53
3.1	Introduction	53
3.2	Experimental Setup	54
3.3	Theoretical Model	55
3.4	Linear Spectrum	56
3.5	Modulational Instability and DBs	57
3.6	Exact Solutions and Stability of DBs	59
3.7	Experimental Observation of DBs	60
3.8	Conclusions	62
3.9	Author Contributions	63

4	Existence and Stability of Discrete Breather Families in Diatomic Granular Crystals	64
4.1	Introduction	65
4.2	Theoretical Setup	67
4.2.1	Equations of Motion and Energetics	67
4.2.2	Weakly Nonlinear Diatomic Chain	68
4.2.3	Linear Diatomic Chain	69
4.2.4	Experimental Determination of Parameters	70
4.3	Overview of DGB	72
4.3.1	Methodology	72
4.3.2	Families of DGBs	72
4.3.3	Stability Overview	74
4.4	Four Regimes of DGB: Existence and Stability	76
4.4.1	Overview of Four Dynamical Regimes	76
4.4.2	Region (I): Close to the Optical Band ($f_b \lesssim f_2$)	78
4.4.3	Region (II): Moderately Discrete Regime	79
4.4.3.1	HS Discrete Gap Breather (HS-DGB)	80
4.4.3.2	LA Discrete Gap Breather (LA-DGB)	81
4.4.4	Region (III): Strongly Discrete Regime ($f_1 \ll f_b \ll f_2$)	85
4.4.5	Region (IV): Close to and Slightly Inside the Acoustic Band	88
4.5	Conclusions	90
4.6	Author Contributions	91
5	Defect Modes in Granular Crystals	92
5.1	Introduction	92
5.2	Experimental Setup	93
5.3	Theoretical Model	94
5.4	Single Defect: Near-Linear Regime	96
5.5	Two Defects: Near-Linear Regime	100
5.6	Single Defect: Nonlinear Localized Modes	102

5.7	Conclusions	104
5.8	Author Contributions	106
6	Bifurcation-Based Acoustic Switching and Rectification	107
6.1	Introduction	108
6.2	Rectifier Concept	109
6.3	Bifurcations	110
6.4	Experimental Response and Power Spectra	111
6.5	Experimental Rectifier Tunability	112
6.6	Numerical Modeling	114
6.7	Conclusions	114
6.8	Methods	116
6.8.1	Experimental Setup	116
6.8.2	Model	116
6.9	Supplementary Information	117
6.9.1	Experimental Measurement of Linear Spectra	117
6.9.2	Quasiperiodic Vibrations	118
6.9.3	Route to Chaos	119
6.9.4	Logic	121
6.10	Author Contributions	122
7	Conclusion	123
	Bibliography	126

List of Figures

1.1	Phononic crystals. (left) Macroscopic sonic phononic crystal and sculpture by Eusebio Sempere, Madrid [1]. (right) One-dimensional hyper-sonic phononic crystal [2].	7
1.2	1D granular crystal composed of 19.05 mm diameter steel and aluminium spheres.	11
1.3	Schematic of experimental setup. Red (light gray) arrows denote direction of data flow.	19
1.4	In-situ piezoelectric sensor. (a) Photograph of sensor. (b) Schematic of sensor. (c) Sensitivity range. Frequency f_r is the resonant frequency of the assembled sensor. f_τ is the discharge time frequency of the sensor. (d) Sensor calibration setup schematic. The actuator applies a low frequency dynamic signal, above f_τ and significantly below the resonant frequency of the calibration setup (including motion of the bead). . . .	22
2.1	(a) Schematic of experimental setup. (b) Schematic of the linearized model of the experimental setup.	38

- 2.2 (a) Dispersion relation for the described sphere-cylinder-sphere granular crystal with cylinder length $L = 12.5$ mm ($M = 27.3$ g) subject to an $F_0 = 20$ N static load. The acoustic branch is the dashed line, the lower optical branch is the solid line, and the upper optical branch is the dash-dotted line. Cutoff frequencies for granular crystals corresponding to our experimental configuration (b) varying the length L (and thus mass) of the cylinder with fixed $F_0=20$ N static compression, and (c) varying the static compression ($F_0 = [20, 25, 30, 35, 40]$ N) with fixed $L = 12.5$ mm cylinder length ($M = 27.3$ g). Solid lines represent the six cutoff frequency solutions. $f_{c,2}$ is dashed to clarify the nature of the intersection with $f_{c,3}$. Shaded areas are the propagating bands. 42
- 2.3 Bode transfer function ($|H(i\omega)|$) for the experimental configurations: (a) the five diatomic (three-particle unit cell) granular crystals with varied cylinder length for fixed $F_0 = 20$ N static compression, and (b) the fixed cylinder length $L = 12.5$ mm ($M = 27.3$ g) granular crystal with varied static load. Solid white lines are the cutoff frequencies calculated from the dispersion relation of the infinite system. The black arrows in (a) denote the eigenfrequencies of defect modes. 47
- 2.4 Experimental transfer function for the $L = 12.5$ mm ($M = 27.3$ g), $F_0 = 20$ N granular crystal. The horizontal dashed line is the -10 dB level used to experimentally determine the $f_{c,2}$ and $f_{c,3}$ band edges which are denoted by the vertical dashed lines. 48
- 2.5 Experimental PSD transfer functions for the experimental configurations described in figure 2.3. (a) The five diatomic (three-particle unit cell) granular crystals with varied cylinder length for fixed $F_0=20$ N static compression, and (b) the fixed cylinder length $L = 12.5$ mm ($M = 27.3$ g) granular crystal with varied static load. Solid white lines are the cutoff frequencies from the dispersion relation using experimentally determined Hertz contact coefficients $A_{1,exp}$ and $A_{2,exp}$ 50

3.1	Top panel: Experimental setup. Bottom panel: Experimental phonon spectrum of the 81-bead steel-aluminum diatomic crystal. The horizontal line designates half of the low frequency mean value, and vertical lines indicate the f_n^{exp} cutoff frequencies given in Table 3.1.	56
3.2	(a1) Spatiotemporal evolution of the forces for the simulated manifestation of the MI and DB generation with particle initial conditions corresponding to the lower optical cutoff mode. (a2) Force versus time for particle 40 for the simulation shown in (a1). (b1) Spatiotemporal evolution of the forces for the generation of a DB under conditions relevant to our experimental setup. (b2) PSD of particle 36 for the simulation shown in (b1). The dashed line in (b2) indicates the driving frequency $f_{\text{act}} = f_2^{\text{exp}}$, and the arrow indicates the DB frequency $f_b \simeq 8.14 \text{ kHz} < f_2^{\text{exp}}$	59
3.3	Bifurcation diagram of the continuation of the DB solutions. (a) Maximal dynamic force of the wave versus frequency f_b . The insets show spatial profiles at two values of f_b . (b) Maximal deviation of Floquet multipliers from the unit circle, which indicates the instability growth strength. The right inset shows a typical multiplier picture, and the left inset shows the connection between the strong (real multiplier) instability and the change in sign of dE/df_b	61
3.4	Experimental observations of MI and DB at $f_b^{\text{exp}} \simeq 8.28 \text{ kHz}$, with $f_1^{\text{exp}} < f_b^{\text{exp}} < f_2^{\text{exp}}$, while driving the chain at $8.90 \text{ kHz} \simeq f_2^{\text{exp}}$ (see Table 3.1) for 90 ms. (a1, a2) Forces versus time and (b1, b2) PSDs at particles 2 and 14. Normalized power versus lattice site at the driving (open symbols) and the DB (filled symbols) frequencies, before (c1) and after (c2) DB formation. Vertical lines in (b) mark the driving frequency and the DB frequency. Blue (red) curves in (a, b, c) refer to time regions of 30 ms before (after) the DB formation, while the black curves refer to the entire signal.	62

4.1	Schematic of the diatomic granular chain. Light gray represents aluminum beads, and dark gray represents stainless steel beads.	69
4.2	Energy of the two families of discrete gap breathers (DGBs) as a function of their frequency f_b . The inset shows a typical example of the energy density profile of each of the two modes at $f_b = 8000$ Hz.	71
4.3	Magnitude of the Floquet multipliers as a function of DGB frequency f_b for the DGB with a light centered-asymmetric energy distribution (LA-DGB; left panel) and for the DGB with a heavy-centered symmetric energy distribution (HS-DGB; right panel).	75
4.4	Top panels: Four typical examples of the relative displacement profile of LA-DGB solutions, each one from a different dynamical regime. Bottom panels: As with the top panels, but for HS-DGB solutions.	77
4.5	(a) Spatial profile of an HS-DGB with frequency $f_b = 8600$ Hz. (b) Corresponding locations of Floquet multipliers λ_j in the complex plane. We show the unit circle to guide the eye. Displacement (c) and velocity components (d) of the Floquet eigenvectors associated with the real instability.	81
4.6	Spatiotemporal evolution (and transformation into $f_b \approx 7900$ Hz LA-DGB) of the displacements of a HS-DGB summed with the pinning mode and initial $f_b = 8600$ Hz. Inset: Fourier transform of the center particle.	82
4.7	(a) Spatial profile of an LA-DGB with frequency $f_b = 8600$ Hz. (b) Corresponding locations of Floquet multipliers λ_j in the complex plane. We show the unit circle to guide the eye. Displacement (c) and velocity (d) components of the Floquet eigenvector associated with the real instability.	83

- 4.8 Spatiotemporal evolution of the displacements of a LA-DGB with $f_b = 8600$ Hz when one (a) adds and (b) subtracts the unstable localized mode depicted in figure 4.7(c). Panel (c) shows the Fourier transform of the center particle for case (a), and panel (d) shows the same for case (b). In panels (c,d), the two vertical lines enclose the regime of the frequencies in which the LA-DGB exhibits the strong real instability. 84
- 4.9 Top panels: Spatial profile of an HS-DGB with frequency $f_b = 7210$ Hz at $t = 0$ (a) and at $t = T/2$ (b). Bottom panels: As with the top panels, but for LA-DGB solutions. The dashed curves correspond to the spatial profile of the surface mode obtained using equations (4.9,4.10). In each panel, we include a visualization of particle positions, and gap openings, for the corresponding time and DGB solution. 87
- 4.10 (a) Spatial profile of an HS-DGB with frequency $f_b = 5500$ Hz. (b) Corresponding locations of Floquet multipliers λ_j in the complex plane. We show the unit circle to guide the eye. (c) Displacement and (d) velocity components of the Floquet eigenvectors associated with the second real instability (which, as described in the text, is a subharmonic instability). 88
- 4.11 Spatial profile of a LA-DGB (a) and an HS-DGB (b) with frequency $f_b = 5210$ Hz. (c,d) Continuation of the DGBs into their discrete out gap siblings as the frequency crosses the upper end of the acoustic band (denoted by dashed lines). The delocalization of the solution profile as the upper acoustic band edge is crossed is evident for both the LA-DGB solutions (c) and the HS-DGB solutions (d). 90

5.1 a) Schematic diagram of the experimental setup for the homogeneous chain with a single defect configuration. b) Experimental transfer functions (as defined in the “single-defect: near linear regime” section) for a granular crystal with a static load of $F_0 = 20$ N and a defect-bead of mass $m = 5.73$ g located at site $n_{def} = 2$. Blue (dark-grey) [red (light-grey)] curves corresponds to transfer function obtained from the force signal of a sensor particle placed at $n = 4$ [$n = 20$]. The diamond marker is the defect mode. The triangle marker is the upper acoustic cutoff mode. The vertical black dashed line is the theoretically predicted defect mode frequency, and the vertical solid black line is the theoretically predicted upper acoustic cutoff frequency. 95

5.2 Frequency of the defect mode, with defect-bead placed at $n_{def} = 2$, as a function of mass ratio m/M . Solid blue line (dark grey, closed diamonds) corresponds to experiments, solid black line (open diamonds) to numerically obtained eigenfrequencies (see equation (5.3)), and green dashed line (light grey, x markers) to the analytical prediction of the three-beads approximation (see equation (5.4)). The error bars account for statistical errors on the measured frequencies and are $\pm 2\sigma$. Inset: The normalized defect mode for $\frac{m}{M} = 0.2$ 99

5.3 (a) Experimental transfer functions for a granular crystal with two defect-beads of mass ratio $\frac{m}{M} = 0.2$ at $n_{def} = 2$ and $n_{def} = 3$ (in contact). Blue (dark grey) [red (light grey)] curve corresponds to transfer function obtained from the force signal of a custom sensor placed at $n = 4$ [$n = 20$]. (b) Frequencies of the defect modes as a function of the distance between them. The solid line denotes experimental data, the dashed line the numerically obtained eigenfrequencies, and the x markers the frequencies from the analytical expressions of equations (5.5)- (5.6). (c),(d) The normalized defect mode shapes corresponding to the defect modes identified in (a) with frequency of the same marker type. 102

- 5.4 (a) Numerical frequency continuation of the nonlinear defect modes corresponding to the experimental setup in figure 5.1(a). (b) Numerically calculated spatial profile of the nonlinear localized mode with frequency $f_{def} = 13.28$ kHz. (c) Measured force-time history of a sensor at site $n = 3$, where a high amplitude, short width, force pulse is applied to the granular crystal. (d) Normalized PSD for the measured time regions of the same color in (c); closed and open diamonds correspond to the high and low amplitude time regions respectively. The vertical dashed line is the mean experimentally determined linear defect mode frequency. . . . 105
- 6.1 Schematics and conceptual diagrams. (a,b) Schematics of the granular crystal used in experiments, composed of 19 stainless steel spherical particles, a light mass defect, and applied static load F_0 . Vertical lines in the spheres indicate the sensor particles. (c,d) Conceptual diagrams of the rectification mechanism. f_d is the defect frequency, f_c is the acoustic (pass) band cutoff frequency, and f_{dr} is the driving frequency. (a,c) Reverse configuration: driving far from the defect, the bad gap filters out vibrations at frequencies in the gap (f_{dr}). (b,d) Forward configuration: driving near the defect, nonlinear modes are generated which transmit through the system. 110

- 6.2 Bifurcation and stability. Maximum dynamic force at the fourth particle from the actuator in the forward configuration as a function of driving amplitude δ (i.e. the actuator displacement). Red square markers are experimental data corresponding to the ($f_{dr} = 10.5$ kHz, $F_0 = 8$ N) configuration shown in figures 6.3 and 6.4. Error bars are based on the range of actuator calibration values. The solid blue (dashed black) line corresponds to the numerically calculated stable (unstable) periodic branches. The dotted blue line corresponds to the numerically calculated quasiperiodic branch. Green arrows denote the path (and jump) followed with increasing driving amplitude. The circled numbers correspond to bifurcation points. 111
- 6.3 Experimental force-time response and power spectra. (a-f) Forward configuration. (g,h) Reverse configuration. (a,c,e,g) Experimentally measured force-time history for the sensor four particles from the actuator ($f_d = 10.5$ kHz, varied amplitudes/configurations). The blue (dark grey) is the time region used to calculate the PSDs. (b,d,f,h) PSD of the measured force-time history for the sensors four (blue [dark grey]) and 19 particles from the actuator (red [light grey]). The vertical black solid line is the upper acoustic band cutoff frequency f_c , the black dashed line the defect mode frequency f_d , and the green (light grey) line the driving frequency f_{dr} 113
- 6.4 Power transmission and energy distribution. (a) Experimental and (b) numerical average transmitted power as a function of driving amplitude δ . The black curve corresponds to $F_0 = 8.0$ N ($f_{dr} = 10.5$ kHz) and the red (light grey) curve to $F_0 = 13.9$ N ($f_{dr} = 11.4$ kHz). Positive/negative displacements denote forward/reverse configurations, respectively. The horizontal black dashed line in (b) is the experimental noise floor. Numerical time-averaged energy density as a function of position for the (c) reverse and (d) forward configurations. (c,d) each curve corresponds to the configuration/amplitude of the same maker type in (b). 115

6.5	Experimentally measured PSD transfer functions. PSD transfer function for the granular crystal rectifiers of figures 6.1-6.4 ($F_0 = 8$ N) in the (a) reverse and (b) forward configurations. Blue (dark grey) curve is the sensor located four particles from the actuator, red (light grey) is the sensor 19 particles from the actuator (corresponding to the sensors of the same color in figure 6.1a,b, respectively). The vertical black line is the acoustic band upper cutoff frequency f_c , and the vertical black dashed line is the defect mode frequency f_d	118
6.6	Quasiperiodic vibrations. (a) Floquet spectrum of the periodic solution corresponding to $f_{dr} = 10.5$ kHz and $\delta_{(+)} = 0.6$ μm . (b) Numerically calculated force-time history of the fourth particle away from the actuator in the forward configuration, using as an initial condition the periodic solution of panel (a). (c) PSD of the blue (dark grey) time region of panel (b).	119
6.7	The period doubling cascade route to chaos. PSD of the numerically calculated force-time history, corresponding to driving amplitudes $\delta_{(+)} = 0.6$ μm (a), $\delta_{(+)} = 1$ μm (b), $\delta_{(+)} = 1.03$ μm (c) and $\delta_{(+)} = 1.2$ μm (d) for the fourth particle from the actuator in the forward configuration.	120
6.8	Mechanical logic devices based on the tunable rectifier. Incident signals are applied through A and B, and received in C. (a) AND gate. Signals will only pass when combined amplitudes of A and B are greater than the critical rectifier amplitude δ_c . (b) OR gate. Signals will pass when either the amplitude of A or B are greater than the critical rectifier amplitude.	121

List of Tables

2.1	Hertz contact coefficients derived from standard specifications [3] (A_1 and A_2) versus coefficients derived from the measured frequency cutoffs ($A_{1,\text{exp}}$ and $A_{2,\text{exp}}$), for the ($F_0 = [20, 25, 30, 35, 40]$ N) fixed cylinder length $L = 12.5$ mm ($M = 27.3$ g) granular crystals.	49
3.1	Predicted (from standard specifications [3, 4]) versus measured cutoff frequencies, linear stiffness K_2 , and coefficient A under a static precompression of $F_0 = 20$ N.	57
4.1	Calculated cutoff frequencies (based on the experimentally obtained coefficient A [5]) under a static compression of $F_0 = 20$ N.	71
4.2	Characteristics of the DGBs in the four different regimes.	77

Chapter 1

Introduction

This thesis describes several new ways to control mechanical energy utilizing the discreteness and nonlinearity of granular crystal systems. We focus on one-dimensional (1D) statically compressed granular crystals composed of macroscopic spheres (or cylinders) of up to two particle types (diatomic). This introduction briefly describes the motivation and historical setting for this research, some of the experimental, theoretical, and conceptual elements common to each of these projects, the significance of this work, and the organization of the thesis.

1.1 Motivation

Mechanical waves are prevalent in everyday life and in most engineering applications. For instance, the pressure wave that causes the sounds that you hear, or the stress waves that cause the vibration of machinery, are all examples of mechanical waves. Accordingly, the study of mechanical waves and the ability to control them is very important for engineering applications.

Mechanical waves take many forms depending on the media they travel through (acoustic waves in fluids or elastic waves in solids) and the wavelength and frequency of the waves. Mechanical waves can be roughly categorized based on their frequency, this includes sonic (less than 20 kHz) waves, ultrasonic (20 kHz to 500 MHz frequencies) waves, and hypersonic (500 MHz to 10 THz) waves [6, 7]. Generally, the wavelength and frequency of the waves are inversely related to each other (though the exact

relationship depends on the media that they are traveling through, for instance if the waves are traveling in a nonlinear or a dispersive medium). Thus waves at very high frequencies have characteristically small wavelengths.

Some examples at macroscopic wavelengths and near-sonic frequencies include sound waves traveling through air and structural vibrations in engineering devices. Some of the most common ways to control macroscale mechanical waves and vibrations include viscous dampers, dissipative foams, tuned mass dampers [8], and active control loops [9]. Increasing the frequency and decreasing the wavelength to micro- and nanoscales includes ultrasonic waves, and hypersonic waves characteristic of thermal phonons (quantized lattice vibrations—the elastic/vibrational analog to photons of light) [6, 7, 10]. Accordingly, macroscopic mechanical waves are also connected to heat transfer through nanoscale mechanical lattice waves and the propagation of phonons in dielectric solids (although there are other mechanisms as well, such as electron conduction in metallic solids and random thermal motion in fluids) [10, 11]. Some of the most common ways to control heat transfer include combinations of insulating dielectric materials/or conductors (depending on the application), and radiative and convective devices such as heat sinks and fans [11].

An alternative approach to control mechanical wave propagation is with dispersion induced by structural discreteness and periodicity [12, 13]. Generally, waves with wavelengths on the order of the length scale of the structural periodicity feel the structure, and their propagation is affected by dispersion [12, 13]. Many periodic structures have thus been designed for the purpose of controlling the propagation of mechanical waves [6, 7, 13, 14]. A fundamental property of many of these periodic structures is the presence of complete band gaps in their dispersion relation, where waves with frequencies in the band gap cannot propagate and are reflected by the material. However, like the concept of a band gap, the functionality of these periodic structures has historically been based on concepts from linear dynamics [6, 13, 14]. As an alternative, nonlinear systems can offer increased flexibility over linear systems, including new ways to localize energy, convert energy between frequencies, and tune the response of the system [15–21].

In this thesis we study granular crystals, which are arrays of macroscopic elastic particles that interact nonlinearly via Hertzian contact [21]. These granular crystals are a type of nonlinear periodic structure whose response to dynamic excitations can be tuned to encompass linear, weakly nonlinear, and strongly nonlinear regimes [21, 22]. As granular crystals are discrete and periodic systems, they can control and affect the propagation of mechanical waves in a similar way to the previously described periodic structures. However, because the system is also nonlinear, there are many new unexplored ways to control the propagation of mechanical waves, in contrast to simple linear band gaps. Because the scale of the granular crystal system is macroscopic, we are concerned with controlling the propagation of mechanical waves with macroscopic wavelengths at sonic frequencies, such as acoustic waves or structural vibrations. With the granular system, we explore new ways to control mechanical waves at sonic frequencies, including tunable frequency band gaps, energy localization, and rectification. Simultaneously, because the elements of periodicity, discreteness, and nonlinearity are universal to many systems, we are studying fundamental phenomena in nonlinear discrete systems, that could be applied to a wide range of other settings.

1.2 Significance of This Work

With this work, we describe new ways to control mechanical energy utilizing the discreteness, periodicity, and nonlinearity present in granular crystals. This includes new ways to engineer the dispersion relation of granular crystals to provide more tunable vibration filtering capabilities, localize energy for energy harvesting applications, and create direction dependent energy flows for energy harvesting, sensing, and logic devices. We present the discovery of phenomena previously unknown to occur in granular crystals, such as discrete breathers and tunable band gaps with up to three pass bands. We provide greater understanding through systematic characterization of such phenomena, including the existence and stability of discrete breathers families, and the behavior and interplay of defects in granular crystal systems. We

also present the discovery of more generally new phenomena (not previously demonstrated in other systems), which was enabled by the type of nonlinearity occurring in granular crystals, such as a tunable phononic rectification based on bifurcations with a bistable transition involving quasi-periodic and chaotic states. The discovery and characterization of such phenomena will aid in the development of practical granular crystal-based devices, for use in vibration filtering and energy harvesting applications. Additionally, the ideas explored here for this prototypical setting could in the future be applied to more complex settings (higher degree of freedom granular crystal systems, other discrete nonlinear systems) and systems of different length scales. Because nonlinearity and discreteness are common elements to many dynamical systems, we also foresee that the phenomena described here could eventually be applied to other photonic and phononic systems.

1.3 Wave Propagation in Periodic Structures

Periodic structures have long been known to affect the propagation of many different types of waves [13]. This is a universal concept for many different types of waves, including matter, electromagnetic, and mechanical waves [13]. Generally, waves with wavelengths on the order of the length scale of the structural periodicity feel the structure, and their propagation is affected by dispersion [12, 13]. Waves in dispersive systems travel at different speeds depending on the wavelength (this is described by group and phase velocities) [12, 13]. However, it should be noted that periodicity is not the only source of dispersion, and it has also been shown to occur for mechanical wave propagation in bars of narrow radius [23] and in shallow bodies of water [24, 25].

The most prominent feature of these periodic dispersive structures is the presence of band gaps in their dispersion relation. The dispersion relation describes the relationship between the wavelength and the frequency (or energy) of the wave [12, 13]. Waves with frequencies in the band gaps (or energies in the case of electron diffusion) cannot propagate through the material and are reflected [12, 13]. This idea of discreteness affecting wave propagation originates with Newton who assumed that sound

propagated in air in the same manner as an elastic wave propagates along a lattice of springs and point masses [12, 26]. Following Newton, the theory of mechanical lattice dynamics has been a topic of continual study, and has been applied to everything from waves traveling along strings to the vibration of real crystal lattices [12]. This history is summarized in the first chapter of Brillouin’s book (up to the time of its publication) [12].

The study of how structural periodicity affects wave propagation has not been confined to just mechanical lattices, and includes many types of waves occurring in multiple settings [13]. Some of the earliest studies were in the field of condensed matter physics and focused on wave propagation in crystalline solids [10, 12, 13, 27, 28]. This includes the study of electron propagation through periodic potential fields in semiconductors, which can be described by the Schrödinger equation [10, 13, 28]; and the propagation of elastic lattice (phonon) waves, which can be described by Newton’s equation [10, 12, 13, 27]. Based on the ideas developed for the propagation of electrons through periodic potentials, the field was expanded to settings other than crystalline solids, which includes: the propagation of electromagnetic (photons) waves through media with periodic dielectric layers, which can be described by Maxwell’s equations [13, 28–30]; the propagation of surface plasmons [31]; the behavior of ultracold atoms [13]; and the propagation of elastic and acoustic waves through periodic composite structures [13, 14, 27]. In this thesis, I focus on the propagation of mechanical (phononic) waves, which is most related to the examples of lattice waves propagating through crystalline solids and elastic and acoustic waves propagating in layered composite structures [10, 12–14, 27].

1.4 Periodic Phononic Structures

As previously described there is a long history relating to mechanical wave propagation in periodic phononic structures [12, 14]. Both elastic waves in solids and acoustic waves in fluids are included in this scope. There is an important difference between the two in that elastic waves in solids support both longitudinal and transverse wave

polarizations (three polarizations total, with two transverse and one longitudinal), and acoustic waves in fluids support only longitudinal waves as fluids cannot support shear stress [6, 14]. However, the structural periodicity can similarly affect the propagation of both types of waves [6, 14].

Initially, the study of mechanical wave propagation in periodic structures was focused on simple mechanical systems and crystalline solids [12]. Since Brillouin, this study has been extended to include a whole new class of artificial composite materials designed to affect the propagation of mechanical waves through dispersion induced by the structural discreteness and periodicity [6, 13, 14, 27]. These materials have formed the basis for the emerging field of phononics, which encompasses materials constructed to control the propagation of elastic and acoustic mechanical waves at structural scales ranging from the macro- to nanoscales [6, 13, 14, 27]. Two examples of such phononic structures, at different length scales, are shown in figure 1.1.

Many studies were done on this subject around the 1970s including experimental studies of pass and stop bands in layered composite materials [32], particulate composites [33], and theoretical studies of wave propagation in periodic composites [34], among others [35]. These studies showed pass and stop bands for either transverse or longitudinal elastic waves (but not both at the same time). A review of these works can be found in [35].

Upon the advent of photonic crystals [28–30, 36], renewed interest was given to the field following several numerical studies published around the same time by Kushawa, Djafari-Rouhani, and collaborators [37] and Sigalas and Economou [38, 39]. These theoretical and numerical studies showed complete band gaps (for all wave polarizations) in (two-dimensional) 2D and (three-dimensional) 3D solid-solid and solid-fluid systems with a high contrast in wave propagation speed between the composite materials. For a review see [14, 40]. One of the first experimental examples of such a structure was a sculpture in Madrid (figure 1.1(a)) which was observed to have complete sonic frequency band gaps [1]. Recent experimental examples include a hypersonic frequency nanostructured 1D phononic crystal [2] (as shown in figure 1.1(b)), spheres embedded in a polymer matrix [41], and hypersonic band gaps in colloidal

crystals [42]. For some recent reviews see [6, 14, 43].

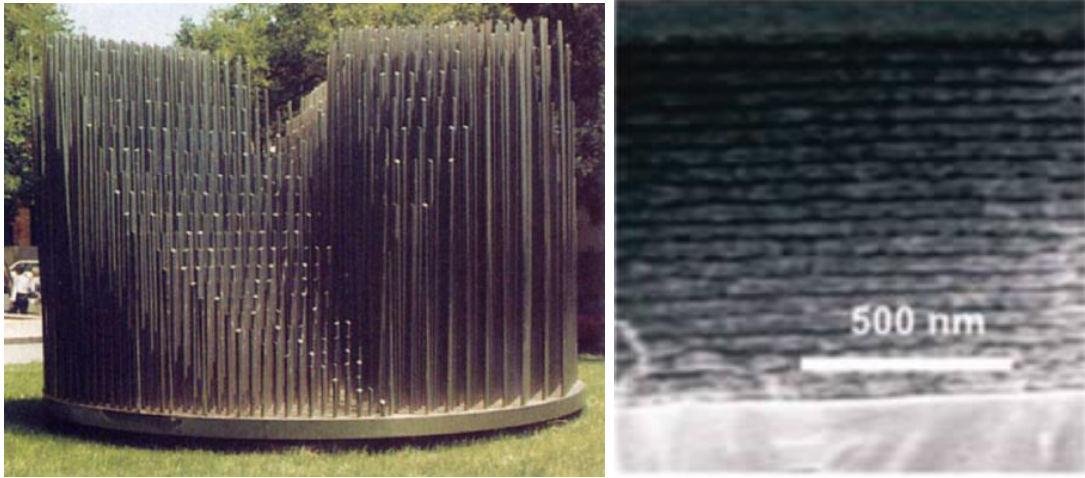


Figure 1.1: Phononic crystals. (left) Macroscopic sonic phononic crystal and sculpture by Eusebio Sempere, Madrid [1]. (right) One-dimensional hypersonic phononic crystal [2].

Although the previously mentioned examples of phononic structures are widely varied in their construction, frequency of operation, and in the analytical methods used to calculate the characteristics of their dispersion relation [12, 40], the underlying concept is the same. When the wavelength is on the order of the periodicity or spatial discreteness of the material, the propagation of mechanical waves is dispersive, and waves with frequencies in the band gaps of the dispersion relation will be reflected by the material [12, 27, 44].

Furthermore, most of the examples of, and analytics for, phononic structures are based on linear dynamics. Aside from granular crystals (which will be subsequently discussed in further detail), there are few, particularly experimental, examples of nonlinear periodic phononic structures. The importance of including nonlinearity is that the presence of nonlinearity adds flexibility to the system, and new ways to control the flow of energy. This includes the breaking of time-reversal symmetry, new ways to tune the system and localize energy, and new ways to convert energy between frequencies [15–20]. Some recent experimental examples of the application of nonlinearity to the field of phononics include the use of a bubbly material as a

nonlinear medium in an acoustic rectifier [45], high amplitude picosecond ultrasonic pulse propagation in crystalline solids [46], and nonlinear acoustic wave propagation in structures with periodic surface features [47].

Despite the few examples of nonlinear phononic structures, there exists a wealth of research into other nonlinear systems (mechanical and otherwise), as will be summarized in the following section.

1.5 Nonlinear Lattices

The study of the dynamics of nonlinear systems has a long history stretching back to Newton’s study of orbital dynamics [15]. The study of nonlinear dynamics is important as it describes the behavior of many real systems, and includes examples ranging from the weather, the swinging of a pendulum, the vibration of structures at high deformations and strain rates, or a chain of elastic spheres in contact, among many others [15, 16, 21, 48]. In general, linearity (as compared to nonlinear behavior) in dynamical systems seems to be more of the exception than the rule. Because the granular crystal systems described in this thesis can be modelled as lattices of nonlinear springs and point masses (as will be described), this section is focused on a brief history and comparison of the major types of nonlinear lattices.

Since the first computational experiments in nonlinear mass-spring lattices by E. Fermi, J. Pasta, and S. Ulam in 1955 [49, 50], there has been a wealth of interest in the dynamics of nonlinear lattices [48]. Using one of the first modern computers, Fermi, Pasta, and Ulam (FPU) studied a system where the restoring (spring) force between two adjacent masses was nonlinearly related to the relative displacement between masses, and investigated how long would it take for long-wavelength oscillations to transfer their energy (thermalize) into an equilibrium distribution [48, 50]. Instead of the predicted thermalization they found that, over the course of the simulation, most of the energy had returned to the mode with which they had initialized the system in coherent form [50].

This discovery initiated whole fields of research relating to the study of nonlinear

waves in discrete lattices [48, 50]. This includes many different types of nonlinear lattices inspired by physical systems (in addition to the FPU lattice), and the study of physical phenomena occurring in them [48]. A review of nonlinear waves in lattices can be found in [48]. The nonlinear lattices most commonly studied can be roughly categorized into three types: the discrete nonlinear Schrödinger (DNLS), the Klein-Gordon (KG), and the FPU lattices [48]. The 1D forms of these lattice equations are as follows [48].

The DNLS can be written as

$$j\dot{u}_i = -\epsilon(u_{i+1} + u_{i-1}) - |u_i|^2 u_i, \quad (1.1)$$

the KG can be written as

$$\ddot{u}_i = \epsilon(u_{i+1} + u_{i-1} - 2u_i) - V'(u_i), \quad (1.2)$$

and the FPU can be written as

$$\ddot{u}_i = V'(u_{i+1} - u_i) - V'(u_i - u_{i-1}), \quad (1.3)$$

where u_i is the dynamical variable of interest at site i , ϵ is a coupling parameter (constant), $j = \sqrt{-1}$, and V is a nonlinear potential function. The DNLS equation has been used to describe nonlinear waveguide arrays and Bose-Einstein condensates, among others [48, 51]. Additionally, under small-amplitude assumptions, the DNLS can be derived from the KG and FPU lattices [51]. The KG system is more similar to the FPU system, but on the left has terms for a linear spring interaction and an on-site nonlinear potential. The KG system has been used to model systems of coupled pendula, electrical systems, and metamaterials with split ring resonators, among others [48]. In contrast to the KG system, the FPU has no on-site potential term, and instead involves a nonlinear potential based on nearest neighbor interactions (nonlinear springs). The system used to describe the behavior of granular crystal systems is a type of FPU lattice [48]. The FPU system has also been used to describe

other types of nonlinear mechanical systems and the behavior of dusty plasmas [48].

Studies of all these lattices have showed the emergence of localized nonlinear structures and have been used to understand the existence of such phenomena in other nonlinear (not necessarily discrete) systems. Two examples of nonlinear coherent structures, which are particularly applicable to the study of granular crystals, are solitary waves and discrete breathers. Solitary waves were first observed by J. Russell in a shallow water-filled canal in 1844 [25]. Since then they were shown to be a solution of the Korteweg-de Vries (KdV), a nonlinear partial differential equation, and have been discovered in myriad systems and discrete nonlinear lattices of all the above types [48, 52] (including granular crystal systems [21]). Discrete breathers are a type of intrinsic (not tied to any structural disorder) localized mode, and have been the subject of many theoretical and experimental investigations [19, 51, 53–58]. Discrete breathers have been demonstrated in charge-transfer solids [59], antiferromagnets [60], superconducting Josephson junctions [61, 62], photonic crystals [36], biopolymers [63, 64], micromechanical cantilever arrays [65], and more. In addition to nonlinear localized structures, the presence of nonlinearity dynamical lattices makes available an array of useful phenomena including quasiperiodic and chaotic modes, sub- and superharmonic generation, bifurcations, the breaking of time-reversal symmetry, and frequency conversion [15–20, 24, 66].

1.6 Disorder in Periodic Structures

In addition to the dispersive effects caused by perfect periodicity, the addition of disorder (or defects) to discrete lattices introduces interesting effects. Many studies have been done on the effects of disorder and defects, and their connection to energy localization. In the seminal work by P. W. Anderson in 1958, he showed the absence of diffusion in sufficiently disordered linear media (initially for electrons in semiconductors, although it is generally applicable), and he explained the relationship of disorder to mode localization [67]. The effects of individual defects and the existence of localized defect modes (linear and nonlinear) have also been widely studied in solid state

physics (see [27, 68–73] and references therein). The study of defects also includes other systems such as photonic crystals [74, 75], optical waveguide arrays [76–78], dielectric superlattices (with embedded defect layers) [79], micromechanical cantilever arrays [65, 80], and Bose-Einstein condensates of atomic vapors [81, 82].

1.7 Granular Crystals

Granular crystals are arrays of elastic particles in contact, and are a type of discrete-nonlinear system (or nonlinear periodic structure). An example of a 1D granular crystal is shown in figure 1.2.



Figure 1.2: 1D granular crystal composed of 19.05 mm diameter steel and aluminium spheres.

The nonlinearity results from Hertzian contact between particles with elliptical contact area [83, 84]. Hertzian contact relates the contact force $F_{i,i+1}$ between two particles (i and $i+1$) to the relative displacement $\Delta_{i,i+1}$ of their particle centers, as shown in equation 1.4.

$$F_{i,i+1} = \alpha_{i,i+1} [\Delta_{i,i+1}]_+^{n_{i,i+1}}. \quad (1.4)$$

Values inside the bracket $[s]_+$ only take positive values, which denotes the tensionless characteristic of the system (i.e., there is no force between the particles when they are separated). For $\Delta_{i,i+1} = 0$ the particles are just touching, $\Delta_{i,i+1} > 0$ the particles are in compression, and $\Delta_{i,i+1} < 0$ the particles are separated. For two spheres (or a sphere and a cylinder) as is studied in this thesis:

$$\alpha_{i,i+1} = \frac{4E_i E_{i+1} \sqrt{\frac{R_i R_{i+1}}{R_i + R_{i+1}}}}{3E_{i+1}(1 - \nu_i^2) + 3E_i(1 - \nu_{i+1}^2)}, \quad n_{i,i+1} = \frac{3}{2}, \quad (1.5)$$

where E_i , ν_i , R_i are the elastic modulus, the Poisson's ratio, and the radius of the i th particle, respectively. The $n_{i,i+1} = 3/2$ comes from the geometry of the contact between two linearly elastic particles with elliptical contact area, as can be seen in [84]. In addition to assuming the contact area is elliptical, and that both particles remain linearly elastic, the derivation of Hertzian contact assumes [84] (i) the contact area is small compared to the dimensions of the particle, (ii) the contact surface is frictionless with only normal forces between them, (iii) the motion between the particles is slow enough that the material responds quasi-statically. Because of the nonlinear Hertzian interaction potential between particles, it is important to note that (as will be explained in greater detail in the following sections) under the presence of a static load, the dynamic behavior of the system is tunable to encompass linear, weakly nonlinear, and strongly nonlinear regimes [21, 22]. As will be described in the following, this tunability and flexibility has allowed for a wide range of studies to be conducted focusing one or more of these dynamical regimes present in granular crystal systems. It has been used for the investigation of fundamental nonlinear dynamic phenomena in discrete systems, and has been implemented in and suggested for use in engineering applications.

1.7.1 Granular Crystals Brief Historical Review

Granular materials have been used throughout history as exemplary devices for the absorption of impacts and vibrations [21]. A couple of examples include the use of sand bags to stop bullets, or the use of iron shot as insulation in explosive chambers [21]. More recently the physics behind such capabilities has become an area of intense study. This research can roughly be divided into two conceptual categories: disordered granular flows [85], and the behavior of packed granular arrays (or granular crystals) [21, 52]. This thesis is focused on the later.

The study of packed granular crystals emerged in 1983 with the study by A. N. Lazaridi and V. F. Nesterenko, showing analytically, numerically, and experimentally, the existence of highly nonlinear solitary waves and the sonic vacuum phenomenon

in 1D granular crystals [86, 87]. Since then granular crystals have received much attention, and many studies have been done on the phenomena occurring in them. Following Nesterenko's seminal works [86, 87], he continued to publish studies relating to solitary and shock wave propagation in highly nonlinear granular crystals and the sonic vacuum (most of which are in published Russian, but are referenced and described in his book [21]). With respect to the analytical derivation of the solitary wave solution, Nesterenko's solution has been revisited [88] and alternate approaches have been taken [89–91].

High amplitude impulse dynamic loading in uncompressed (highly nonlinear) 1D and 2D granular crystals composed of elastic spheres and disks has been investigated by A. Shukla and collaborators [92–95]. In particular, theirs was some of the earliest research into how high impulse stress waves propagate in quasi-1D and γ -shaped granular media. They used a combination of numerical and experimental techniques including high speed photographic, photoelastic, and strain gage measurements.

S. Sen and collaborators numerically studied solitary wave propagation [52], and the effects of their crossing [96], in unloaded (highly nonlinear) granular crystals with application for detecting buried impurities [97, 97, 98] and impact absorbers [99]. In a related impact absorption study, J. Hong and collaborators used numerical techniques to describe a universal power law decay in granular protectors [100]. They numerically studied the evolution of meta-stable breathers initiated by quasi-statically displacing a single particle [101].

C. Coste and collaborators studied granular crystal response across several dynamical regimes. This includes one of the earliest experimental studies (aside from the early work of Nesterenko [86]) on highly nonlinear solitary wave propagation in uncompressed or lightly compressed 1D granular crystals [102]. This was followed by a study exploring the validity of Hertzian contact in 1D granular crystals under a variety of loading (static and dynamic) conditions and dynamical regimes [103]. This study comparatively explored alternative models to the Hertzian potential and characterized the effect of localized plasticity near the contact. C. Coste and B. Gilles also conducted some of the earliest studies on linear wave propagation in highly com-

pressed 2D granular crystals [104, 105]. Increasing further in dimensionality, a recent study by V. Tournat and collaborators investigated linear band gaps in hexagonal close packed (hcp) three-dimensional (3D) compressed granular crystals using a combination of analytical, numerical, and experimental techniques [106]. Tournat and collaborators also studied self-demodulation in compressed 1D granular crystals—a weakly nonlinear effect [107].

A. C. Hladky-Hennion, M. de Billy, and collaborators conducted several studies involving the linear response of 1D periodic (monoatomic and diatomic with a two particle unit cell) arrays of glued [108], welded [109], and elastically compressed spherical particles [110]. These systems were shown to exhibit tunable phononic band gaps. They also demonstrated the existence of subresonances in granular crystals related to the resonant modes of the individual spherical particles [111]. More recently A. C. Hladky-Hennion and collaborators have studied quasi-1D chains of “stubbed” wave guide arrays, or glued granular crystal arrays with sets of spheres glued on in the perpendicular direction to the axis of the crystal [112, 113]. Another alternate geometry involving linear wave propagation in periodic granular crystals is a recent study by F. J. Sierra-Valdez and collaborators studying 1D and 2D arrays of magnetic spheres where the magnetization is modulated [114].

S. Job, F. Melo, and collaborators also studied several aspects of highly nonlinear solitary pulse propagation using a combination of analytical, numerical, and experimental techniques. This includes experimental studies of shock mitigation in tapered chains [115], the interaction of solitary waves with boundaries [116], the effect of small amounts of viscous fluid near the contact area [117], and highly nonlinear wave localization around a mass defect [118]. Another previous numerical study on this topic (highly nonlinear solitary waves in 1D granular crystals with impurities) was done by Hascoet and collaborators [119].

Several numerical and theoretical studies of granular crystal phenomena have recently been done separately by K. Lindenberg and collaborators. K. Lindenberg has published several works on 1D uncompressed granular crystal systems relating to friction and dissipation [120, 121], a binary collision model for pulse propagation

[122], and tapered and decorated chains [123, 124]. A. F. Vakakis and collaborators have also recently studied the localized, traveling, and nonlinear normal modes in 1D uncompressed granular chains [125, 126].

In addition to these studies, since 2005, much research has been done in the field of granular crystals by C. Daraio and collaborators. Utilizing a combination of analytical, numerical, and experimental approaches, their research includes the study of anomalous strongly nonlinear wave reflection at the interface of two different 1D granular crystals [127]; highly nonlinear wave propagation in a 1D granular crystal composed of teflon spheres [128], polymer-coated steel spheres [129], diatomic chains of spheres [130], heterogeneous chains of spheres of higher periodicity [131], and disordered chains of spheres [132]; the tunability of solitary wave properties in 1D granular crystals [22]; dissipation and its effects on solitary waves in 1D granular crystals [133]; the behavior of stationary shocks in 1D highly nonlinear granular crystals [134]; and highly nonlinear solitary wave splitting and recombination in Y-shape granular crystals [135]. The studies done by this group have also included a numerical study of defects modes [136] and an analytical, numerical, and theoretical study of tunable frequency band gaps [137] in highly compressed (linear and weakly nonlinear) 1D diatomic granular crystals. They explored the engineering application of such granular crystal related phenomena in shock and energy absorbing layers [138, 139], actuating devices [140], acoustic lenses [141], and sound scramblers [127, 128].

It is clear that while much work has been done in the highly nonlinear regime of 1D granular crystals, and some work done in the linear regimes in 1D, 2D, and 3D, even in 1D granular crystals, the weakly nonlinear regime has been left relatively untouched. This thesis will focus on several phenomena characteristic of the weakly nonlinear regime and some unexplored phenomena in the near-linear regime.

1.7.2 One-Dimensional Granular Crystals

The granular crystals explored here are statically compressed 1D arrays of elastic spherical (or cylindrical) particles in contact. Because the stiffness of the contact

between two spheres is very low compared to the bulk stiffness of the particles composing the crystal, we approximate this array as a system of nonlinear springs and point masses. Another perspective from which to approach this same idea is that the characteristic (resonant) frequencies of the particles themselves are very high compared to the frequencies of the granular crystal system involving the rigid body-like motion of the particles in the system.

The (conservative) Hamiltonian of this statically compressed system of springs and point masses can be written as:

$$H = \sum_{i=1}^N \left[\frac{1}{2} m_i \left(\frac{du_i}{dt} \right)^2 + V(u_{i+1} - u_i) \right], \quad (1.6)$$

where m_i is the mass of the i th particle, $u_i = u_i(t)$ is its displacement from the equilibrium position in the initially compressed chain, and $V(u_{i+1} - u_i)$ is the interaction potential between particles i and $i+1$. Accordingly, we split up the static and dynamic contributions to the displacement, where $\Delta_{i,i+1} = \delta_{i,i+1} + u_i - u_{i+1} = \delta_{i,i+1} - \phi_{i,i+1}$, $\Delta_{i,i+1}$ is the total displacement between the centers of adjacent particles, $\delta_{i,i+1}$ is the initial (static) displacement (which results from the static compression force F_0), and u_i is the dynamic displacement as previously described. Assuming the previously mentioned assumptions for Hertz contact hold, we set V to be the tensionless Hertzian contact potential. To ensure that the classical ground state, for which $u_i = \dot{u}_i = 0$, is a minimum of the energy H , we also enforce that the interaction potential satisfies the conditions $V(0) = V'(0) = 0$, $V''(0) > 0$. The interaction potential can thus be written in the following form [52, 91]:

$$V(\phi_{i,i+1}) = \frac{1}{n_{i,i+1} + 1} \alpha_{i,i+1} [\delta_{i,i+1} - \phi_{i,i+1}]_+^{n_{i,i+1} + 1} - \alpha_{i,i+1} \delta_{i,i+1}^{n_{i,i+1}} \phi_{i,i+1} - \frac{1}{n_{i,i+1} + 1} \alpha_{i,i+1} \delta_{i,i+1}^{n_{i,i+1} + 1}, \quad (1.7)$$

where $\phi_{i,i+1} = u_{i+1} - u_i$ denotes the relative dynamic displacement, and $\alpha_{i,i+1}$ and $n_{i,i+1}$ are the coefficients that depend on material properties and particle geometries (as before).

The energy E of the system can be written as the sum of the energy densities e_i of each of the particles in the chain, where we approximate the energy density of each

particle to have half the potential energy contributions from each contact:

$$\begin{aligned}
 E &= \sum_{i=1}^N e_i, \\
 e_i &= \frac{1}{2} m_i \dot{u}_i^2 + \frac{1}{2} [V(u_{i+1} - u_i) + V(u_i - u_{i-1})].
 \end{aligned} \tag{1.8}$$

For the case of two spheres (or a sphere in contact with the flat face of a cylinder) $\alpha_{i,i+1}$ and $n_{i,i+1}$ are as defined in equation 1.5. For this case, a granular crystal can be modelled as the following system of nonlinear springs and point masses:

$$m_i \ddot{u}_i = \alpha_{i-1,i} [\delta_{i-1,i} + u_{i-1} - u_i]_+^{3/2} - \alpha_{i,i+1} [\delta_{i,i+1} + u_i - u_{i+1}]_+^{3/2} - \frac{m_i}{\tau} \dot{u}_i, \tag{1.9}$$

where τ is an experimentally determined coefficient relating to the strength of the linear damping. The linear damping term was included to account for the dissipation occurring in the real system. Linear damping (versus Coulomb friction, a nonlinear damping term, or others) was selected by matching the qualitative profile of the decay to the experimental results. The coefficient τ was selected by matching the rate of decay from the experimental results.

1.7.3 Weakly Nonlinear Granular Crystal

Considering the (conservative, $\tau = \infty$) Hamiltonian case, if the dynamical displacements have small amplitudes relative to those due to the static compression ($|\phi_{i,i+1}| < \delta_{i,i+1}$), the weakly nonlinear dynamics of the granular crystal can be considered. To describe this regime, a power series expansion of the forces can be taken (up to quartic displacement terms) to yield the, so-called, $K_2 - K_3 - K_4$ model [142]:

$$m_i \ddot{u}_i = \sum_{j=2}^4 K_{j,i,i+1} [(u_{i+1} - u_i)^{j-1} - (u_i - u_{i-1})^{j-1}], \tag{1.10}$$

where $K_{2,i,i+1} = \frac{3}{2} \alpha_{i,i+1}^{2/3} F_0^{1/3}$ is the linear stiffness, $K_{3,i,i+1} = -\frac{3}{8} \alpha_{i,i+1}^{4/3} F_0^{-1/3}$, and $K_{4,i,i+1} = \frac{3}{48} \alpha_{i,i+1}^2 F_0^{-1}$. For this simplified model, there are analytical solutions for

certain nonlinear phenomena including the form of the discrete breather solution and the onset of modulational instability [142]. However, because this model loses accuracy as $|\phi_{i,i+1}|$ approaches $\delta_{i,i+1}$, and analytical solutions for the fully nonlinear system are more cumbersome, numerical simulations were heavily relied on (Newton-Rahpson method) to predict solutions of the fully nonlinear system.

1.7.4 Linear Granular Crystal

For dynamical displacements with amplitude much less than the static overlap ($|\phi_{i,i+1}| \ll \delta_{i,i+1}$), the nonlinear K_3 and K_4 terms can be neglected from equation (1.10), and the linear dispersion relation of the system computed [137]. The resulting harmonic system of springs and masses is a textbook model for vibrational normal modes in crystals [10, 12]. With this reduced model the dispersion relation of the infinite system can be predicted (including pass and stop bands) and the normal modes of the finite system (eigenfrequencies and mode shapes) computed. For examples, see chapter 2 for calculation of the dispersion relation and state-space transfer function in a diatomic system, and see chapter 5 for the normal modes of disordered finite systems.

1.8 Experimental Setup

An experimental setup was designed to test the vibrational response of statically compressed 1D granular crystals. The setup was designed to be adjustable and easily accomodate many different granular crystal configurations (particle type and size, length, static load, sensor locations and type of measurement). The details of the experiments in each chapter differ slightly, but many of the core elements are consistant throughout. The core design of this experimental setup is shown in figure 1.3, and will be detailed in the following section.

The particles composing the granular crystals are positioned on two (or four) 12.7 mm polycarbonate rods, which are aligned with 12.7 mm thick polycarbonate guide plates designed to align 19.05 mm diameter particles in a 1D configuration, while still allowing the particles to move freely in the axial direction. The polycarbonate

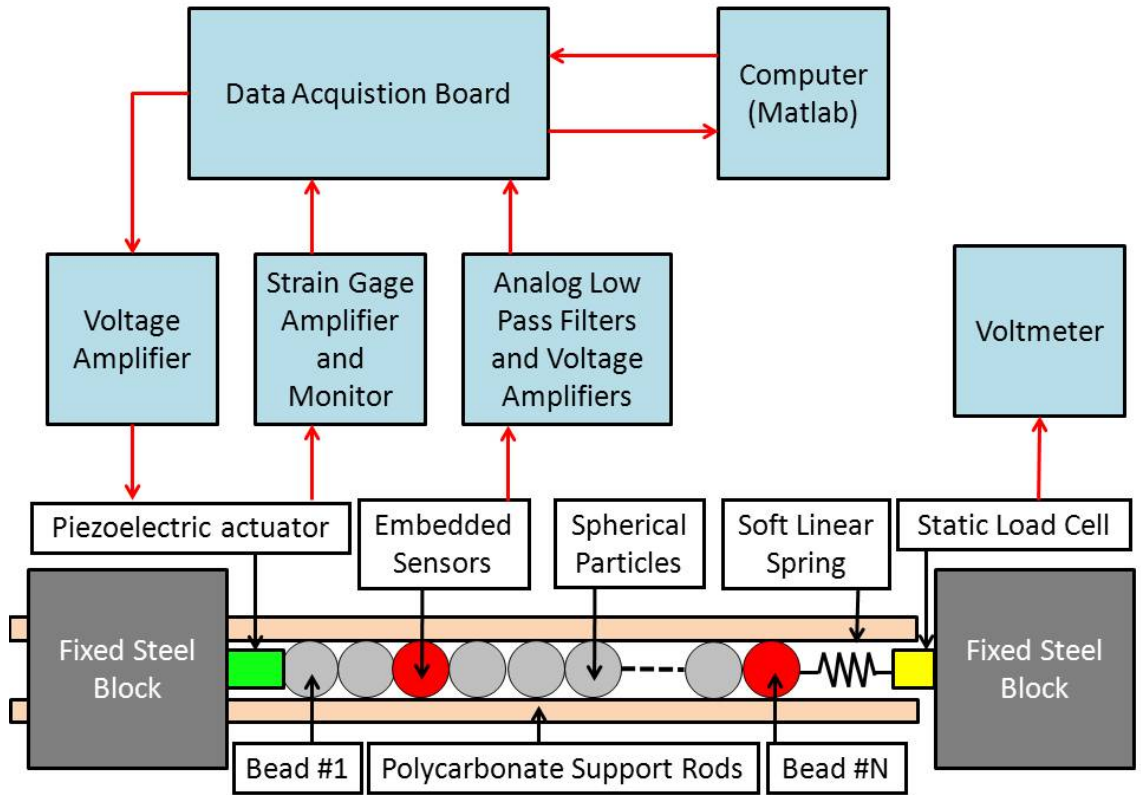


Figure 1.3: Schematic of experimental setup. Red (light gray) arrows denote direction of data flow.

guide plates are 10.16 cm in height and width, with a 19.2 mm diameter hole centered 5.08 cm from the bottom edge. Four 12.7 mm diameter holes are placed in a square configuration around the larger center hole to support the particles, such that the edge of the rod is 9.53 mm from the center of the large hole. Polycarbonate rods were used (over metals) for several reasons. They are electrically insulating – so as to prevent sensor cross-talk. They have a high elastic modulus (for plastics) that is sufficiently stiff to support the granular crystal. They have a low coefficient of friction in contact with the steel and aluminum particles composing the granular crystal, so that alignment structure can be sufficiently decoupled from the system. They also have relatively (compared to the granular crystal particles) high dissipation, which will be useful to dissipate any signals transferred to the rods by frictional or transverse coupling. The configuration with four rods was a square configuration,

used to keep the chain from buckling under high static loads. For experiments with lower static loads, only the bottom two polycarbonate rods were used, where gravity was sufficient to keep the chain from buckling. In the cases with higher static loads, the top rods were needed to keep the crystal in approximately a 1D configuration because a chain of spheres in contact (point contacts) is a geometrically unstable configuration. In all the experiments using four rods, a small upshift in the frequency of the dispersion relation was observed [5, 143, 144]. The spatial gap between the chain particles and the top rods (which characterizes the degree to which the chain can buckle) was $\approx 200 \mu\text{m}$. It is currently hypothesised, though it has not yet been rigorously tested, that this upshift is in part connected to the buckling of the chain, as it was not observed in the two-rod configuration. For experiments where smaller radii particles were used, polycarbonate or teflon insert rings were used to align the particles with the axis of the granular crystal. The insert rings have an outer diameter of 19.05 mm and an inner diameter slightly larger than the particle it is being used to support. The thickness is 6.35 mm for particles with diameters greater than 6.35 mm (the thickness near the particle is reduced for smaller particle insert rings).

Dynamic perturbations were applied to the granular crystals using a piezoelectric actuator (Piezomechanik PSt 150/5/7 VS10 or PI P-820.10) mounted on a steel block, and the evolution of the force-time history of the propagating excitations was visualized using a calibrated dynamic force sensor, which are described in further detail in the following sections. At the opposite end of the crystal with respect to the piezoelectric actuator, a static compressive force, F_0 , was applied using a lever-mass system (composed of two steel bars at 90 degree angles, a mass hung on the horizontal portion, and two fulcrum support plates) or a soft (compared to the contact stiffness of the particles) stainless steel linear compression spring (McMaster 9435K141, 18.5 mm diameter, 5.08 cm uncompressed length, 1.24 kN/m stiffness), which are described in further detail below. The resulting applied static load is measured with a static load cell (Transducer Techniques SLB-25) mounted in a teflon holder (outer diameter 19.05 mm) placed in between the steel cube and the spring. As shown in figure 1.3, the driving signals are generated with MATLAB and a Data Acquisition Board (DAQ,

National Instruments 6251-USB), and passed to the piezoelectric actuator through a voltage amplifier (Piezomechanik LE 150/100 EBW or Piezo Systems Inc. EPA-104-115). The measured piezoelectric sensor signals are conditioned with voltage amplifiers (Olympus NDT 5660) and or combined voltage amplifiers and analog low pass filters (Alligator Technologies USBPGF-S1) before being passed, along with the output of the strain gage embedded in the piezoelectric actuator (via Piezomechanik DMS-01 strain gage amplifier), to MATLAB via the DAQ. The output of the static load cell is measured by a separate voltmeter.

For the experiments in chapter 3 the components used were the PI P-820.10 actuator, the Piezo Systems Inc. EPA-104-115 amplifier, the Olympus NDT 5660 amplifiers, and the lever mass compression system. For the experiments in all the other chapters, the components used were the Piezomechanik PSt 150/5/7 VS10 with the embedded strain gage and the strain gage amplifier, the Piezomechanik LE 150/100 EBW amplifier, the Alligator Technologies USBPGF-S1 amplifiers and filters, and the spring plus static load cell compression system.

1.8.1 In-Situ Piezoelectric Sensors

In-situ piezoelectric sensors, as shown in figure 1.4(a),(b) were fabricated to measure the propagating stress waves in the granular crystal.

The sensors are composed of a lead zirconate titanate (PZT) piezoelectric disk (STEMiNC Model SMD15T09S411, 15 mm diameter, 0.9 mm thickness, 2.2 MHz resonant frequency, 3481 pF capacitance) epoxied between two halves of a particle in the granular crystal. The piezoelectric disk measures a voltage proportional (for certain loading conditions) to the stress applied. They were constructed so as to preserve the bulk properties of the original bead, including the contact stiffness, mass, and dimensions [145]. As described in [116], this type of sensor measures the average force between the two adjacent contacts, assuming the resonant frequency of the assembled sensor is much larger than the measured frequencies. Because of this, it is important to use a stiff epoxy that can maintain the bulk stiffness of the particle.

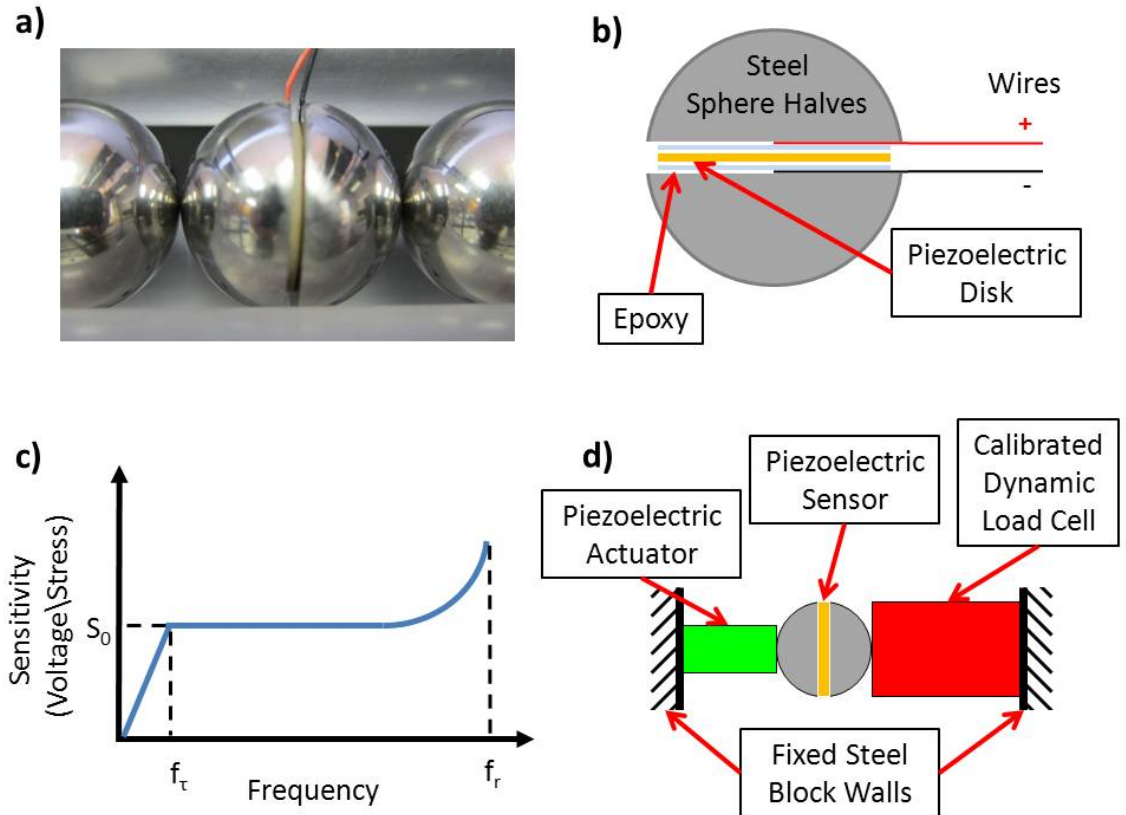


Figure 1.4: In-situ piezoelectric sensor. (a) Photograph of sensor. (b) Schematic of sensor. (c) Sensitivity range. Frequency f_r is the resonant frequency of the assembled sensor. f_t is the discharge time frequency of the sensor. (d) Sensor calibration setup schematic. The actuator applies a low frequency dynamic signal, above f_t and significantly below the resonant frequency of the calibration setup (including motion of the bead).

In addition to this, an epoxy was selected so that when the piezoelectric disk is completely coated with a thin layer, it is electrically insulated from the surrounding particle halves and other sensors in the rest of the crystal.

The resonant frequency (and thus bulk stiffness) was checked by applying an impulsive excitation to the particle and measuring the frequency content of voltage output of the sensor caused by the ringing that followed the impulse. More specifically, this procedure consisted of suspending the sensor, striking the sensor with a stiff low mass object, measuring the time history of the sensor response with an oscilloscope (Tektronix TDS2014B), and calculating the Fast Fourier Transform of the sensor

ringing following the impulse. The stiffness was estimated by approximating the assembled sensor as two free point masses (bead halves) connected by a linear spring (epoxy and piezo). The 19.05 mm 316 stainless steel sensors were measured to have a resonant frequency of $f_r \approx 80$ kHz (well above the measurement frequencies of interest). This resonant frequency is important also for characterizing operational frequency range of the sensor. As shown in figure 1.4(c), when the applied frequencies approach the resonant frequency of the sensor, the sensitivity relating stress to voltage becomes nonlinear. The lower end of the operational frequency range is constrained by the discharge time of the sensor. The discharge time can be estimated as $\tau_d \approx RC$ where R is the resistance of the acquisition/conditioning system connected to the sensor (in this case approximately 10 G Ω), and C is the capacitance of the sensor. A longer discharge time gives a wider frequency range, where the lowest measureable frequency can be approximated as $f_\tau \approx \frac{1}{RC}$. Accordingly, it is desirable to have a high resistance and capacitance in this application. The 19.05 mm 316 stainless steel sensors used here were estimated to have $f_\tau \approx 0.03$ Hz.

The sensitivity of the sensors was calibrated with the setup shown in figure 1.4(d). The piezoelectric sensor was compressed between the piezoelectric actuator and a commercially calibrated dynamic load cell (PCB 208C01), both of which were mounted on steel blocks fixed to the optical table that serve as rigid walls. A low frequency harmonic force (100 Hz) was applied through the piezoelectric actuator, with frequency higher than the discharge time of both sensors, but low enough compared to the resonant frequencies of each component and the setup as a whole such that the system responds quasistatically. Because the system is responding quasistatically, the force measured by the commercial load cell can be compared with the voltage coming from the piezoelectric sensor. The method of acquiring the data for this comparison is as detailed in the following sections.

1.8.2 Piezoelectric Actuator

A preloaded piezoelectric stack actuator (Piezomechanik PSt 150/5/7 VS10 or PI P-820.10) was used to apply dynamic perturbations to the granular crystal. A piezoelectric actuator was chosen over an electrodynamic shaker (higher displacements, lower frequency range) because of the high frequency (and force generation) requirement of the experiments. There are several factors important in the selection of the piezoelectric actuator. A preloaded actuator is important for good high frequency dynamic response. Similarly to the piezoelectric sensors, the resonant frequency of the actuator must be significantly greater than the frequency content of the applied signal and of the crystal response to maintain linear actuator operation. The stiffness of the actuator should also be greater than the stiffness of the mechanical system it is coupled to (the granular crystal), so that the behavior of the actuator is sufficiently decoupled from the response of the system. For similar piezoelectric materials, a larger stiffness is achieved with a larger cross-sectional area and shorter length stacks. Both of these aspects can be problematic, in that a larger cross-sectional area results in a higher actuator capacitance, and a shorter stack results in less actuator stroke length (and less force generated in the granular crystal, albeit decreasing the capacitance). A higher actuator capacitance limits the effective frequency and stroke range of the actuator by increasing the current requirement of the amplification electronics. The current requirement for long term harmonic operation is defined as $I = CUf_{act}$, where I is the average current, C is the actuator capacitance, U is the applied voltage, and f_{act} is the signal/actuator frequency [146]. Accordingly, increased actuator flexibility can be gained by using a voltage amplifier of the largest possible power to drive the actuator.

The piezoelectric actuator used here (for all experiments other than the discrete breathers experiments, described in chapter 3 and [5]), incorporates a built in strain gage. This strain gage can be used to directly monitor the actuator response during the experiments. Both the strain gage and the sensitivity of the actuator (stroke/displacement versus applied voltage) was calibrated with a laser vibrometer.

The calibration consisted of driving the piezoelectric actuator harmonically (while attached to the mounting block, but free from the granular crystal) and simultaneously measuring the output of the embedded strain gage and the output of the laser vibrometer. From the strain measured by the strain gage and the velocity of the piezostack cap measured by the laser vibrometer, the displacement of both signals could be calculated and compared. Operating sufficiently below the resonant frequency of the actuator to maintain a linear actuator response, and operating below the voltage limit imposed by the maximum available current, the actuating frequency, and the actuator capacitance—the actuator displacement varies linearly with voltage. This linear sensitivity was obtained with the laser vibrometer, as per the previously described process.

The stiffness of the actuator was also calibrated using the embedded strain gage in two ways. The first was to measure the resonant frequency of the actuator (via the response of the strain gage) with different masses attached to the end of the actuator, while driving the actuator (not attached to the granular crystal) with low amplitude bandwidth limited noise. In this configuration, the actuator is modelled as a single degree of freedom linear spring mass system, and we estimate the stiffness accordingly. The second method was to measure the change in the stroke/displacement amplitude when the actuator is free (not attached to the granular crystal), and when the actuator is coupled to the granular crystal. In both cases the actuator was found to have a high stiffness compared to the granular crystal. Because of this, the actuator was modeled as a rigid moving wall in numerical simulations.

1.8.3 Data Acquisition and Sampling

Signal generation and acquisition was done with a Data Acquisition Board (National Instruments NI-6251-USB) attached to a PC driven by MATLAB. There are several important factors involved in the selection of the DAQ. The sampling frequency f_s should be as high as possible, as this quantity defines the maximum measureable frequency (which by the Nyquist criterion is $f_s/2$ [147]). For the following chapters

the sampling frequency f_s was: chapters 2 and 6 - 200 kHz, chapter 3 - 125 kHz, and chapter 5 - 250 kHz. This is particularly important when digitally sampling, so as to avoid aliased signals that can cause frequency content above this threshold to appear as low frequency content in the measurement (it is generally best to sample above the primary resonances in the system). To ensure no aliasing occurs, analog low pass filters were used (in the later experiments), to cut off frequency content above $f_s/2$. In addition to the sampling rate, when using Fourier transform based frequency analysis (for the experiments here, we use Power Spectral Density [PSD], which is the magnitude squared of the Fast Fourier Transform [FFT] [147]), the signal length must be taken into consideration. The frequency resolution of the signal $\delta f = 1/T$ where T is the time length of the measured signal. The DAQ should also have the highest voltage resolution possible so as to avoid erroneous signals from discretizing the data. To this effect, voltage amplifiers were used following the sensors so as to best match the measured signal with the voltage range of the DAQ. The voltage amplifiers also improved the system signal-to-noise ratio. Finally, as previously discussed, a higher DAQ input channel resistance also aids in the measurement of low frequency signals in piezoelectric devices.

1.8.4 Data Analysis and Post Processing Tools

To post process the acquired signal time histories and run the DAQ, several MATLAB (R2008b) functions were utilized. The DAQ was driven by MATLAB via the “Data Acquisition Toolbox”. To calculate the PSD, the onesided *periodogram* function was used with a rectangular window. To create bandwidth limited noise, the *filtfilt* and *butter* (5th order) functions were applied to a uniform random variable for the phase of a harmonic signal.

1.8.5 Boundary Conditions and Static Load Application and Measurement

For these experiments, boundary conditions were designed that could be decoupled from the system response and simply modeled, while applying the static load and allowing the necessary measurements and actuation. For the actuator boundary, a steel block was designed that would act as a rigid wall. Holes were milled to allow the granular crystal alignment rods to be adjusted in length (similar to the polycarbonate guide plate pattern), without moving the actuator mount. The dimensions (the actuator mounting block was a cube of 8.9 cm per side, and the block at the other end of the crystal was a cube of 7.6 cm per side) were designed based on the estimate that the frequency of the first resonant mode of the block should be greater than the frequencies of the system (approximately 23 kHz). This is critical to ensure that the “rigid” wall does not begin to vibrate on its own, otherwise vibrations aside from what is calculated by the applied voltage, and measured by the strain gage will be applied to the granular crystal. Additionally, a resonant frequency within the range of the granular crystal response would cause the boundary to interact with the response of the crystal – creating a nontrivial boundary condition to model. The resonant frequency of the first mode was estimated where $f_b = \frac{1}{2L_b} \sqrt{\frac{E_b}{\rho_b}}$, where L_b is the length of the block, E_b is its elastic modulus, and ρ_b is its density. The resonant frequency was experimentally checked by applying a impulse excitation to the block and measuring the frequency spectrum of the response with accelerometer bolted to the opposite side. As the actuator mount is rigid, and the actuator (as previously described) of high stiffness compared to the granular crystal, in numerics, the front of the actuator is modeled as a moving wall.

Opposite the actuator “rigid wall”, a static load was applied to statically compress the granular crystal. Two methods were used for this. Initially (for the discrete breathers experiments, see figure 3.1), a lever–hanging mass system was used to apply the static load, where the static load applied was calculated based on the lever geometry and calibrated with a static load cell which was then removed. This method was

difficult to model, and not fully decoupled from the system. Because this mechanism was built from steel (stiff at the contact), but allowed to pivot around the lever, it acted like a large mass with applied force boundary condition. However, this did not greatly effect the experiment as the dissipation was high enough and the chain long enough that the dynamic effect of the boundary could not be seen at the beginning of the chain (where the relevant phenomena was occurring). Modifications were attempted, such as adding additional mass to the lever or adding dissipative elements; however in all cases, using an accelerometer measurements, it was found that there was significant movement of the boundary.

Following this, an attempt was made to make a fixed boundary at the other end (similar to the actuator boundary) which would also apply the static load. Though this method was never actually used, it is important for understanding the design of the final boundary condition. A steel block of similar dimensions was fabricated where its position could be adjusted and then fixed to the optical table some distance with respect to the actuator mount – thus statically compressing the crystal. There were several challenges with this method. The first is the measurement of the static load. With the tools then available, the static load could be measured by the displacement of the actuator (based of the embedded strain gage measurement) or with a static load cell. The static load cells used were soft elements (compared to the stiffness of the granular crystal contacts), which create a stiffness defect in the granular crystal or at the boundary, so these were not used in this configuration. The second major challenge was due to the stiffness of the granular crystal as a whole. Under a fixed-fixed condition, any small buckling of the chain, or actuator hysteresis caused a significant change in the effective static load.

Following these attempts, a “free” boundary condition with applied static load was designed (see figures. 1.3, 2.1, and 5.1). A soft stainless steel linear spring (stiffness 1.24 kN/m) was placed in between the moveable steel cube. Thus when the moveable steel block was positioned and fixed with respect to the actuator mount, the spring is compressed and a static load applied to the granular crystal. Because the linear spring is so much softer than the contact stiffness between the particles in the

granular crystal, the boundary is modelled as a free boundary condition. This was confirmed by placing a piezoelectric sensor at the last particle in the chain, applying an impulsive excitation, and measuring the frequency response. The frequency matched closely with that predicted by a free-boundary condition surface mode. Furthermore, because of the low stiffness of the compression spring, anything placed behind the spring (with respect to the granular crystal) is effectively decoupled from the system. The static load cell is thus placed between the spring and the rigid boundary, where the static load cell is mounted in a dissipative teflon holder. This configuration allows the static load to be measured without affecting the response of the chain, and allows for small deviations in the granular crystal realignment and actuator hysteresis without significantly affecting the static load applied to the crystal.

1.8.6 Experimental Procedure

As with the setup in general, many of the elements of the experimental procedure are shared among the experiments of each chapter. An example of this procedure is as follows (where the static compression mechanism is the soft linear spring configuration):

1. Electrical connections are made with coaxial BNC cables.
2. Connect the actuator input to the output of the voltage amplifier (as shown in figure 1.3). Connect a ‘T’ connector to one of the output channels on the DAQ board. Connect one terminal of the ‘T’ connector to an input channel on the DAQ board to directly measure the generated signal. Connect the input of the voltage amplifier to the other terminal of the ‘T’ connector, which is connected to the output channel on the DAQ board. Check the gain on the voltage amplifier.
3. If used, connect the output of the strain gage embedded in the piezoelectric actuator to the strain gage amplifier and monitor. Connect the output of the

strain gage amplifier and monitor to an input channel on the DAQ board. Turn on the strain gage amplifier and monitor.

4. Turn on the DAQ board and the voltage amplifier and set the DC offset voltage to be half of the amplifier positive voltage range. This is performed at the beginning of the procedure to allow the actuator enough time to reach a steady static offset.
5. Prepare the polycarbonate guide rods by sanding them with fine grain sand paper (and regular fine grain paper). Remove any residue with a soft clean cloth. Prepare the particles composing the granular crystal by cleaning with isopropanol.
6. Fix the actuator to the mounting block, and fix the mounting block to the optical table.
7. Align the polycarbonate alignment plates in front of the actuator, and place at regular intervals to span the length of the granular crystal. Position extra guide plates on the opposite side of the actuator mounting block to support any remainder of the polycarbonate guide rods.
8. Insert the polycarbonate guide rods through the polycarbonate guide plates and the actuator mounting block designed for 19.05 mm diameter particles. If using four rods, leave one rod off until the end so that the granular crystal particles can be positioned.
9. Position the particles composing the granular crystal onto the polycarbonate guide rods. If using any smaller radii particles, use a polycarbonate or teflon guide ring with 19.05 mm outer diameter to axially align the particle.
10. Replace desired particles with the custom in-situ piezoelectric sensors (see figure 1.4). Connect the sensor outputs to the input of voltage amplifiers (and or low-pass filters). Check the gains on the voltage amplifiers, and set the cutoff frequency of the low-pass filters to 30 kHz. Connect the output of the voltage

amplifiers to an input channel on the DAQ board. Turn on the voltage amplifiers and low-pass filters.

11. Place the soft linear spring (with outer diameter of approximately 18.5 mm) at the end of the granular crystal, opposite of the piezoelectric actuator.
12. Place the static load cell with the teflon holder behind the soft linear spring (with respect to the piezoelectric actuator). Connect the two reference voltage inputs of the static load cell to the 5 V DC source on the DAQ board. Connect the two measurement outputs of the static load cell to the voltmeter.
13. If used, insert the fourth (or third and fourth) polycarbonate guide rod.
14. Position the second steel boundary block behind the static load cell so that the linear spring and the crystal are compressed. Measure the static load applied with the static load cell (displayed on the voltmeter). Fix the steel boundary block to the optical table when the desired static load is reached.
15. In any MATLAB code used to drive the data acquisition: set the gains, the number and names of any input and output channels, and the sampling rate (as described in previous sections).
16. The signal generation and measurement (via the DAQ board) can now be conducted nearly simultaneously across all channels (the input channels are multiplexed, such that they are sampled sequentially at the DAQ board maximum sample rate, and the signals are recorded at the user specified sampling frequency). The measured signals (including the feedback from the output channel) can now be recorded via MATLAB and post processed as desired.
17. Acquire data without any driving signal to assure that all sensors have discharged and reached a steady static value (repeat this step before any data acquisition).
18. Conduct a calibration run using the signals to be used in the specific experiment. Make sure the gains and the DAQ input voltage ranges are set so that

the acquired signal voltages closely match the DAQ input voltage ranges. Include a check in the data acquisition code to make sure the voltage range is not approached and exceeded by the acquired signals.

19. To characterize the linear spectrum of the granular crystal: apply a long-time (1 to 2 seconds) low-amplitude (compared to the static load [greater than 1%]) bandwidth-limited noise signal via the piezoelectric actuator. Linearly ramp the generated signal at the beginning and end to minimize transient response. Repeat over multiple iterations (greater than 8). In post-processing, calculate the PSD of a time-window which avoids transients caused by turning on and off the signal, for each repetition. The PSD can be normalized by the measured signal voltage (from the DAQ board output feedback channel) and averaged (in the frequency domain) over all repetitions. The spectrum can then be normalized by the average PSD level in the transmitting bands.
20. To characterize any other relevant phenomena, a similar procedure can be used as in the previous step, however the generated signal can be replaced with any other arbitrary signal (as described in each of the following chapters).

1.9 Numerical Tools

As will be seen in the subsequent chapters, several numerical tools were used in conjunction with the experiments. These include numerical calculation of the eigen-frequencies and eigen-modes for the linearized system, numerical calculation of the transfer function of the linearized system based on the state space formulation, genetic optimization algorithms, 4th order Runge-Kutta integration of the fully nonlinear equations of motion, and Newton-Raphson parameter continuation.

The eigen-frequencies and eigen-modes were calculated using MATLAB's (R2008b) *eig* function. The transfer function of the linearized system in state space formulation was calculated using MATLAB's (R2008b) *bode* and *ss* (using an experimentally derived frequency discretization) functions.

The numerical simulations using the 4th-order Runge-Kutta integration of the fully nonlinear equations of motion (equation 1.9) were predominantly carried out by collaborators (G. Theocharis). The integration time-step was selected by ensuring the long-time conservation of energy in the conservative simulations, and by checking for a smooth response. This time-step was then used in the nonconservative simulations. The Newton-Raphson continuations shown in this thesis were also carried out by collaborators (G. Theocharis).

1.10 Conceptual Organization of This Thesis

The remainder of the thesis is organized as follows: each chapter is a stand-alone published (under review, or in preparation for submission) journal article [5, 143, 144, 148, 149] relating to 1D statically compressed granular crystals. Consequently, each chapter is conceptually grouped according to regime of dynamic response and particular phenomena investigated. The necessary background for each chapter is included in its introduction, and the notation for each chapter differs slightly. The citation for the paper on which each chapter is based is provided at the end of each chapter, along with a short summary of the contributions of each co-author.

In chapter 2 we describe how an increased degree of periodicity, in granular crystal systems (operating in the near-linear dynamical regime), enables new ways to tune the frequency filtering response of the crystal. We show the first experimental demonstration of three bands of propagation (with two finite gaps), their tunability with static load, and how the resulting dispersion relation can be engineered by changing the mass of a single particle in the unit cell. In chapter 3 we show the first experimental demonstration of discrete breathers occurring in granular crystals (weakly nonlinear dynamical regime). In chapter 4 we follow this with a longer numerical work characterizing the existence and stability of two discrete breather families (one of which the discrete breather of the previous chapter falls into), throughout the gap of a linear spectrum. We describe how, because of the tensionless characteristic of our system, the granular crystal supports a type of discrete breather (different from that

occurring in other nonlinear systems without this additional degree of nonlinearity) which closely resembles a nonlinear analog of the linear surface mode known to exist for this type of periodicity crystal. In chapter 5, we present a systematic experimental study of defect modes in granular crystals. Defect modes had already experimentally been shown to exist in uncompressed granular crystals experiencing temporary linearization in the neighborhood of a defect interacting with a solitary wave [118], and numerically shown to occur in weakly nonlinear granular crystals in [136]. Our investigation is the first to experimentally characterize these defect modes in statically compressed crystals using continuous vibrations and spectral analysis. In particular we experimentally describe the interplay of two defects in close spatial proximity, and show the nonlinear frequency shift due to an increased degree of nonlinearity under impulsive loading conditions. Finally, in chapter 6 we demonstrate a novel method of bifurcation-based phononic switching and rectification, utilizing a granular crystal system. We describe the bistable transition from a low amplitude nontransmitting periodic state to high amplitude transmitting quasiperiodic and chaotic states.

Chapter 2

Tunable Band Gaps in Diatomic Granular Crystals with Three-Particle Unit Cells

We investigate the tunable vibration filtering properties of statically compressed one-dimensional diatomic granular crystals composed of arrays of stainless steel spheres and cylinders interacting via Hertzian contact. The arrays consist of periodically repeated three-particle unit cells (sphere-cylinder-sphere) in which the length of the cylinder is varied systematically. We investigate the response of these granular crystals, given small amplitude dynamic displacements relative to those due to the static compression, and characterize their linear frequency spectrum. We find good agreement between theoretical dispersion relation analysis (for infinite systems), state-space analysis (for finite systems), and experiments. We report the observation of up to three distinct pass bands and two finite band gaps and show their tunability for variations in cylinder length and static compression.

2.1 Introduction

The presence of band gaps, a characteristic of wave propagation in periodic structures, has been studied in a wide array of settings involving phononic/photonic crystals [12, 28, 36, 150] and plasmonics [31]. Materials exhibiting band gaps are of particular interest as they forbid and allow the propagation of waves in selected frequency

ranges (pass and stop bands), and in the case of elastic wave propagation (in composites or multilayered structures) have previously been proposed for use in acoustic filters/vibration isolation applications [1, 40, 43], and rectification of acoustic energy flux [45].

Chains composed of elastic particles in close contact with each other, or “granular crystals,” have gained much recent attention with respect to elastic wave propagation in nonlinear media. The nonlinearity in granular crystals results from the Hertzian contact between two elastic spherical (or spherical and cylindrical) particles in compression and from a zero tensile strength [84]. The contact stiffness is defined by the geometry and material properties of the particles in contact [84]. In this type of system, the dynamic response can be tuned to encompass linear, weakly nonlinear, and strongly nonlinear regimes, by varying the relative amplitudes of the dynamic disturbances and the static compression [21, 138]. This simple means of controlling their dynamic response has made granular crystals a useful test bed for the study of nonlinear phenomena, including coherent structures such as solitary waves [21, 102], discrete breathers [5, 148], shock waves [134], and linear/nonlinear defect modes [118, 136]. Additionally, granular crystals have been shown to be useful in engineering applications, including shock and energy absorbing layers [99, 100, 138, 139], actuating devices [140], acoustic lenses [141] and sound scramblers [127, 128].

Previous studies involving statically compressed granular crystals, composed of one-dimensional (1D) periodic (monoatomic and diatomic with a two particle unit cell) arrays of glued [108], welded [109], and elastically compressed spherical particles [5, 110, 137, 151], have been shown to exhibit tunable vibrational band gaps. In this chapter, we study statically compressed 1D diatomic granular crystals composed of periodic arrays of stainless steel sphere-cylinder-sphere unit cells. We employ theoretical models to estimate the dispersion relation of the crystals, we numerically validate their dynamic response using state-space analysis, and we verify experimentally the crystal’s acoustic transmission spectrum. For such configurations, we experimentally report the presence of a third distinct pass band and a second finite band gap. We show tunability and customization of the response, for variation of the cylinder length

and static compression.

2.2 Experimental Setup

We assemble five different 1D diatomic granular crystals composed of three-particle, sphere-cylinder-sphere, repeating unit cells as shown in figure 2.1(a). The chains are 21 particles (7 unit cells) long. The particles (spheres and cylinders) are made from 440C stainless steel, with radius $R = 9.53$ mm, elastic modulus $E = 200$ GPa, and Poisson's ratio $\nu = 0.3$ [3]. Each of the five chains is assembled with cylinders of a different length, $L = [9.4, 12.5, 15.8, 18.7, 21.9]$ mm. The mass of the spherical particles is measured to be $m = 27.8$ g and the mass of the cylindrical particles is measured to be $M = [20.5, 27.3, 34.1, 40.7, 47.8]$ g for each of the corresponding cylinder lengths.

We align the spheres and cylinders, cleaned with isopropanol, in a horizontal 1D configuration using a containment structure of four polycarbonate rods (12.7 mm diameter). We hold the polycarbonate rods in place with polycarbonate guide plates spaced at intervals of 1 unit cell. We apply low amplitude broadband noise to the granular crystals using a piezoelectric actuator mounted on a steel cube of height 88.9 mm, which is fixed to the table. We visualize the evolution of the force-time history of the propagating excitations using a calibrated dynamic force sensor. The force sensor is composed of a piezoelectric disk embedded with epoxy inside two halves of a $R = 9.53$ mm, 316 stainless steel sphere (of elastic modulus 193 GPa, and a Poisson ratio of 0.3 [3]). The sensor is constructed so as to approximate the mass, shape, and contact properties of the spherical particles in the rest of the crystal [127, 128, 138, 145]. The assembled force sensor is calibrated against a commercial dynamic force sensor, and has a measured total mass and resonant frequency of 28.0 g and 80 kHz, respectively. We insert the dynamic force sensor in place of the last particle, located at the opposite end of the crystal from the actuator. We condition its output with a 30 kHz cutoff 8-pole butterworth low-pass filter and voltage amplifier.

At the opposite end of the crystal with respect to the piezoelectric actuator, we apply a static compressive force, F_0 , using a soft (compared to the contact stiffness of the particles) stainless steel linear compression spring (stiffness 1.24 kN/m). In this case, we can approximate this boundary as a free boundary. The static compressive force applied to the chain is adjusted by positioning, and fixing to the table, a movable steel cube of height 76.2 mm so that the soft linear spring is compressed. The resulting applied static load is measured with a static load cell placed in between the steel cube and the spring.

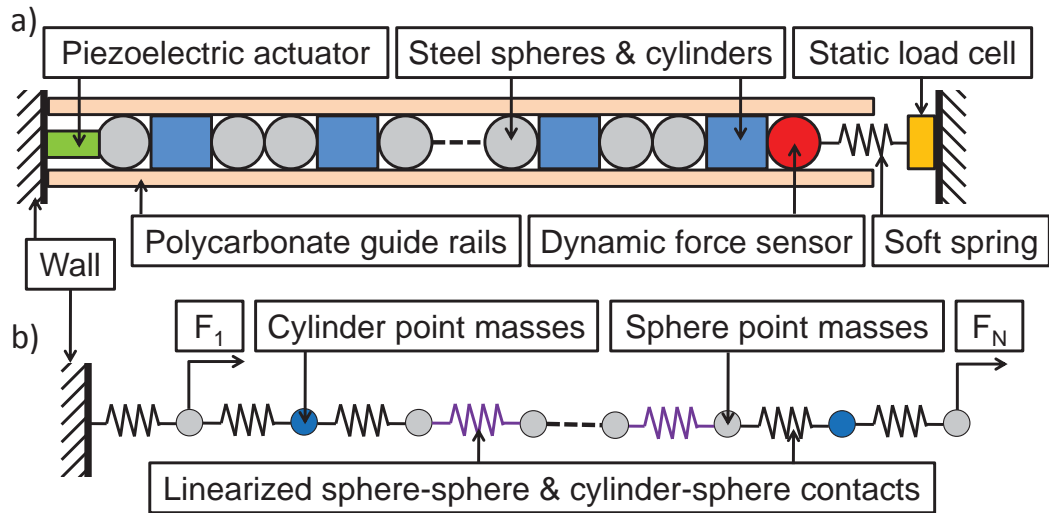


Figure 2.1: (a) Schematic of experimental setup. (b) Schematic of the linearized model of the experimental setup.

2.3 Theoretical Discussion

2.3.1 Dispersion Relation

We model a 1D diatomic crystal composed of n sphere-cylinder-sphere unit cells (and N particles) as a chain of nonlinear oscillators [21]:

$$m_l \ddot{u}_l = \alpha_{l-1,l} [\delta_{l-1,l} + u_{l-1} - u_l]_+^p - \alpha_{l,l+1} [\delta_{l,l+1} + u_l - u_{l+1}]_+^p, \quad (2.1)$$

where $[Y]_+$ denotes the positive part of Y ; the bracket takes the value Y if $Y > 0$, and 0 if $Y \leq 0$. This represents the tensionless characteristic of our system; when adjacent particles are not in contact, there is no force between them. The above model assumes that the particles act as point masses. This is valid as long as the frequencies of the applied vibrations are much lower than the frequencies of the natural vibrational modes of the individual particles [111]. Here, u_l is the displacement of the l th particle around the static equilibrium, $\delta_{l-1,l}$ is the static overlap between the $(l-1)$ th and the l th particles, and m_l is the mass of the l th particle (where l is the index of the l th particle in the chain counted from the piezoelectric actuator end, and $l \in \{1, \dots, 3n\}$). As per Hertz's contact law, the coefficients α depend on the geometry and material properties of the adjacent particles and on the exponent p (here $p = 3/2$) [84]. Here, in the case of the sphere-cylinder-sphere unit cell, we need to account for two different values of the contact coefficients α , corresponding to the sphere-cylinder and the sphere-sphere contacts, where:

$$\alpha_{sphere,cylinder} = \alpha_{cylinder,sphere} = A_1 = \frac{2E\sqrt{R}}{3(1-\nu^2)}, \quad (2.2)$$

$$\alpha_{sphere,sphere} = A_2 = \frac{E\sqrt{2R}}{3(1-\nu^2)}. \quad (2.3)$$

For this case, it can be seen that $A_1 = \sqrt{2}A_2$. Furthermore, for Hertzian contacts, under a static load F_0 , we can define the static overlap for the sphere-cylinder

contact as $\delta_{sphere,cylinder} = \delta_{cylinder,sphere} = (F_0/A_1)^{2/3}$, and for the sphere-sphere contact as $\delta_{sphere,sphere} = (F_0/A_2)^{2/3}$ [21, 84]. Considering small amplitude dynamic displacements, as compared to the static overlap, one can linearize the equations of motion (equation 2.1). For the studied sphere-cylinder-sphere unit cell, the particles' linearized equations of motion are:

$$\begin{aligned} m\ddot{u}_{3j-2} &= \beta_2[u_{3j-3} - u_{3j-2}] - \beta_1[u_{3j-2} - u_{3j-1}], \\ M\ddot{u}_{3j-1} &= \beta_1[u_{3j-2} - u_{3j-1}] - \beta_1[u_{3j-1} - u_{3j}], \\ m\ddot{u}_{3j} &= \beta_1[u_{3j-1} - u_{3j}] - \beta_2[u_{3j} - u_{3j+1}], \end{aligned} \tag{2.4}$$

where j is the number of the j th unit cell ($j \in \{1, \dots, n\}$), m is the mass of a spherical particle, M is the mass of a cylindrical particle, $\beta_1 = \frac{3}{2}A_1^{2/3}F_0^{1/3}$ is the linearized stiffness between a spherical and cylindrical particle, and $\beta_2 = \frac{3}{2}A_2^{2/3}F_0^{1/3}$ is the linearized stiffness between two spherical particles. The dispersion relation for a diatomic (two particle unit cell) granular crystal is known to contain two branches (*acoustic* and *optical*) [137]. Here we use a similar procedure to calculate the dispersion relation for a diatomic crystal with a three particle unit cell.

We substitute the following traveling wave solutions into equations (2.4):

$$\begin{aligned} u_{3j-2} &= Ue^{i(kaj+\omega t)}, \\ u_{3j-1} &= Ve^{i(kaj+\omega t)}, \\ u_{3j} &= We^{i(kaj+\omega t)}, \end{aligned} \tag{2.5}$$

where k is the wave number, ω is the angular frequency, and $a = L+4R-2\delta_{sphere,cylinder}-\delta_{sphere,sphere}$ is the equilibrium length of the sphere-cylinder-sphere unit cell. U , V , and W are the wave amplitudes, and are constructed complex so as to contain both the amplitude and phase difference for each particle within the unit cell. Solving for

a nontrivial solution we obtain the following dispersion relation:

$$\begin{aligned}
0 = & -2\beta_1^2\beta_2 + \beta_1(\beta_1 + 2\beta_2)(2m + M)\omega^2 \\
& - 2m(\beta_2M + \beta_1(m + M))\omega^4 \\
& + m^2M\omega^6 + 2\beta_1^2\beta_2\cos ak).
\end{aligned} \tag{2.6}$$

In figure 2.2 (a), we plot the dispersion relation (equation 2.6) for the previously described sphere-cylinder-sphere unit cell granular crystal, with cylinder length $L = 12.5$ mm ($M = 27.3$ g), subject to an $F_0 = 20$ N static load. Three bands of solutions (or propagating frequencies) can be seen; the lowest in frequency being the acoustic band, followed by lower and upper optical bands. Frequencies in between these bands are said to lie in a band gap (or forbidden band). Waves at these frequencies are evanescent, decay exponentially, and cannot propagate throughout the crystal [12].

If we solve the dispersion relation, equation (2.6), for when $k = \frac{\pi}{a}$ and $k = 0$ we obtain the following cutoff frequencies:

$$\begin{aligned}
f_{c,1}^2 &= 0, \\
f_{c,2}^2 &= \frac{\beta_1 + 2\beta_2}{4\pi^2m}, \\
f_{c,3}^2 &= \frac{\beta_1(2m + M)}{4\pi^2mM}, \\
f_{c,4}^2 &= \frac{\beta_1}{4\pi^2m}, \\
f_{c,5}^2 &= \frac{\beta_1(2m + M) + 2\beta_2M}{8\pi^2mM} \\
&\quad - \frac{\sqrt{-16\beta_1\beta_2mM + (2\beta_1m + \beta_1M + 2\beta_2M)^2}}{8\pi^2mM}, \\
f_{c,6}^2 &= \frac{\beta_1(2m + M) + 2\beta_2M}{8\pi^2mM} \\
&\quad + \frac{\sqrt{-16\beta_1\beta_2mM + (2\beta_1m + \beta_1M + 2\beta_2M)^2}}{8\pi^2mM},
\end{aligned} \tag{2.7}$$

where $f_{c,1}$, $f_{c,2}$, and $f_{c,3}$ correspond to $k = 0$ and $f_{c,4}$, $f_{c,5}$, and $f_{c,6}$ to $k = \frac{\pi}{a}$. In figure 2.2 (a), we label the six cutoff frequencies (equations 2.7) for the previously described granular crystal.

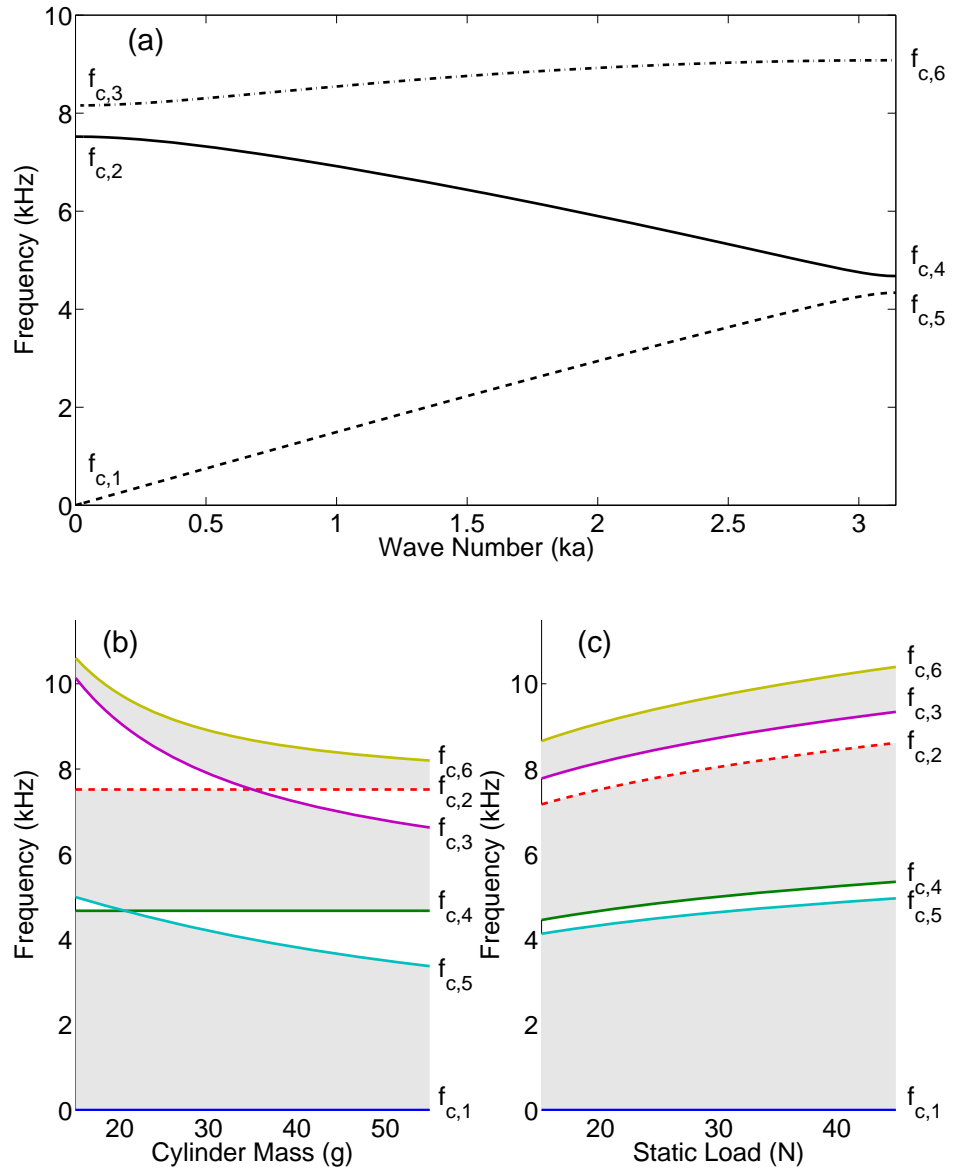


Figure 2.2: (a) Dispersion relation for the described sphere-cylinder-sphere granular crystal with cylinder length $L = 12.5$ mm ($M = 27.3$ g) subject to an $F_0 = 20$ N static load. The acoustic branch is the dashed line, the lower optical branch is the solid line, and the upper optical branch is the dash-dotted line. Cutoff frequencies for granular crystals corresponding to our experimental configuration (b) varying the length L (and thus mass) of the cylinder with fixed $F_0 = 20$ N static compression, and (c) varying the static compression ($F_0 = [20, 25, 30, 35, 40]$ N) with fixed $L = 12.5$ mm cylinder length ($M = 27.3$ g). Solid lines represent the six cutoff frequency solutions. $f_{c,2}$ is dashed to clarify the nature of the intersection with $f_{c,3}$. Shaded areas are the propagating bands.

From equations 2.7, it can be seen that the cutoff frequencies are tunable through the variation of particle masses m and M , and the linearized stiffnesses β_1 and β_2 (thus tunable with changes in geometry, and static compression F_0). In figure 2(b) we plot the cutoff frequencies in equations (2.7) as a function of cylinder length for fixed $F_0=20$ N static compression, and in figure 2(c) as a function of static compression ($F_0 = [20, 25, 30, 35, 40]$ N) for fixed cylinder length $L = 12.5$ mm ($M = 27.3$ g). The lines represent the cutoff frequency solutions ($f_{c,2}$ is dashed to clarify the nature of the intersection with $f_{c,3}$, and the shaded areas are the pass bands). It can be seen that within our frequency range of interest, two of the cutoff frequency solutions coincide at specific cylinder lengths. The intersection between $f_{c,4}$ and $f_{c,5}$ can be found to occur at $M/m = \frac{\beta_1}{\beta_2}$ and the intersection between $f_{c,2}$ and $f_{c,3}$ at $M/m = (2 - \frac{\beta_1}{\beta_2})$. Notice, however, that aside from these special parameter values where the above intersections occur, the spectrum preserves the three pass bands with two associated finite bandgaps between them.

2.3.2 State-space Approach

In addition to the dispersion relation previously calculated for an infinite system, we study the finite linearized system corresponding to our experimental setup as shown in figure 2.1(b). We model the actuator boundary of our system as a fixed 440C steel wall. We model the other end of the chain as a free boundary, as the stiffness of the spring used for static compression is much less than the characteristic stiffness of the particles in contact. The linearized equations of motion for the finite system are the same as equations (2.4), except the equations for the first and last particles which are given by the following expressions:

$$\begin{aligned} m\ddot{u}_1 &= F_1 - \beta_1[u_1] - \beta_1[u_1 - u_2], \\ m\ddot{u}_{21} &= \beta_1[u_{20} - u_{21}], \end{aligned} \tag{2.8}$$

where F_1 is the force applied to the first particle by the actuator. Next, we apply the state-space approach, using the following formulation [9]:

$$\begin{aligned}\dot{\mathbf{x}} &= \mathbf{A}\mathbf{x} + \mathbf{B}F_1, \\ F_N &= \mathbf{C}\mathbf{x} + \mathbf{D}F_1,\end{aligned}\tag{2.9}$$

where \mathbf{x} is the state vector. Matrices \mathbf{A} , \mathbf{B} , \mathbf{C} , and \mathbf{D} are called state, input, output and direct transmission matrices, respectively. Here, \mathbf{D} is a zero matrix (size 1×1). We choose as an input to the system the force F_1 , and as an output $F_N = \frac{\beta_1[u_{20} - u_{21}]}{2}$, the averaged force of the two contacts of the last particle (which is analogous to what is measured by the embedded dynamic force sensor in our experimental setup) [127, 128, 138, 145]. Thus, for the linear system of figure 2.1(b), we obtain:

$$\mathbf{x} = \begin{pmatrix} u_1 \\ \vdots \\ u_{N-1} \\ u_N \\ \dot{u}_1 \\ \vdots \\ \dot{u}_N \end{pmatrix},$$

$$\mathbf{A} = \left(\begin{array}{c|c} \mathbf{0} & \mathbf{I} \\ \hline \mathbf{M}^{-1}\mathbf{K} & \mathbf{0} \end{array} \right),$$

$$\mathbf{B} = \begin{pmatrix} 0 \\ \vdots \\ 0 \\ 1/m \\ 0 \\ \vdots \\ 0 \end{pmatrix},$$

$$\mathbf{C} = \left(0 \quad \dots \quad \frac{\beta_1}{2} \quad -\frac{\beta_1}{2} \quad 0 \quad \dots \quad 0 \right),$$

where, $\mathbf{0}$ is a zero matrix and \mathbf{I} is the identity matrix (both of size $N \times N$). The mass matrix \mathbf{M} , and the stiffness matrix \mathbf{K} are defined as follows:

$$\mathbf{M} = \begin{pmatrix} m & 0 & 0 & \dots & 0 & 0 & 0 \\ 0 & M & 0 & \dots & 0 & 0 & 0 \\ 0 & 0 & m & \dots & 0 & 0 & 0 \\ \vdots & \vdots & \vdots & \ddots & \vdots & \vdots & \vdots \\ 0 & 0 & 0 & \dots & m & 0 & 0 \\ 0 & 0 & 0 & \dots & 0 & M & 0 \\ 0 & 0 & 0 & \dots & 0 & 0 & m \end{pmatrix},$$

$$\mathbf{K} = \begin{pmatrix} -2\beta_1 & \beta_1 & 0 & 0 & 0 & \dots & 0 & 0 & 0 \\ \beta_1 & -2\beta_1 & \beta_1 & 0 & 0 & \dots & 0 & 0 & 0 \\ 0 & \beta_1 & -\beta_1 - \beta_2 & \beta_2 & 0 & \dots & 0 & 0 & 0 \\ 0 & 0 & \beta_2 & -\beta_2 - \beta_1 & \beta_1 & & 0 & 0 & 0 \\ \vdots & \vdots & & & \ddots & & & \vdots & \vdots \\ 0 & 0 & 0 & & \beta_1 & -\beta_1 - \beta_2 & \beta_2 & 0 & 0 \\ 0 & 0 & 0 & \dots & 0 & \beta_2 & -\beta_2 - \beta_1 & \beta_1 & 0 \\ 0 & 0 & 0 & \dots & 0 & 0 & \beta_1 & -2\beta_1 & \beta_1 \\ 0 & 0 & 0 & \dots & 0 & 0 & 0 & \beta_1 & -\beta_1 \end{pmatrix}.$$

We use the formulation in equations 2.9, with MATLAB's (R2008b) *bode* func-

tion, to compute the bode diagram of the frequency response for the experimental configurations described. The bode diagram is the magnitude of the transfer function $H(s) = D + \mathbf{C}(s\mathbf{I} - \mathbf{A})^{-1}\mathbf{B}$, where $s = i\omega$ [9]. We plot the bode transfer function, $|H(i\omega)|$, for the five previously described diatomic (three-particle unit cell) chains with varied cylinder length for fixed $F_0=20$ N static compression, (figure 2.3(a)), and with varied static compression ($F_0 = [20, 25, 30, 35, 40]$ N) for fixed cylinder length $L = 12.5$ mm ($M = 27.3$ g) (figure 2.3(b)).

We truncate the visualization in figure 2.3 below -40 dB and above 20 dB as a visual aid to maintain clarity of the frequency region of interest. This resembles experimental conditions, as the noise floor of our measurements is approximately -38 dB (as can be seen in figure 2.4) and the presence of dissipation in our experiments reduces the sharpness of the resonant peaks in contrast to those predicted by the state-space analysis. Attenuating and propagating frequency regions for this formulation match well with the cutoff frequencies of the infinite system (see equations (2.7)), denoted by the solid lines plotted in figure 2.3. The high amplitude (bright) peaks correspond to the eigenfrequencies of the system, the modes of which are spatially extended. However, for certain cylinder lengths, we also observe eigenfrequencies located in the second gaps of the linear spectra (denoted by the arrows in figure 2.3(a)). These modes result from the break in periodicity due to the presence of the actuator “wall” (acting like a defect in the system). In our setup (see figure 2.1(b)), it can be seen that the first particle (which is spherical) is coupled to both its nearest neighbors via springs characterized by spherical-planar contact (β_1). This is unique within the chain and forms a type of locally supported defect mode. When the frequency of this mode lies within a band gap the mode becomes spatially localized around the first particle and its amplitude decays exponentially into the chain. Furthermore, as our chains are relatively short and the gap that the localized modes occupy relatively narrow (in frequency), the spatial profile is found to be almost similar to the extended modes. This suggests that it may be experimentally difficult to differentiate these modes from their extended counterparts.

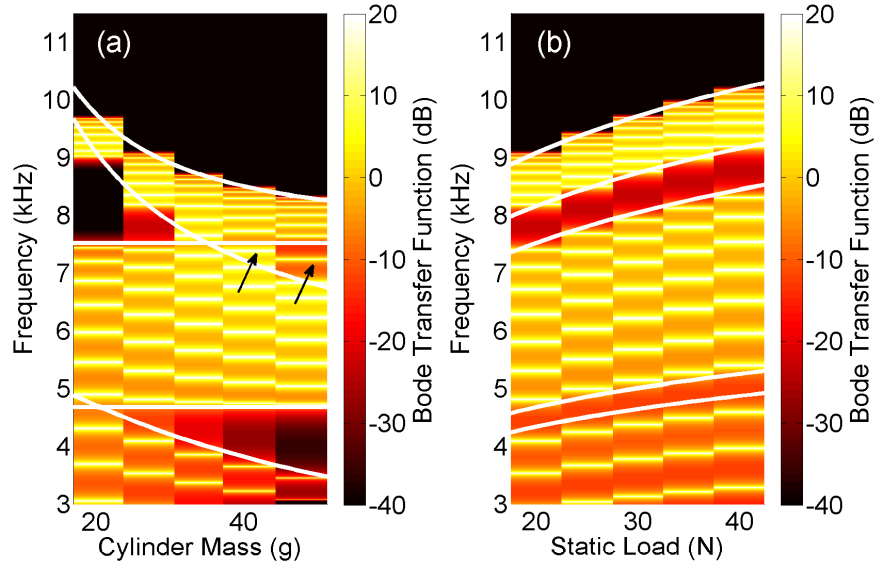


Figure 2.3: Bode transfer function ($|H(i\omega)|$) for the experimental configurations: (a) the five diatomic (three-particle unit cell) granular crystals with varied cylinder length for fixed $F_0 = 20$ N static compression, and (b) the fixed cylinder length $L = 12.5$ mm ($M = 27.3$ g) granular crystal with varied static load. Solid white lines are the cutoff frequencies calculated from the dispersion relation of the infinite system. The black arrows in (a) denote the eigenfrequencies of defect modes.

2.4 Experimental Linear Spectrum

We experimentally characterize the linear spectrum of the previously described diatomic chains with sphere-cylinder-sphere unit cells for varied cylinder length and static load. We apply a low-amplitude (approximately 200 mN peak) bandwidth limited (3 – 15 kHz) noise excitation with the piezoelectric actuator. We measure the dynamic force using a sensor embedded in the last particle of the granular crystal as shown in figure 2.1. We compute the power spectral density (PSD [147]) of the measured dynamic force history over 1.3 s intervals, and average the PSD over 16 acquisitions. We normalize the averaged PSD spectrum by the average PSD level in the 3 – 7.5 kHz range of the $L = 12.5$ mm ($M = 27.3$ g), $F_0 = 20$ N granular crystal response to obtain the transfer functions shown in figure 2.4 and figure 2.5. More specifically, figure 2.4 shows the experimental transfer function in more detail for the $L = 12.5$ mm ($M = 27.3$ g), $F_0 = 20$ N granular crystal.

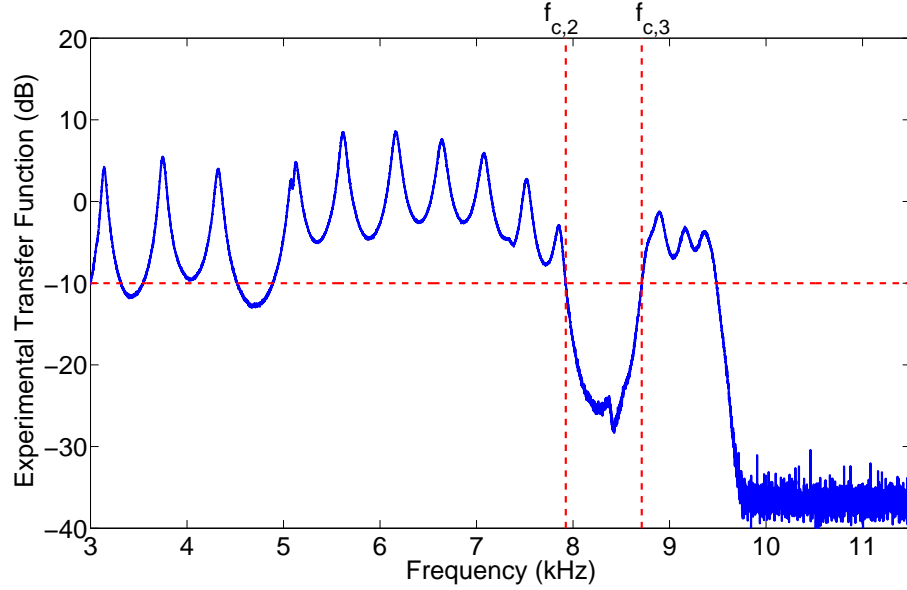


Figure 2.4: Experimental transfer function for the $L = 12.5$ mm ($M = 27.3$ g), $F_0 = 20$ N granular crystal. The horizontal dashed line is the -10 dB level used to experimentally determine the $f_{c,2}$ and $f_{c,3}$ band edges which are denoted by the vertical dashed lines.

As in [5], we observe that the experimentally determined spectra are upshifted in frequency from the theoretically derived spectra for all configurations tested. Because of this we use the measured spectra to extract the effective elastic properties of our system. For the $F_0 = [20, 25, 30, 35, 40]$ N, fixed cylinder length $L = 12.5$ mm ($M = 27.3$ g) granular crystals, we measure the frequencies of the -10 dB level of the PSD transfer function corresponding to the second band gap ($f_{c,2}$ and $f_{c,3}$). We use these experimentally determined frequencies to solve for two average, experimentally determined, Hertzian contact coefficients of our system $A_{1,exp}$ and $A_{2,exp}$ using the previously described equations for A_1 , A_2 , β_1 , β_2 , $f_{c,2}$, and $f_{c,3}$. An example of the determination of $f_{c,2}$ and $f_{c,3}$, for the $L = 12.5$ mm ($M = 27.3$ g), $F_0 = 20$ N granular crystal, is shown in figure 2.4. We compare the experimentally determined $A_{1,exp}$ and $A_{2,exp}$ to the theoretically determined A_1 and A_2 in Table 4.1 (error ranges indicate the standard deviation resulting from the measurements at the five different static loads). As the equations for the five non-zero cutoff frequencies (see equations 2.7) in our granular crystals are dependent on some combination of A_1 and A_2 , the choice

	A_1 [$\text{N}/\mu\text{m}^{3/2}$]	A_2 [$\text{N}/\mu\text{m}^{3/2}$]
Theory	14.30	10.11
Experiments	18.04 ± 0.44	11.48 ± 0.06

Table 2.1: Hertz contact coefficients derived from standard specifications [3] (A_1 and A_2) versus coefficients derived from the measured frequency cutoffs ($A_{1,\text{exp}}$ and $A_{2,\text{exp}}$), for the ($F_0 = [20, 25, 30, 35, 40]$ N) fixed cylinder length $L = 12.5$ mm ($M = 27.3$ g) granular crystals.

of using $f_{c,2}$ and $f_{c,3}$ to solve for A_1 and A_2 is not unique and other combinations of cutoff frequencies could be used similarly.

In previous work [5], numerous possible explanations for the upshift in the spectrum were identified. We include these possible explanations, along with some further additions, in the following list. While still adhering to Hertzian behavior, uncertainty in the standard values of material parameters [3] or deviations in the local radius of curvature due to surface roughness could result in the material behaving more stiffly [103]. In addition, there exist several factors which could cause deviations from Hertzian behavior, and result in a shift in the exponent p or in the effective contact coefficient A . These factors include the dynamic loading conditions [84], non-Hookean elastic dynamics or dissipative mechanisms (nonlinear elasticity, plasticity, viscoelasticity, or solid friction) [84, 103, 116, 133], or small amounts of oil from handling near the contact area [117]. A non-planar contact area, resulting from a small misalignment of the particle centers, the previously mentioned non-Hookean elastic dynamics, or dissipative mechanisms, could also cause non-Hertzian behavior [103]. We also observe that the contact coefficient A between the cylindrical and spherical particles has the larger deviation from theory. This deviation could be attributed mainly to the cylindrical particles, due to characteristics not shared by the spherical particles. Such characteristics could include surface roughness particular to the manufacturing process of the cylindrical particles, or plastic deformation occurring closer to the surface as compared to spherical particles.

In figure 2.5, we plot the experimentally determined PSD transfer functions for the five previously described diatomic (three-particle unit cell) chains with varied cylinder

length for fixed $F_0=20$ N static compression (figure 2.5(a)), and static compression $F_0 = [20, 25, 30, 35, 40]$ N, for fixed cylinder length $L = 12.5$ mm ($M = 27.3$ g) (figure 2.5(b)). We plot with solid white lines the cutoff frequencies from the dispersion relation calculated using the experimentally determined Hertz contact coefficients $A_{1,exp}$ and $A_{2,exp}$. We observe good agreement between the semi-analytically derived cutoffs (i.e, from the theoretical dispersion relation but using $A_{1,exp}$ and $A_{2,exp}$) and the experimental spectra. By comparing figure 2.5 to figure 2.3, we observe good qualitative agreement between the numerical (state-space) and experimental spectra. Comparing the experimentally and theoretically determined cutoff frequencies, we observe an average (over all experimental configurations) upshift in the experimental frequency cutoffs versus the theoretically determined frequency cutoffs of: 5.8% in $f_{c,2}$, 8.1% in $f_{c,3}$, 8.1% in $f_{c,4}$, 5.4% in $f_{c,5}$, and 7.0% in $f_{c,6}$.

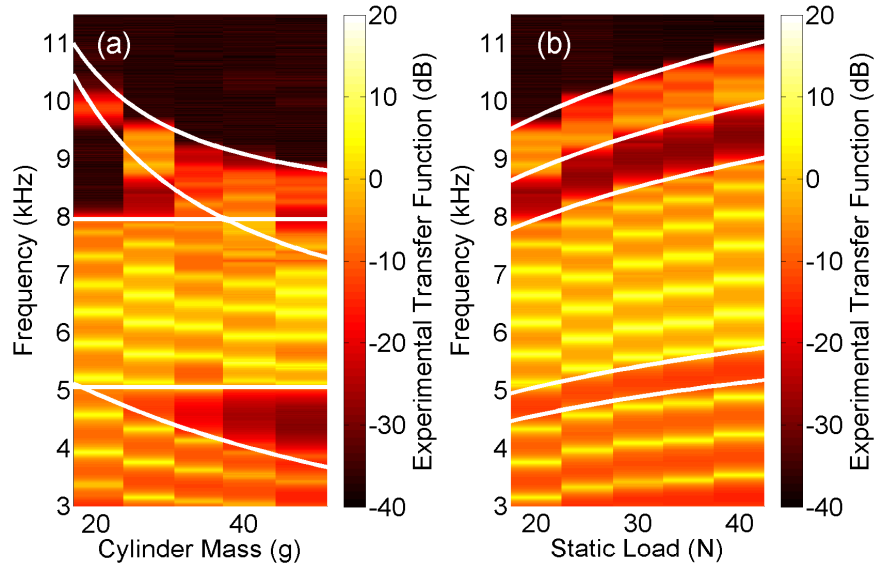


Figure 2.5: Experimental PSD transfer functions for the experimental configurations described in figure 2.3. (a) The five diatomic (three-particle unit cell) granular crystals with varied cylinder length for fixed $F_0=20$ N static compression, and (b) the fixed cylinder length $L = 12.5$ mm ($M = 27.3$ g) granular crystal with varied static load. Solid white lines are the cutoff frequencies from the dispersion relation using experimentally determined Hertz contact coefficients $A_{1,exp}$ and $A_{2,exp}$.

The demonstrated attenuation of the elastic wave propagation in frequency regions

lying within the band gaps of the granular crystals shows that such systems have potential for use in a wide array of vibration filtering applications. Furthermore, the tunability displayed (achievable from material selection, shape, size, periodicity, and application of static compression) offers significant potential for attenuating a wide spectrum of undesired frequencies.

2.5 Conclusions

In this work, we describe the tunable vibration filtering properties of a 1D granular crystal composed of periodic arrays of three-particle unit cells. The unit cells are assembled with elastic beads and cylinders that interact via Hertzian contact. Static compression is applied to linearize the dynamics of particles interaction and to tune the frequency ranges supported by the crystal. We measure the transfer functions of the crystals using state-space analysis and experiments, and we compare the results with the corresponding theoretical dispersion relations. Up to three distinct pass bands and three (two finite) band gaps are shown to exist for selected particle configurations. The tunability of the band edges in the crystal's dispersion relation is demonstrated by varying the applied static load and the cylinder length.

In the present work, we restrict our considerations to the study of near linear, small amplitude excitations. A natural extension of this work would involve the examination of nonlinear excitations within the bandgaps of such granular chains [5]. In particular, it would be relevant to compare the properties of localized nonlinear waveforms in different gaps of the linear spectrum. Such studies will be reported in future publications.

2.6 Author Contributions

This chapter is based on [143]. G.T., P.G.K., and C.D. proposed the study. G.T. developed the three-particle unit cell dispersion relation. J.Y. developed the initial state space implementation and participated in the early experimental work and computational analysis. N.B. designed and conducted the final experiments, the data analysis, the final analytic and computational analysis, and wrote the paper. G.T. and C.D. provided guidance and contributed to the analysis throughout the project. All authors contributed to editing the manuscript and provided intellectual contribution.

Chapter 3

Discrete Breathers in Diatomic Granular Crystals

We report the experimental observation of modulational instability and discrete breathers in a one-dimensional diatomic granular crystal composed of compressed elastic beads that interact via Hertzian contact. We first characterize their effective linear spectrum both theoretically and experimentally. We then illustrate theoretically and numerically the modulational instability of the lower edge of the optical band. This leads to the dynamical formation of long-lived breather structures, whose families of solutions we compute throughout the linear spectral gap. Finally, we experimentally observe the manifestation of the modulational instability and the resulting generation of localized breathing modes with quantitative characteristics that agree with our numerical results.

3.1 Introduction

Intrinsic localized modes (ILMs), or discrete breathers (DBs), have been a central theme in numerous theoretical and experimental investigations during the past two decades [19, 51, 53–55]. Their original theoretical proposal in settings such as anharmonic nonlinear lattices [56, 57] and the rigorous proof of their existence under fairly general conditions [58] motivated studies of such modes in a diverse host of applications, including charge-transfer solids [59], antiferromagnets [60], superconducting Josephson junctions [61, 62], photonic crystals [36], biopolymers [63, 64], microme-

chanical cantilever arrays [65], and more.

Granular crystals, which consist of closely packed ensembles of elastically interacting particles, have also recently drawn considerable attention. This broad interest has arisen from their tunable dynamic response encompassing linear, weakly nonlinear, and strongly nonlinear regimes [21, 116]. Such flexibility, arising from the nonlinear contact interaction between particles, makes them ideal not only as toy models for probing the physics of granular materials but also for the implementation of engineering applications, including shock and energy absorbing layers [99, 100, 115, 138, 139], actuating devices [140], and sound scramblers [127, 128]. Only recently have nonlinear localized modes begun to be explored in granular crystals. Previous studies have focused on metastable breathers in acoustic vacuum [101], the observation of localized oscillations near a defect [118, 136], and one-dimensional (1D) diatomic crystals restricted to linear dynamics due to welded sphere contacts [109]. Understanding and controlling localization in granular crystals might lead to new energy harvesting/filtering devices.

In this chapter, we use experiments, theory, and numerical simulations to investigate the existence, stability, and dynamics of DBs in a compressed 1D diatomic granular crystal. The characteristics of the DB are a few number of particles oscillate with a frequency in the forbidden band (i.e., the gap) of the linear spectrum, with an amplitude which decreases exponentially from the central particle. We first detail our experimental setup and theoretical model. We then analyze the system's dynamics in the linear regime, show how a modulational instability (MI) generates DBs in the weakly nonlinear regime, and finally provide experimental evidence of their existence.

3.2 Experimental Setup

We assemble a 1D diatomic granular crystal by alternating aluminum spheres (6061-T6 type, radius $R_a = 9.525$ mm, mass $m_a = 9.75$ g, elastic modulus $E_a = 73.5$ GPa, Poisson ratio $\nu_a = 0.33$) and stainless steel spheres (316 type, $R_b = R_a$, $m_b = 28.84$ g, $E_b = 193$ GPa, $\nu_b = 0.3$). The reported values of $E_{a,b}$ and $\nu_{a,b}$ are standard specifica-

tions [3, 4]; we discuss the precise characterization of the effective elastic properties of our system below. We hold the spheres in place using four polycarbonate restraining bars and guide plates. At one end of the crystal, we apply a precompressive force using a lever-mass system. We drive the crystal dynamically with a piezoelectric actuator that we fit on a steel plate clamped on a steel bracket (called the “wall” in figure 3.1). We visualize the evolution of the force-time history of the propagating excitations using calibrated, periodically-placed piezo sensors that we embed inside selected particles (preserving the inertia and the bulk stiffness of the original bead [116, 127, 128]). We measure the static load using a calibrated strain gauge cell that we place in contact with the lever arm and with the last bead of the crystal.

3.3 Theoretical Model

We model a 1D diatomic crystal of N spheres as a chain of nonlinear oscillators [21]:

$$m_i \ddot{u}_i = A[\delta_0 + u_{i-1} - u_i]_+^p - A[\delta_0 + u_i - u_{i+1}]_+^p, \quad (3.1)$$

where $[Y]_+$ denotes the positive part of Y , u_i is the displacement of the i th sphere (where $i \in \{1, \dots, N\}$) around the static equilibrium, the masses are $m_{\text{odd}} = m_a$ and $m_{\text{even}} = m_b$, and the coefficient A depends on the exponent p and the geometry/material properties of adjacent beads. The exponent $p = 3/2$ yields the Hertz potential law between adjacent spheres [84].

In this case, $A = \left(\frac{3}{4} \frac{1-\nu_a^2}{E_a} + \frac{3}{4} \frac{1-\nu_b^2}{E_b}\right)^{-1} \left(\frac{1}{R_a} + \frac{1}{R_b}\right)^{-1/2}$, and one obtains a static overlap of $\delta_0 = (F_0/A)^{2/3}$ under a static load F_0 [21, 84]. We compute the linear dispersion relation of our system from the linearization of equation (3.1). For diatomic crystals, this curve contains two branches (*acoustic* and *optical*) [10]. At the edge of the first Brillouin zone—i.e., at $k = \frac{\pi}{2a}$, where $a = R_a + R_b - \delta_0$ is the equilibrium distance between two adjacent beads—the linear spectrum possesses a gap between the upper cutoff frequency $\omega_1 = \sqrt{2K_2/M}$ of the acoustic branch and the lower cutoff frequency $\omega_2 = \sqrt{2K_2/m}$ of the optical branch. The linear stiffness is $K_2 =$

$\frac{3}{2}A^{2/3}F_0^{1/3}$, and we define $M = \max\{m_a, m_b\}$ and $m = \min\{m_a, m_b\}$. The upper cutoff frequency of the optical band is located at $\omega_3 = \sqrt{2K_2(1/m + 1/M)}$. In Table 3.1, we summarize K_2 , A , and the three cutoff frequencies, which we estimate using standard specifications [3, 4] and compute using a static load of $F_0 = 20$ N.

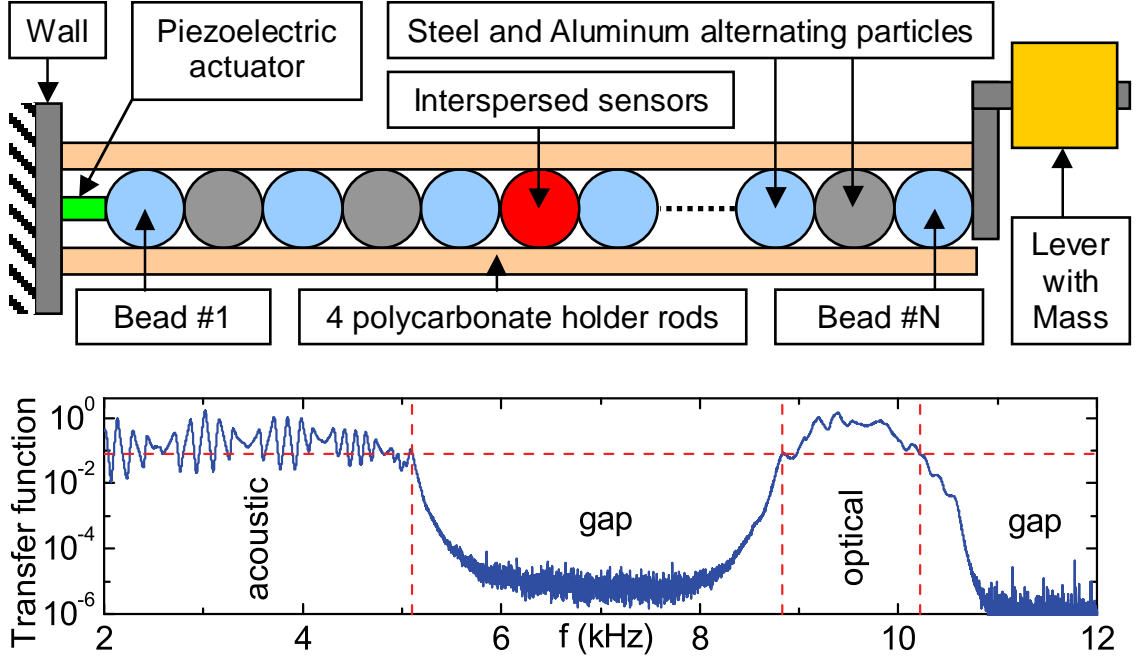


Figure 3.1: Top panel: Experimental setup. Bottom panel: Experimental phonon spectrum of the 81-bead steel-aluminum diatomic crystal. The horizontal line designates half of the low frequency mean value, and vertical lines indicate the f_n^{exp} cutoff frequencies given in Table 3.1.

3.4 Linear Spectrum

We experimentally characterize the linear spectrum of a diatomic crystal [151] ($N = 81$ and $F_0 = 20$ N) by applying low-amplitude (approximately 10 mN peak), broadband frequency (2 – 18 kHz), and uniform noise for 800 ms. We measure the dynamic force using a sensor located inside the 14th particle, and derive the input force from the driving voltage multiplied by the actuator sensitivity. We then compute the power spectral density (PSD) of the force-sensor, normalize it to the PSD of the driving force, and average the ratio over 8 acquisitions to obtain the transfer function shown

in figure 3.1. This spectrum clearly shows forbidden bands (i.e., gaps) and pass bands bounded by cutoff frequencies. These frequencies match half of the transfer function’s low-frequency level, which we compute as the mean level in the 2 – 4 kHz range. We summarize these frequencies in Table 3.1. Matching these frequencies to the theoretical formulas above provides an opportunity to probe the beads’ effective parameters K_2 and A shown in Table 3.1 (error bars indicate the standard deviations from the three frequency measurements). We find that all cutoff frequencies show a systematic upshift of about 9% compared to the predictions from standard specifications. We have identified four possible explanations: (i) the uncertainty in the standard values of material parameters [3, 4]; (ii) non-Hookean elastic dynamics might lead to a slight shift in the nonlinear exponent p and accordingly a large deviation in the coefficient A [84]; (iii) imperfect surface smoothness might induce fluctuations in p and hence in A [103]; and (iv) dissipative mechanisms, such as viscoelasticity and solid friction, can induce stiffening of the interaction potential between particles [116, 133].

	f_1 [kHz]	f_2 [kHz]	f_3 [kHz]	K_2 [N/ μm]	A [N/ $\mu\text{m}^{3/2}$]
th.	4.71	8.10	9.37	12.63	5.46
exp.	5.11	8.83	10.22	14.95 ± 0.10	7.04 ± 0.07
diff.	+8.5%	+9.0%	+9.1%	+18.4%	+28.8%

Table 3.1: Predicted (from standard specifications [3, 4]) versus measured cutoff frequencies, linear stiffness K_2 , and coefficient A under a static precompression of $F_0 = 20$ N.

3.5 Modulational Instability and DBs

We now consider the weakly nonlinear dynamics of the granular crystal. If the displacements have small amplitudes relative to those due to precompression, we can take a power series expansion of the forces (up to quartic displacement terms) to yield the $K_2 - K_3 - K_4$ model:

$$m_i \ddot{u}_i = \sum_{k=2}^4 K_k [(u_{i+1} - u_i)^{k-1} - (u_i - u_{i-1})^{k-1}] , \quad (3.2)$$

where $K_3 = -\frac{3}{8}A^{4/3}F_0^{-1/3}$ and $K_4 = \frac{3}{48}A^2F_0^{-1}$. equation (3.2) constitutes a diatomic variant of the Fermi-Pasta-Ulam (FPU) nonlinear oscillator chain [152–155]. Because $\frac{K_3^2}{K_2K_4} > \frac{3}{4}$, we expect the lower optical cutoff mode, for which the light masses oscillate out of phase at frequency f_2^{exp} and the heavy masses are at rest, to be subject to MI [142], which is a principal mechanism for energy localization in nonlinear lattices [156, 157]. In order to verify this prediction, we numerically solve equation (3.1) using A_{exp} (see Table 3.1) and the lower optical cutoff mode as the initial condition. To trigger the MI, we choose an initial oscillation amplitude of the light masses that corresponds to an 11.25 N (i.e., $0.5625F_0$) dynamic peak force. As shown in figure 3.2(a), this method allows us to observe the MI and the resulting generation of a localized mode, after $t \simeq 8$ ms, with frequency $f_b = 7.95$ kHz in the gap. In figure 3.2(a2), one can observe an exponential growth, which is characteristic of MI, around $t \simeq 5$ ms. A more convenient way to excite the lower optical cutoff mode is to drive the chain at one end with a sine wave at the lower optical cutoff frequency, $f_{\text{act}} = f_2^{\text{exp}}$. In figure 3.2(b1), we show an example of the spatiotemporal evolution of the forces when the chain is driven during 30 ms (the amplitude of the first bead’s displacement is about $0.061\delta_0$). In this example, the maximum dynamic force acting on the beads over the first 10 cycles of the excitation is about 6.5 N $\simeq 0.325F_0$. We thus anticipate a weakly nonlinear response that is well described by the $K_2 - K_3 - K_4$ theory. Indeed, during the first 20 ms, the lower optical cutoff mode is established, followed by an MI after $t \simeq 22$ ms. The width of the extended lattice wave is decreased, its amplitude is increased and—as a result of the spontaneous symmetry breaking induced by the instability—a DB is subsequently formed, which for these initial conditions, is localized near bead 37. This nonlinear solution exists even after the actuator is turned off at $t = 30$ ms. The PSD of the force at particle 36 [see figure 3.2(b2)] reveals the presence of a frequency component in the gap at $f_b \simeq 8.14$ kHz $< f_2^{\text{exp}}$. From numerical simulations, we find that the final location of the DB depends on the features of the driving signal (amplitude, frequency, and duration). Thus, the exact localized pinning site is not known a priori.

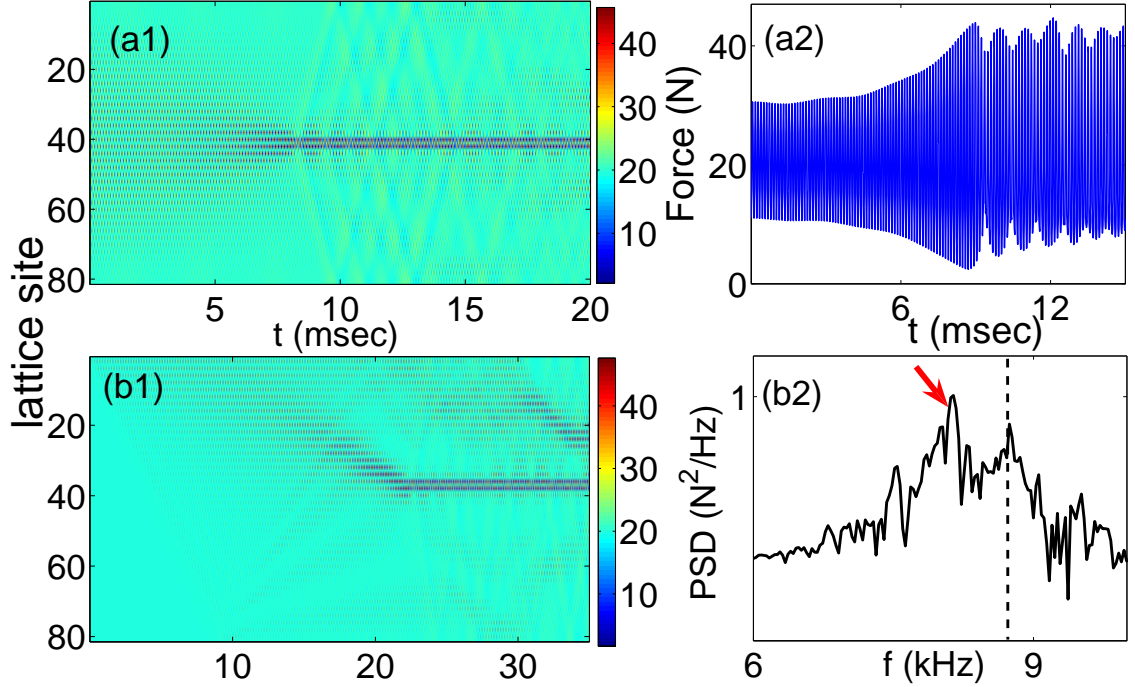


Figure 3.2: (a1) Spatiotemporal evolution of the forces for the simulated manifestation of the MI and DB generation with particle initial conditions corresponding to the lower optical cutoff mode. (a2) Force versus time for particle 40 for the simulation shown in (a1). (b1) Spatiotemporal evolution of the forces for the generation of a DB under conditions relevant to our experimental setup. (b2) PSD of particle 36 for the simulation shown in (b1). The dashed line in (b2) indicates the driving frequency $f_{\text{act}} = f_2^{\text{exp}}$, and the arrow indicates the DB frequency $f_b \simeq 8.14 \text{ kHz} < f_2^{\text{exp}}$.

3.6 Exact Solutions and Stability of DBs

We apply Newton’s method (see [51] and references therein) with free boundary conditions to numerically obtain, with high precision, the above dynamically generated DB waveforms as exact time-periodic solutions. We then study their linear stability and frequency dependence (within the spectral gap). Continuing this solution within the gap [i.e., for $f \in (f_1^{\text{exp}}, f_2^{\text{exp}})$] starting from the lower optical cutoff mode allows us to trace the entire family of DB solutions. In figure 3.3(a), we show the maximum dynamic force $\max(F_i)$, which is the experimentally observable parameter of the DB solution, as a function of the DB frequency f_b . As $f_b \rightarrow f_2^{\text{exp}}$, $\max(F_i) \rightarrow 0$ and the DBs broaden and finally merge with the linear lower optical cutoff mode. In the insets

of figure 3.3(a), we show examples of these solutions with frequencies $f_b = 8.35$ kHz and $f_b = 8.75$ kHz. To examine the stability of the DB solutions, we compute their Floquet multipliers λ_j [51]. If $|\lambda_j| = 1$ for all j , then the DB is linearly stable. In figure 3.3(b), we show the stability diagram for the family of DB solutions and the corresponding locations of Floquet multipliers in the complex plane for the DB with $f_b = 8.63$ kHz. Strictly speaking, the DB is stable only for $f_b \simeq f_2^{\text{exp}}$. Otherwise, the DB family exhibits oscillatory instabilities [51, 136]. However, the deviations of the unstable eigenvalues from the unit circle are bounded above by 0.08, and numerical integration of the DBs up to times $100T$ (where T is their period) reveals their robustness. Importantly, we also find that DB solutions exhibit a strong instability due to a pair of real multipliers when $f_b \in (8.45 \text{ kHz}, 8.7 \text{ kHz})$. As shown in figure 3.3(b), this instability is connected with the turning points of the energy of the DB as a function of its frequency (these occur when $dE/df_b = 0$). Similar features have also been observed in diatomic Klein-Gordon chains [158].

3.7 Experimental Observation of DBs

We excite the 81-bead diatomic crystal by driving the actuator with a higher-amplitude (relative to the linear-spectrum experiments) 90 ms sine voltage with frequency close to the lower optical cutoff frequency f_2^{exp} . We place force sensors in particles 2, 6, 10, 14, 18, 22, and 26. The experimental results in figure 3.4 show the MI onset and subsequent DB formation. figure 3.4(a) shows the force versus time at particles 2 (near the actuator) and 14 (close to the DB pinning site), and figure 3.4(b) shows the corresponding PSDs. The peak force amplitude near the actuator is $8.6 \text{ N} \simeq 0.43F_0$ (where $F_0 = 20 \text{ N}$). figure 3.4(c) shows the normalized power versus lattice site at both the driving and DB frequencies, before and after the formation of the DB. The normalized power is the PSD at a given frequency divided by the spectral power—i.e., the integral of the PSD over all frequencies. The force at particle 14 shows an exponential increase (at $t \simeq 20$ ms), which is indicative of the onset of MI. This is followed by the DB formation at $t \simeq 55$ ms. Both figure 3.4(b) and (c) show the

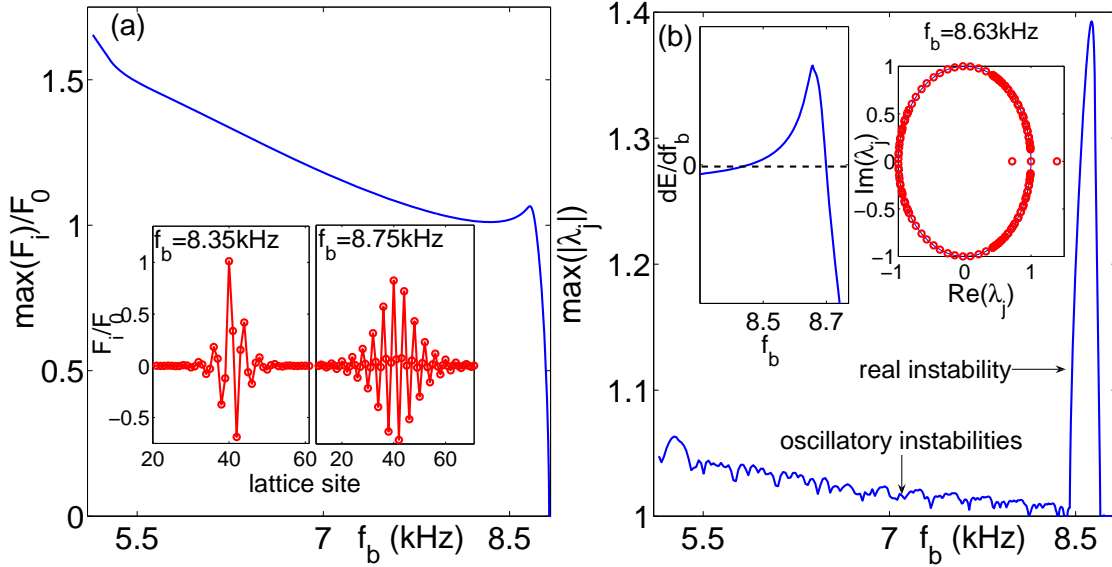


Figure 3.3: Bifurcation diagram of the continuation of the DB solutions. (a) Maximal dynamic force of the wave versus frequency f_b . The insets show spatial profiles at two values of f_b . (b) Maximal deviation of Floquet multipliers from the unit circle, which indicates the instability growth strength. The right inset shows a typical multiplier picture, and the left inset shows the connection between the strong (real multiplier) instability and the change in sign of dE/df_b .

appearance of a frequency component $f_b^{\text{exp}} \simeq 8.28$ kHz in the gap and localization of the energy over approximately 15 beads around site 14. Before the DB generation, for $t \leq 35$ ms, the lattice mostly vibrates at the driving frequency, and the power is uniformly distributed over the lattice [see figure 3.4(c1)]. After the DB formation, for $t \geq 55$ ms, part of the energy is pumped from the driving to the DB frequency, as shown in figure 3.4(c2). The decay of the vibrations after the actuator is turned off, which does not occur in the numerical simulations, arises from dissipation [116, 133]. However, analysis of the PSD after the actuator is turned off indicates that the power at DB frequency is longer-lived than at the driving frequency.

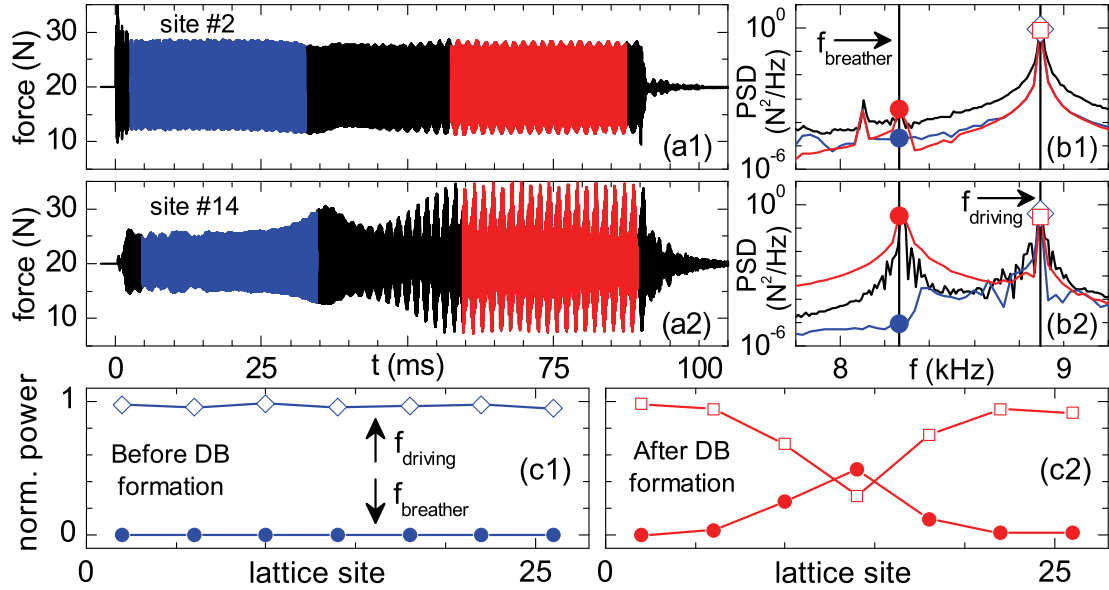


Figure 3.4: Experimental observations of MI and DB at $f_b^{\text{exp}} \simeq 8.28$ kHz, with $f_1^{\text{exp}} < f_b^{\text{exp}} < f_2^{\text{exp}}$, while driving the chain at 8.90 kHz $\simeq f_2^{\text{exp}}$ (see Table 3.1) for 90 ms. (a1, a2) Forces versus time and (b1, b2) PSDs at particles 2 and 14. Normalized power versus lattice site at the driving (open symbols) and the DB (filled symbols) frequencies, before (c1) and after (c2) DB formation. Vertical lines in (b) mark the driving frequency and the DB frequency. Blue (red) curves in (a, b, c) refer to time regions of 30 ms before (after) the DB formation, while the black curves refer to the entire signal.

3.8 Conclusions

We have characterized the dynamics of compressed 1D diatomic granular crystals using theory, numerical simulations, and experiments. We found good agreement for the linearized spectrum, explored the mechanism leading to the formation of DBs via MI, and provided clear experimental proof of their existence. Our results provide a first step toward achieving a deeper understanding and classifying ILMs in 1D granular crystals and pave the way for their manifestation in 2D and 3D lattices, which might eventually lead to their exploitation in energy-harvesting applications.

3.9 Author Contributions

This chapter is based on [5]. G.T., P.G.K., M.A.P., and C.D. proposed the study. N.B. and S.J. led the experimental work. G.T. led the theoretical and numerical analysis. C.D., P.G.K., and M.A.P provided guidance and contributed to the design and analysis throughout the project. All authors contributed to the writing and editing of the manuscript.

Chapter 4

Existence and Stability of Discrete Breather Families in Diatomic Granular Crystals

We present a systematic study of the existence and stability of discrete breathers that are spatially localized in the bulk of a one-dimensional chain of compressed elastic beads that interact via Hertzian contact. The chain is diatomic, consisting of a periodic arrangement of heavy and light spherical particles. We examine two families of discrete gap breathers: (1) an unstable discrete gap breather that is centered on a heavy particle and characterized by a symmetric spatial energy profile and (2) a potentially stable discrete gap breather that is centered on a light particle and is characterized by an asymmetric spatial energy profile. We investigate their existence, structure, and stability throughout the band gap of the linear spectrum and classify them into four regimes: a regime near the lower optical band edge of the linear spectrum, a moderately discrete regime, a strongly discrete regime that lies deep within the band gap of the linearized version of the system, and a regime near the upper acoustic band edge. We contrast discrete breathers in anharmonic FPU-type diatomic chains with those in diatomic granular crystals, which have a tensionless interaction potential between adjacent particles, and highlight in that the asymmetric nature of the latter interaction potential may

4.1 Introduction

The study of granular crystals draws on ideas from condensed matter physics, solid mechanics, and nonlinear dynamics. A granular crystal consists of a tightly packed, uniaxially compressed array of solid particles that deform elastically when in contact with each other. One-dimensional (1D) granular crystals have been of particular interest over the past two decades because of their experimental, computational, and (occasionally) theoretical tractability, and the ability to tune the dynamic response to encompass linear, weakly nonlinear, and strongly nonlinear behavior by changing the amount of static compression [21, 22, 52, 102, 116]. Such systems have been shown to be promising candidates for many engineering applications, including shock and energy absorbing layers [99, 100, 115, 138, 139], actuating devices [140], acoustic lenses [141] and sound scramblers [127, 128].

Intrinsic localized modes (ILMs), which are also known as discrete breathers (DBs), have been a central theme for numerous theoretical [19, 51, 53, 55–58, 159–162] and experimental studies [36, 59–65, 163–165] for more than two decades. Granular crystals provide an excellent setting to investigate such phenomena further. Recent papers have begun to do this, considering related topics, e.g., metastable breathers in acoustic vacuum [101], localized oscillations on a defect that can occur upon the incidence of a traveling wave [118], and an investigation of the existence and stability of localized breathing modes induced by the inclusion of “defect” beads within a host monoatomic granular chain [136]; for earlier work see, e.g., the reviews of [21, 52].

Very recently, we reported the experimental observation of DBs in the weakly nonlinear dynamical regime of 1D diatomic granular crystals [5]. In [5] we describe the characteristics of the DB to be a few number of particles oscillate with a frequency in the forbidden band (i.e., the gap) of the linear spectrum, with an amplitude which decreases exponentially from the central particle. We took advantage of a modulational instability in the system to generate these breathing modes, and found good qualitative and even quantitative agreement between experimental and numerical results. It is the aim of the present chapter to expand on these investigations with a more

detailed numerical investigation of the existence, stability and dynamics of DBs in a diatomic, strongly compressed granular chain. In this paper, we examine two families of DBs lying within the gap of the linear spectrum (or discrete gap breathers-DGBs). By varying their frequency, DGBs can subsequently be followed as a branch of solutions. The family that is centered around a central light mass and has an asymmetric energy profile can potentially be stable sufficiently close to the lower optical band edge before becoming weakly unstable when continued further into the gap. Other solutions, such as the family that is centered around a central heavy mass and has a symmetric energy profile seem to always be unstable. We examine both light and heavy mass centered families using direct numerical simulations.

The study of DGB has importance both for increasing understanding of the nonlinear dynamics of strongly compressed granular elastic chains, and for the potential to enable the design of novel engineering devices. For instance, in the past there have been several attempts to design mechanical systems to harvest or channel energy from ubiquitous random vibrations and noise of mechanical systems [166, 167]. However, a drawback of such attempts has been that the energy of ambient vibrations is distributed over a wide spectrum of frequencies. Our recent experimental observation of intrinsic (and nonlinear) localized modes in chains of particles [5] opens a new possible mechanism for locally trapping vibrational energy in desired sites and harvesting such long-lived and intense excitations directly (e.g., by utilizing piezo-materials [168]).

The remainder of this chapter is structured as follows: We first report the theoretical setup for our investigations and discuss the system's linear spectrum. We then give an overview of the families of the DGB solutions that we obtain and present a systematic study of their behavior, categorized into four regimes relating to the frequency and degree of localization of these solutions. Finally, we summarize our findings and suggest some interesting directions for future studies.

4.2 Theoretical Setup

4.2.1 Equations of Motion and Energetics

We consider a 1D chain of elastic solid particles, which are subject to a constant compression force F_0 that is applied to both free ends as shown in figure 4.1. The Hamiltonian of the system is given by

$$H = \sum_{i=1}^N \left[\frac{1}{2} m_i \left(\frac{du_i}{dt} \right)^2 + V(u_{i+1} - u_i) \right], \quad (4.1)$$

where m_i is the mass of the i th particle, $u_i = u_i(t)$ is its displacement from the equilibrium position in the initially compressed chain, and $V(u_{i+1} - u_i)$ is the interaction potential between particles i and $i + 1$.

We assume that stresses lie within the elastic threshold (in order to avoid plastic deformation of the particles) and that the particles have sufficiently small contact areas and velocities, so that we can make use of tensionless, Hertzian power-law interaction potentials. To ensure that the classical ground state, for which $u_i = \dot{u}_i = 0$, is a minimum of the energy H , we also enforce that the interaction potential satisfies the conditions $V(0) = V'(0) = 0$, $V''(0) > 0$. The interaction potential can thus be written in the following form [52, 91]:

$$V(\phi_i) = \frac{1}{n_i + 1} \alpha_{i,i+1} [\delta_{i,i+1} - \phi_i]_+^{n_i+1} - \alpha_{i,i+1} \delta_{i,i+1}^{n_i} \phi_i - \frac{1}{n_i + 1} \alpha_{i,i+1} \delta_{i,i+1}^{n_i+1}, \quad (4.2)$$

where $\delta_{i,i+1}$ is the initial distance (which results from the static compression force F_0) between the centers of adjacent particles. Additionally, $\phi_i = u_{i+1} - u_i$ denotes the relative displacement, and $\alpha_{i,i+1}$ and n_i are coefficients that depend on material properties and particle geometries. The bracket $[s]_+$ of equation (4.2) takes the value s if $s > 0$ and the value 0 if $s \leq 0$ (which signifies that adjacent particles are not in contact).

The energy E of the system can be written as the sum of the energy densities e_i

of each of the particles in the chain:

$$\begin{aligned} E &= \sum_{i=1}^N e_i, \\ e_i &= \frac{1}{2}m_i\dot{u}_i^2 + \frac{1}{2}[V(u_{i+1} - u_i) + V(u_i - u_{i-1})]. \end{aligned} \quad (4.3)$$

In this chapter, we focus on spherical particles. For this case, the Hertz law yields

$$\alpha_{i,i+1} = \frac{4E_i E_{i+1} \sqrt{\frac{R_i R_{i+1}}{R_i + R_{i+1}}}}{3E_{i+1}(1 - \nu_i^2) + 3E_i(1 - \nu_{i+1}^2)}, \quad n_i = \frac{3}{2}, \quad (4.4)$$

where the i th bead has elastic modulus E_i , Poisson ratio ν_i , and radius R_i . Hence, a 1D diatomic chain of N alternating spherical particles can be modeled by the following system of coupled nonlinear ordinary differential equations:

$$m_i \ddot{u}_i = A[\delta_0 + u_{i-1} - u_i]_+^{3/2} - A[\delta_0 + u_i - u_{i+1}]_+^{3/2}, \quad (4.5)$$

where $A = \alpha_{i,i+1} = \frac{4E_1 E_2 \left(\frac{R_1 R_2}{R_1 + R_2}\right)^{1/2}}{3(E_2(1 - \nu_1^2) + E_1(1 - \nu_2^2))}$, $\delta_0 = \delta_{i,i+1} = \left(\frac{F_0}{A}\right)^{2/3}$, and we recall that F_0 is the static compression force. The particle masses are $m_{2i-1} = m$ and $m_{2i} = M$ for $i \in \{1, \dots, N\}$. By convention, we will take M to be the larger of the two masses and m to be the smaller of the two masses. The equations of motion for the beads at the free ends are

$$m_1 \ddot{u}_1 = F_0 - A[\delta_0 - (u_2 - u_1)]_+^{3/2}, \quad (4.6)$$

$$m_N \ddot{u}_N = A[\delta_0 - (u_N - u_{N-1})]_+^{3/2} - F_0. \quad (4.7)$$

4.2.2 Weakly Nonlinear Diatomic Chain

If the dynamical displacements have small amplitudes relative to those due to the static compression ($|\phi_i| < \delta_0$), we can consider the weakly nonlinear dynamics of the granular crystal. It is the interplay of this weak nonlinearity with the discreteness of

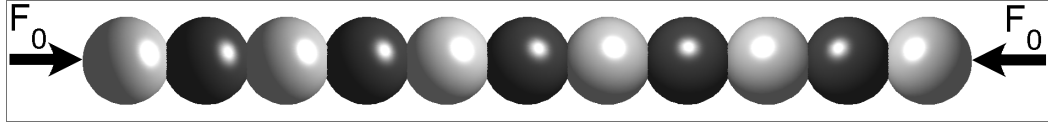


Figure 4.1: Schematic of the diatomic granular chain. Light gray represents aluminum beads, and dark gray represents stainless steel beads.

the system that allows the existence of the DGB. To describe this regime, we take a power series expansion of the forces (up to quartic displacement terms) to yield the, so-called, $K_2 - K_3 - K_4$ model:

$$m_i \ddot{u}_i = \sum_{j=2}^4 K_j [(u_{i+1} - u_i)^{j-1} - (u_i - u_{i-1})^{j-1}] , \quad (4.8)$$

where $K_2 = \frac{3}{2} A^{2/3} F_0^{1/3}$ is the linear stiffness, $K_3 = -\frac{3}{8} A^{4/3} F_0^{-1/3}$, and $K_4 = \frac{3}{48} A^2 F_0^{-1}$.

4.2.3 Linear Diatomic Chain

For dynamical displacements with amplitude much less than the static overlap ($|\phi_i| \ll \delta_0$), we can neglect the nonlinear K_3 and K_4 terms from equation (4.8) and compute the linear dispersion relation of the system [137]. The resulting diatomic chain of masses coupled by harmonic springs is a textbook model for vibrational normal modes in crystals [10]. Its dispersion relation contains two branches (called *acoustic* and *optical*). At the edge of the first Brillouin zone—i.e., at wave number $k = \frac{\pi}{2\Delta_0}$, where $\Delta_0 = R_a + R_b - \delta_0$ is the equilibrium distance between two adjacent beads—the linear spectrum possesses a gap between the upper cutoff frequency $\omega_1 = \sqrt{2K_2/M}$ of the acoustic branch and the lower cutoff frequency $\omega_2 = \sqrt{2K_2/m}$ of the optical branch. The upper cutoff frequency of the optical band is located at $\omega_3 = \sqrt{2K_2(1/m + 1/M)}$.

In addition to acoustic and optical modes, the diatomic semi-infinite harmonic chain also supports a gap mode, provided the existence of a light particle at the

surface and the use of free boundary conditions. This mode is localized at the surface (i.e., at the first particle) and its displacements have the following form [169]:

$$u_{2k+1} = B(-1)^k \left(\frac{m}{M}\right)^k e^{j\omega_s t}, \quad (4.9)$$

$$u_{2k+2} = B(-1)^{k+1} \left(\frac{m}{M}\right)^{k+1} e^{j\omega_s t}, \quad (4.10)$$

with $k \geq 0$, frequency $\omega_s = \sqrt{K_2(1/m + 1/M)}$ in the gap of the linear spectrum and B an arbitrary constant. Thus, the surface mode decays exponentially with a characteristic decay length of

$$\xi = 2\Delta_0 / \ln(M/m). \quad (4.11)$$

A standard derivation of the surface mode is given in Ref. [170], while a simple physical explanation of its existence and characteristics can be found in Ref. [171]. The latter is summarized as follows: Adjacent pairs vibrate in such a way that the connecting spring is not stretched. Thus each pair experiences no force from any other particle and is decoupled from the rest of the chain. The resulting decoupled pairs oscillate with ω_s .

This particular mode with frequency in the band gap, localized around the surface, proves to have a nonlinear counterpart and to be very closely related to the DGB in the strongly discrete regime as we describe in later sections.

4.2.4 Experimental Determination of Parameters

In our experiments from [5] and numerical simulations, we consider a 1D diatomic granular crystal with alternating aluminum spheres (6061-T6 type, radius $R_a = 9.53$ mm, mass $m = m_a = 9.75$ g, elastic modulus $E_a = 73.5$ GPa, Poisson ratio $\nu_a = 0.33$) and stainless steel spheres (316 type, $R_b = R_a$, $M = m_b = 28.84$ g, $E_b = 193$ GPa, $\nu_b = 0.3$). The values of $E_{a,b}$ and $\nu_{a,b}$ that we report are standard specifications [3, 4]. In Ref. [5], we experimentally characterized the linear spectrum of this diatomic crystal and we calculated the particle's effective parameter $A = 7.04$

$N/\mu\text{m}^{3/2}$. Using this value with the theoretical formulas above, we calculate the cutoff frequencies and the surface mode frequency. We summarize these results for a static load of $F_0 = 20$ N in Table 4.1. For the rest of the chapter we use this experimentally determined effective parameter A in our numerical analyses.

A [$\text{N}/\mu\text{m}^{3/2}$]	f_1 [kHz]	f_2 [kHz]	f_3 [kHz]	f_s [kHz]
7.04	5.125	8.815	10.20	7.21

Table 4.1: Calculated cutoff frequencies (based on the experimentally obtained coefficient A [5]) under a static compression of $F_0 = 20$ N.

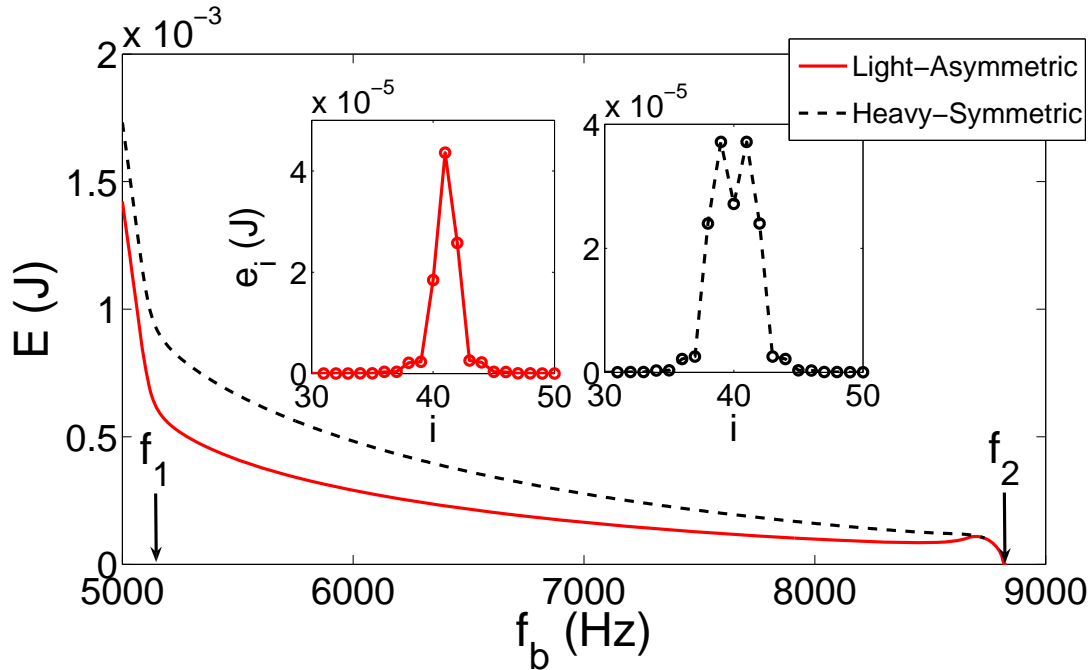


Figure 4.2: Energy of the two families of discrete gap breathers (DGBs) as a function of their frequency f_b . The inset shows a typical example of the energy density profile of each of the two modes at $f_b = 8000$ Hz.

4.3 Overview of DGB

4.3.1 Methodology

As the equations of motion (4.5) are similar to the equations of motion in the FPU-type problem of [172, 173], we accordingly recall relevant results. A rigorous proof of the existence of DBs in a diatomic FPU chain with alternating heavy and light masses (which is valid close to the $m/M \rightarrow 0$ limit) can be found in Ref. [153]. Information about the existence and stability of DBs in the gap between the acoustic and optical band of an anharmonic diatomic lattice can be found in Refs. [142, 152–155]. At least two types of DGBs are known to exist, and (as we discuss below) both can arise in granular chains.

We conduct numerical simulations of a granular chain that consists of $N = 81$ beads (except where otherwise stated) and free boundaries. In order to obtain DGB solutions with high precision, we solve the equations of motion (4.5, 4.6, 4.7) using Newton’s method in phase space. This method is convenient for obtaining DGB solutions with high precision and for studying their linear stability. Additionally, we can obtain complete families of solutions using parameter continuation; one chooses system parameters corresponding to a known solution and subsequently changes the parameters using small steps. For a detailed presentation of the numerical methods, see Ref. [51] and references therein.

4.3.2 Families of DGBs

The initial guess that we used to identify the DGB modes is the lower optical cutoff mode, obtained by studying the eigenvalue problem of the linearization of equation (4.5). Such a stationary profile (with vanishing momentum) is seeded in the nonlinear Newton solver to obtain the relevant breather-type periodic orbits. Continuation of this lower optical mode inside the gap allows us to follow one family of DGB solutions. By examining the energy density profiles of these solutions, we observe that they are characterized by an asymmetric localized distribution of the

energy centered at the central light bead of the chain (see the left inset of figure 4.2). We will henceforth refer to this family of solutions with the descriptor *LA* (light centered-asymmetric energy distribution).

For frequencies deep within the band gap, the DGB is not significantly affected by the boundary conditions since it extends only over few particles. Thus, its pinning site may be placed at any light bead of the chain, not only the central one. However, as the frequency of the DGB solution approaches the lower optical cutoff, the solution becomes more and more extended and the boundaries come into play. For instance, using an initial guess of a LA-DGB solution deep within the gap, shifted by a unit cell to the left, we performed a continuation throughout the frequency gap, and obtained a similar family of LA-DGB (but shifted by one unit cell). It is interesting to note that this family of breathers does not bifurcate from the optical band, as the family of the LA-DGB centered at the central light bead does, but rather ceases to exist at $f_b \approx 8755$ Hz.

These families of DGB solutions, centered at light beads, are not the only ones that our system supports. We were able to trace a second type of family as well. The energy density profiles for solutions in this second family are symmetric and centered on a heavy bead (see the right inset of figure 4.2). We will call this family of solutions *HS* (heavy centered-symmetric energy distribution). The seed for this solution (as will be described in further detail) may be obtained by perturbing the LA-DGB along an eigenvector associated with translational symmetry. A continuation of this family of solutions can be performed as well. Increasing the frequencies towards the optical cutoff band, we found that the HS-DGB family of solution, centered at the central heavy bead, also ceases to exist at $f_b \approx 8755$ Hz. This branch of DGBs is linearly unstable and at that frequency experiences a saddle-center bifurcation with the LA-DGB branch of solutions shifted one unit cell from the middle of the chain, and thus both families of DGBs disappear. The bifurcation point depends on the length of the system and specifically, the larger the system size, the closer the frequency of the bifurcation to the lower optical cutoff frequency.

The above phenomenology can be generalized for all the shifted families of DGB

solutions (namely LA and HS-DGB with different pinning sites). Approaching the optical band, consecutive pairs of HS-DGB and LA-DGB solutions collide and disappear. This cascade of pairwise saddle-center bifurcations occurs closer to the optical band edge, the further away from the chain boundary the pair of LA and HS-DGBs is centered. Only one branch of solution, the LA-DGB solution centered at the central light bead, survives and ends at the linear limit of the optical lower cutoff edge. In this chapter, we will focus on two families of DGB solutions. The LA-DGB centered at the central light bead and the HS-DGB centered at the central heavy bead.

In figure 4.2, we show the dependence of the breather's energy on its frequency and (in the insets) examples of the spatial energy profile of these two different families of DGB solutions (with frequency $f_b = 8000$ Hz) that the system supports. As one can observe in the energy diagram, the energies of the two solutions are very close around $f_b \approx 8755$ Hz, while the energy of the LA-DGB approaches zero as the frequency of the breather approaches the optical lower cutoff frequency f_2 . In contrast, when the frequency of the breather approaches the acoustic upper cutoff frequency f_1 , the energies of the solutions grow rapidly. As we discuss below, this arises from the resonance of the DGB with the linear acoustic upper cutoff mode.

Finally, as briefly discussed in Ref. [5], the energy of the LA-DGBs appears to have turning points (i.e., points at which $dE/df_b = 0$) at $f \approx 8480$ Hz and $f \approx 8700$ Hz. These turning points are directly associated with the real instability that the branch of LA-DGB solutions has in that frequency regime. This has also been observed in binary discrete nonlinear Schrödinger (DNLS) models with alternating on-site potential [174] and diatomic Klein-Gordon chains [158].

4.3.3 Stability Overview

In order to examine the linear stability of the obtained solutions, we compute their Floquet multipliers λ_j [51, 159]. If all of the multipliers λ_j have unit magnitude, then the DGB is linearly stable for our Hamiltonian dynamical model. Otherwise, it is subject to either real or oscillatory instabilities, for which the modulus of the

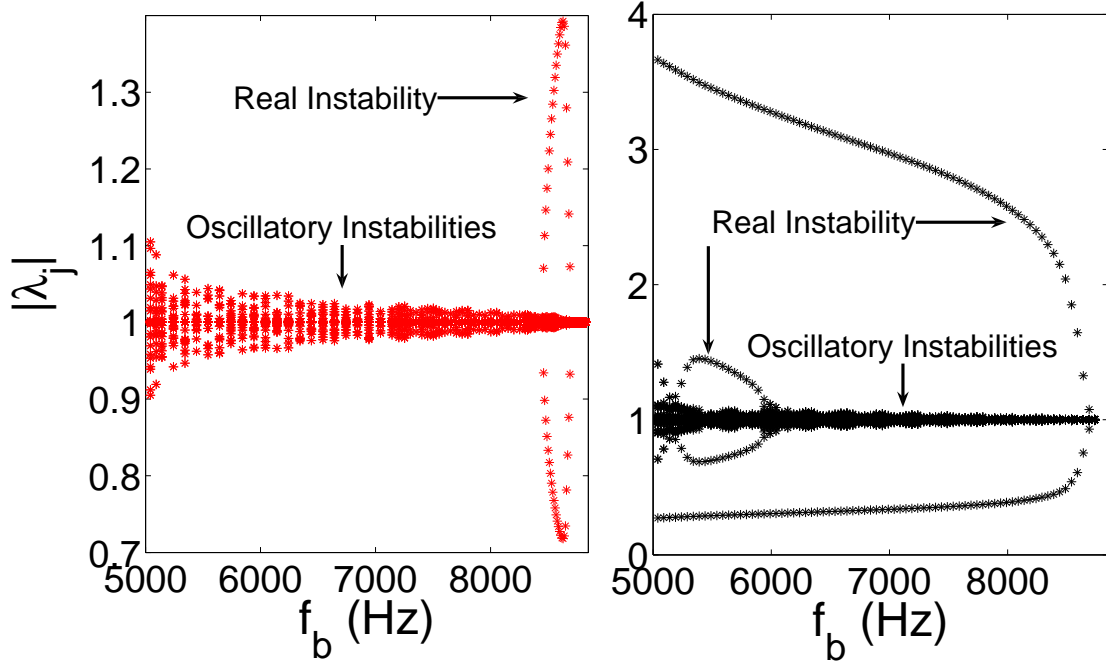


Figure 4.3: Magnitude of the Floquet multipliers as a function of DGB frequency f_b for the DGB with a light centered-asymmetric energy distribution (LA-DGB; left panel) and for the DGB with a heavy-centered symmetric energy distribution (HS-DGB; right panel).

corresponding unstable eigenvector grows exponentially as a function of time. It is important to note that two pairs of Floquet multipliers are always located at $(1, 0)$ in the complex plane. One pair, corresponding to the phase mode, describes a rotation of the breather's aggregate phase. The second pair arises from the conservation of the total mechanical momentum, an additional integral of motion that arises in FPU-like chains with free ends [51].

In figure 4.3, we show the resulting stability diagram for both families of DGB solutions. Strictly speaking, the DGBs are linearly stable only for f_b very close to f_2^{exp} . For all other frequencies, both families of the DGBs exhibit either real or oscillatory instabilities [159]. Real instabilities are connected to the collision of a pair of Floquet multipliers—the eigenvectors of which are spatially localized—at the points $(+1, 0)$ or $(-1, 0)$ on the unit circle. These instabilities are associated with growth rates that are typically independent of the size of the system (i.e., of the number

of particles in the chain). On the other hand, oscillatory instabilities can arise due to the collision of either two Floquet multipliers associated with spatially extended eigenvectors or one multiplier associated with a spatially extended eigenvector and another associated with a spatially localized one. Such collisions require that Krein signatures of the associated colliding eigenvectors are opposite [159]. From a physical perspective, the Krein signature is the sign of the Hamiltonian energy that is carried by the corresponding eigenvector [175]. Oscillatory instabilities can occur at any point on the unit circle.

The first type of oscillatory instability, which arises from the collision of two spatially extended eigenvectors, is known to be a finite-size effect. As discussed in Ref. [176], the strength of such instabilities should depend on the system size. In particular, when the size of the system is increased, the magnitude of such instabilities weakens uniformly. Simultaneously, the number of such instabilities increases with system size due to the increasing density of colliding eigenvalues. Eventually, these instabilities vanish in the limit of an infinitely large system.

The second type of oscillatory instability, which arises from a collision of a spatially localized eigenvector with a spatially extended eigenvector, occurs when an internal mode of the DGB (i.e., a localized eigenvector) enters the band of extended states associated with the phonon spectrum of the system (such extended eigenvectors are only slightly modified due to the presence of the DGB). This kind of oscillatory instability does not vanish in the limit of an infinitely large system and is directly connected with Fano-like resonant wave scattering by DGBs (see, e.g., Ref. [177] for the monoatomic FPU case).

4.4 Four Regimes of DGB: Existence and Stability

4.4.1 Overview of Four Dynamical Regimes

The purpose of this section is to qualitatively categorize the two families of DGB into four regimes (*(I) close to the optical band*, *(II) moderately discrete*, *(III) strongly*

discrete, and (IV) close to and slightly inside the acoustic band) according to DGB characteristics such as the maximum relative displacement and the localization length of the DGB, denoted by l (DGBs are localized vibrational modes with amplitude which decays exponentially as $\exp(-|i|/l)$). Recalling that ξ is the localization length of the linear surface mode, we find that this length, ξ , consists of a lower bound for the localization length l of both families of DGBs.

In the top panels of figure 4.4, we show typical examples of the relative displacement profiles of LA-DGB solutions (each of which occurs in a different regime of the band gap). We similarly show four typical HS-DGB solutions (at the same frequencies) in the bottom panels. In Table 4.2, we summarize the characteristics of the DGB solutions in the four regimes.

	Regime (I)	Regime (II)	Regime (III)	Regime (IV)
$\max \frac{ u_i - u_{i+1} }{\delta_0}$	< 1	$\gtrsim 1$	$\gg 1$	$\gg 1$
localization length	$l \gg \xi$	$l > \xi$	$l \gtrsim \xi$	$l \gg \xi$

Table 4.2: Characteristics of the DGBs in the four different regimes.

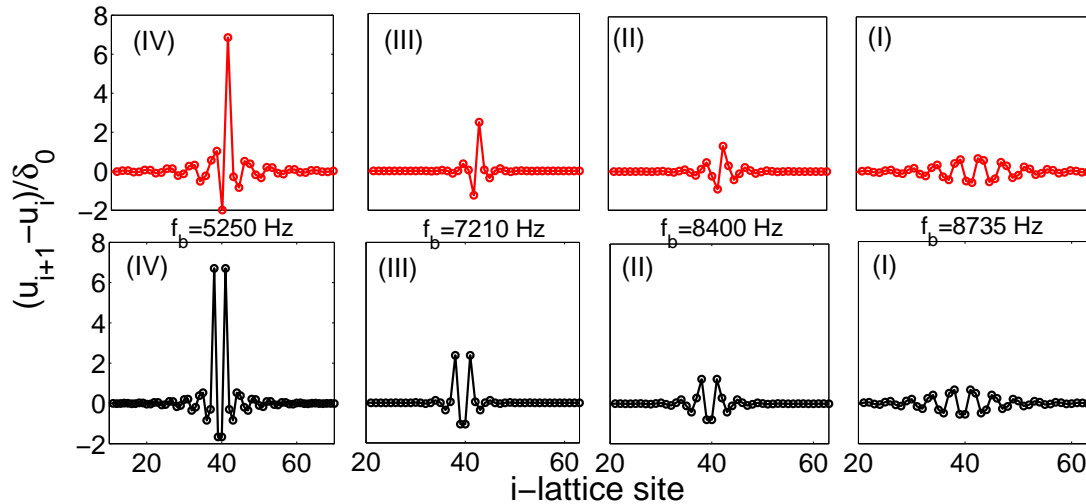


Figure 4.4: Top panels: Four typical examples of the relative displacement profile of LA-DGB solutions, each one from a different dynamical regime. Bottom panels: As with the top panels, but for HS-DGB solutions.

In addition to the differences in amplitude and localization length, each regime

displays some uniquely interesting characteristics. The *close to the optical* regime contains the only strictly linearly stable modes (LA-DGB). The *moderately discrete* regime includes (but is larger than) the aforementioned region of strong instability for the LA-DGB, and is the region within which our experimentally observed LA-DGB [5] falls. The *strongly discrete* regime shows a change in spatial displacement profile (in both families) with respect to the other regimes, which (as will be discussed) is connected to large time loss of contact between adjacent beads (gap openings) and the existence of gap surface modes, and is unique to our tensionless contact potential. The *close to and slightly inside the acoustic band* regime shows resonances with the upper acoustic band edge, and (for the HS-DGB) a resulting period doubling bifurcation.

We now continue, by conducting a detailed investigation of both DGB families in the four different regimes.

4.4.2 Region (I): Close to the Optical Band ($f_b \lesssim f_2$)

Regime (I) is located very close to the lower optical band edge of the linear spectrum. As we mention above, the HS-DGB family of solutions starts to exist from $f_b \approx 8755$ Hz and below, while the LA-DGB family of solutions is initialized from the linear limit at the lower edge of the optical band. In this regime, both DGB solutions are characterized by a localization length l that is much larger than the characteristic localization length ξ of the surface mode. The DGB spatial profiles have the form of the spatial profile of the optical cutoff mode and the LA-DGB family is linearly stable. Moreover, as indicated by the relative displacements of the solutions in regime (I), we can also conclude that $\max \frac{|u_i - u_{i+1}|}{\delta_0} < 1$, so the dynamics of the system is weakly nonlinear and the adjacent particles are always in contact (gaps do not open between particles). It should be noted that despite the linear stability, this similarity in frequency and spatial profile to the lower optical cutoff mode could make this regime of DGB difficult to observe experimentally and differentiate from the linear mode.

In this regime, since both DGB solutions are characterized by a small amplitude and a large localization length l , the effect of the discreteness is expected to be weak.

Continuous approximation techniques (see, for example, Ref. [142]) have revealed that the dynamics of the envelope of the solutions close to the optical band is described by a focusing nonlinear Schrödinger (NLS) equation. Hence, the two types of DGBs can be viewed as discrete analogs of the asymmetric gap solitons that are supported by the NLS equation that is obtained in the asymptotic limit.

In this regime, due to the weak effect of the discreteness for $f_b \lesssim f_2$, a third pair of Floquet multipliers appears in the vicinity of the point $(+1, 0)$ on the unit circle. This is in addition to the two previously discussed pairs of Floquet multipliers relating to the phase mode and conservation of momentum. This third mode is the mode associated with the *breaking* of the continuous translational symmetry (i.e., there is a discrete translational symmetry/invariance in the limit of small lattice spacing). The associated Floquet multiplier is of particular interest, as it has been associated with a localized mode called a “translational” or “pinning” mode [159]. Perturbing the LA-DGB solution along this corresponding Floquet eigenvector enables us to obtain the HS-DGB family of solutions (essentially translating light mass centered DGB by one site to a heavy centered DGB).

4.4.3 Region (II): Moderately Discrete Regime

We call regime (II) *moderately discrete*. In this regime, the localization length l of the two DGB solutions is smaller than in the case of regime (I), so the effect of discreteness becomes stronger. In regime (II), we find that $\frac{|u_i - u_{i+1}|}{\delta_0} \gtrsim 1$ near the central bead. As a result this regime also has a larger kink-shaped distortion of the chain (i.e., displacement differential between the left and right ends of the chain). This kink shaped distortion, which is visible in panel (a) of figure 4.5, is a static mutual displacement of the parts of the chain separated by the DGB, and is a characteristic of DB solutions in anharmonic lattices that are described by asymmetric interparticle potentials (see for example [142, 152]). The larger amplitude also translates into a gap opening for the contact(s) of the central particle for a small amount of time. The response of the system can be considered as strongly nonlinear near the central bead

of the breather and weakly nonlinear elsewhere.

As the frequency is decreased throughout this regime, the effect of the discreteness becomes stronger and the previously discussed “pinning” mode moves away from the point $(+1, 0)$ on the unit circle; it moves along the unit circle for the LA-DGB solution and along the real axis for the HS-DGB solution (which causes a strong real instability in the latter case). For $8450 \text{ Hz} < f_b < 8700 \text{ Hz}$ both DGB families are subject to strong harmonic (and real) instability. However for $f_b < 8400 \text{ Hz}$, the LA-DGB is subject only to weak oscillatory instabilities whereas the HS-DGB maintains the real instability. It is in this regime, below the strong instability frequency region that we categorize the type of LA-DGB found experimentally in [5].

We discuss both HS and LA-DGB modes of this regime in further detail in the following sections.

4.4.3.1 HS Discrete Gap Breather (HS-DGB)

In figure 4.5(a), we show the spatial profile of an example HS-DGB solution with frequency $f_b = 8600 \text{ Hz}$ located in the *moderately discrete* regime. Observe in the stability diagram in panel (b) that one pair of Floquet multipliers has abandoned the unit circle and is positioned along the real axis. This strong instability (with a real multiplier) is caused by a localized Floquet eigenvector (the pinning mode). We plot the displacement and velocity components of this eigenvector in panels (c) and (d), respectively. This localized pinning mode is symmetric and centered at a heavy particle. Perturbing the HS-DGB along this unstable eigenvector deforms it in the direction of the LA-DGB.

To reveal the effect of this instability (pinning mode) and elucidate the transition between HS and LA-DGB, we perform numerical integration of the original nonlinear equations of motion (4.5) using as an initial condition the sum of the unstable HS-DGB mode and the pinning mode. In order to reduce the reflecting radiation from the boundaries, we use a (rather large) chain that consists of $N = 501$ particles. The HS-DGB performs a few localized oscillations up to times of about $5T$ (where T is the period of the solution); then, it starts to emit phonon waves and eventually is

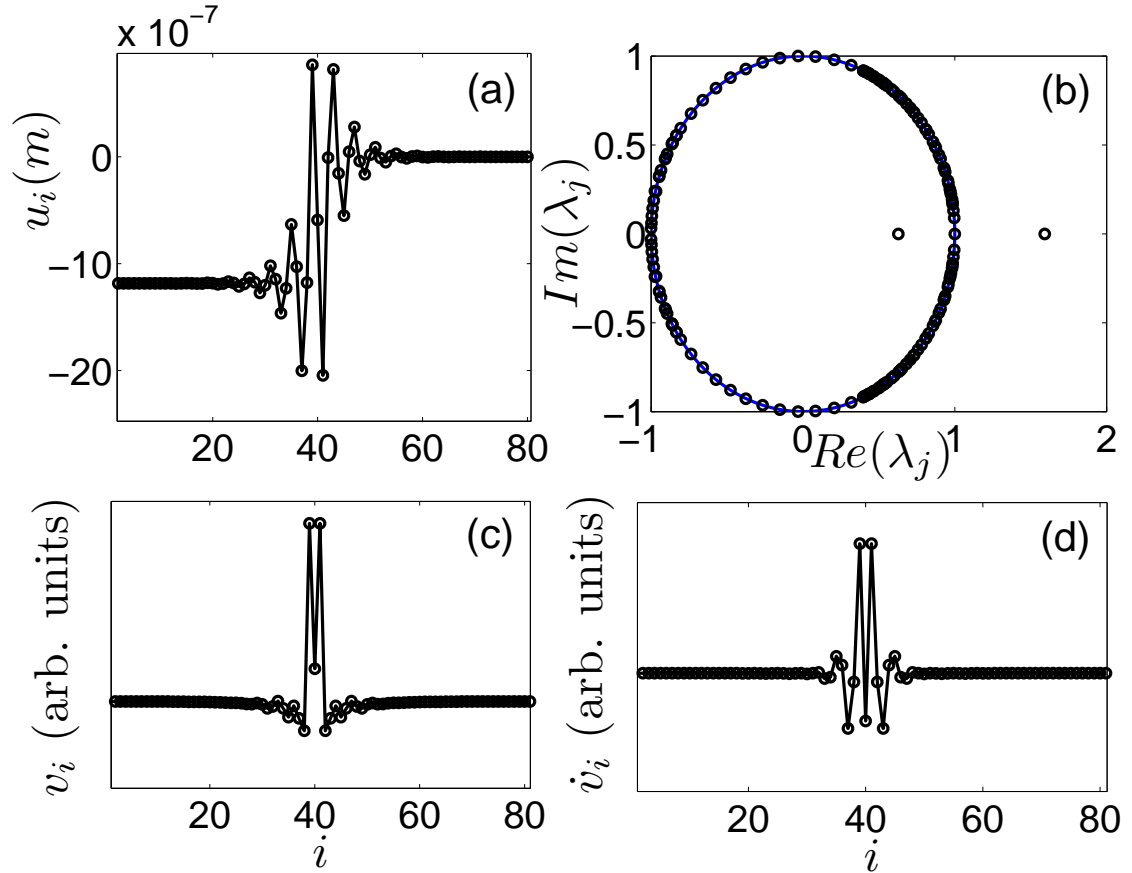


Figure 4.5: (a) Spatial profile of an HS-DGB with frequency $f_b = 8600$ Hz. (b) Corresponding locations of Floquet multipliers λ_j in the complex plane. We show the unit circle to guide the eye. Displacement (c) and velocity components (d) of the Floquet eigenvectors associated with the real instability.

transformed into a LA-DGB. By performing a Fourier transform of the displacements of the center particle (see the inset of figure 4.6), we find that the frequency of the transformed LA-DGB is $f_b \approx 7900$ Hz.

4.4.3.2 LA Discrete Gap Breather (LA-DGB)

We now discuss the LA-DGB branch of solutions in the *moderately discrete* regime. Carefully monitoring the motion of the Floquet multipliers on the unit circle during parameter continuation, we observe that at $f \approx 8717$ Hz, a pair of Floquet multipliers leaves the phonon band that consists of the eigenstates that are spatially extended. The corresponding eigenmode becomes progressively more localized as the frequency

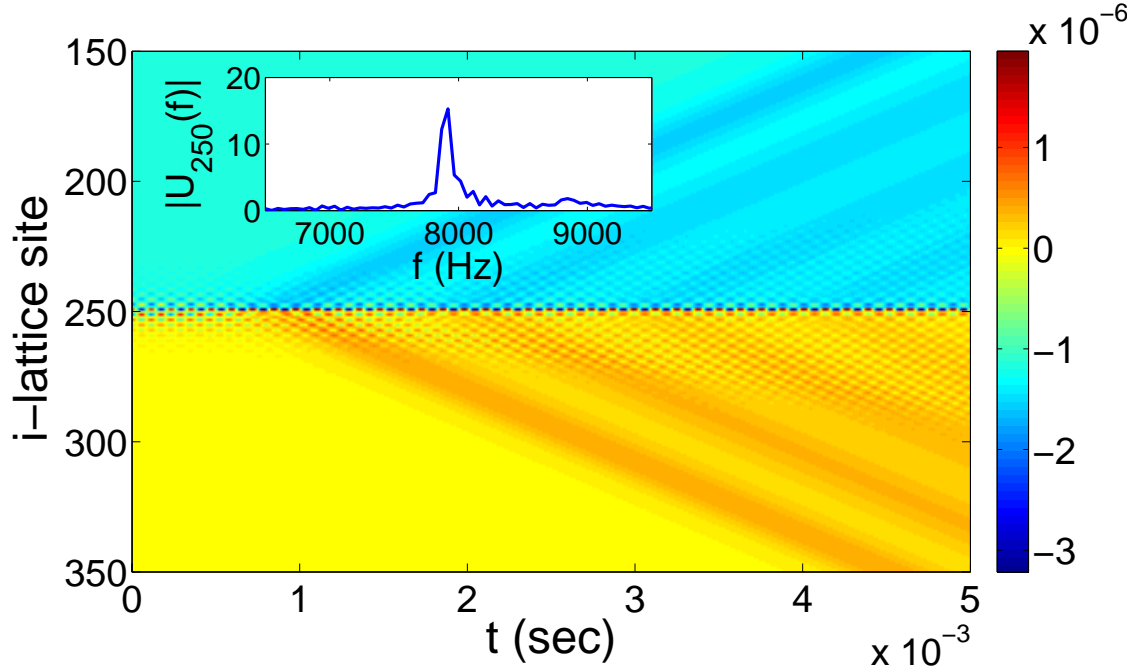


Figure 4.6: Spatiotemporal evolution (and transformation into $f_b \approx 7900$ Hz LA-DGB) of the displacements of a HS-DGB summed with the pinning mode and initial $f_b = 8600$ Hz. Inset: Fourier transform of the center particle.

decreases [178]. At $f \approx 8700$ Hz, it arrives at the point $(+1, 0)$ on the unit circle, where it collides with its complex conjugate to yield a real instability (see the left panel of figure 4.3). This instability persists down to $f \approx 8450$ Hz. As indicated above, this real instability is directly associated with the turning points that arise from the frequency dependence of the energy.

In figure 4.7(a), we show the spatial profile of an example LA-DGB solution with frequency $f_b = 8600$ Hz (in the real instability region). Observe in the stability diagram in panel (b) that one pair of Floquet multipliers has abandoned the unit circle and is located along the real axis. This strong instability (arising from the real multiplier) is caused by a localized Floquet eigenvector. We plot its displacement and velocity components in panel (c) and (d), respectively. This mode is asymmetric and centered at a light particle.

To reveal the effect of this instability, we perform numerical integration of the nonlinear equations of motion (4.5). As before, we use a large chain consisting of

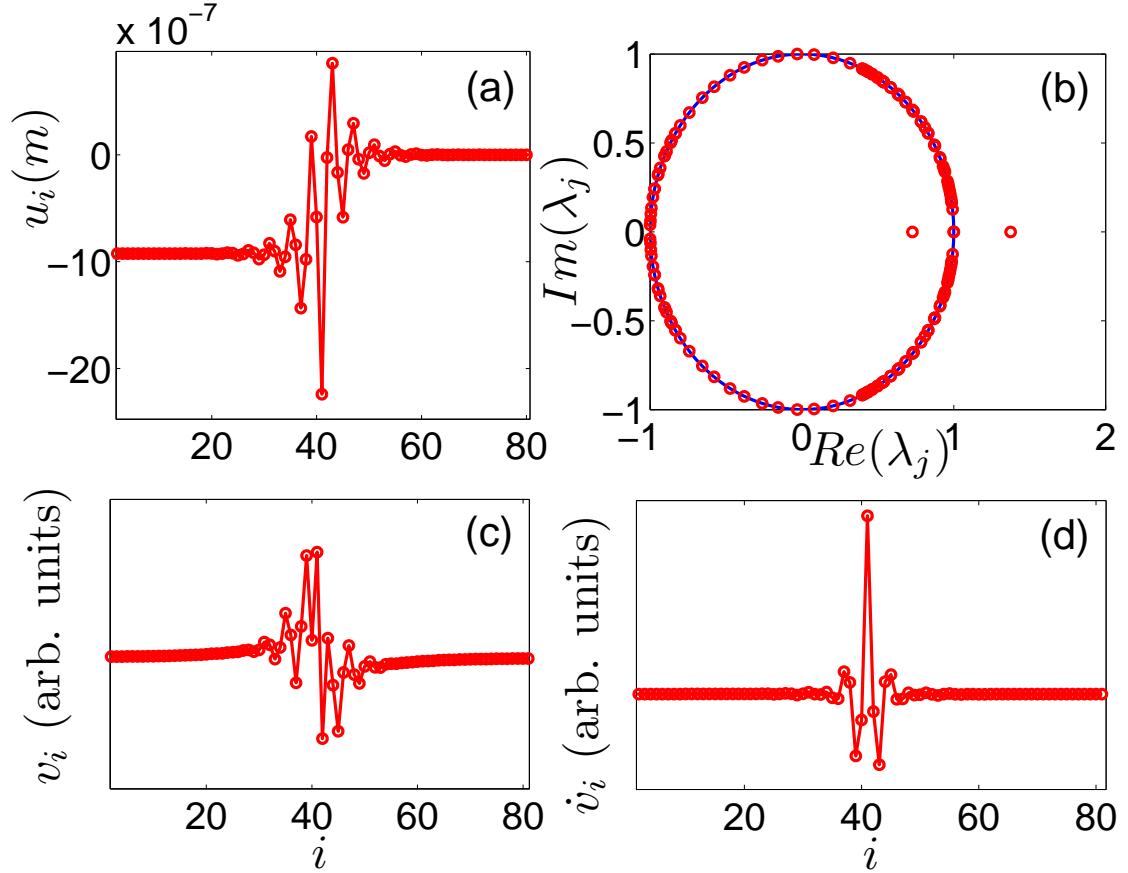


Figure 4.7: (a) Spatial profile of an LA-DGB with frequency $f_b = 8600\text{Hz}$. (b) Corresponding locations of Floquet multipliers λ_j in the complex plane. We show the unit circle to guide the eye. Displacement (c) and velocity (d) components of the Floquet eigenvector associated with the real instability.

$N = 501$ particles in order to reduce the reflecting radiation from the boundaries. As one can observe in the top panels of figure 4.8, the LA-DGB with frequency $f_b = 8600$ Hz, which is subject to the strong real instability, is transformed into a linearly stable, more extended, LA-DGB with $f_b \approx 8800$ Hz when we add to the solution the unstable Floquet eigenvector. On the other hand, as depicted in the bottom panels of figure 4.8, we obtain an LA-DGB with $f_b \approx 8200$ Hz when we subtract the unstable eigenvector from the initial LA-DGB solution. Hence, it becomes apparent that depending on the nature of the perturbation, the unstable LA-DGB can be “steered” towards higher or lower (more stable) oscillation frequencies within the gap.

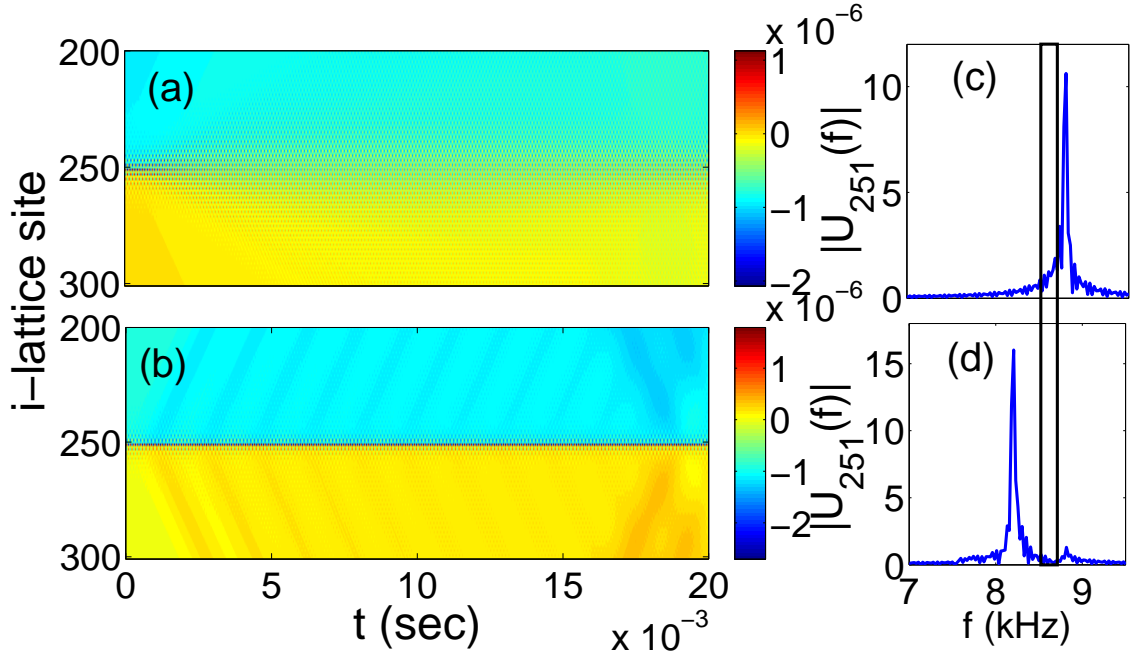


Figure 4.8: Spatiotemporal evolution of the displacements of a LA-DGB with $f_b = 8600$ Hz when one (a) adds and (b) subtracts the unstable localized mode depicted in figure 4.7(c). Panel (c) shows the Fourier transform of the center particle for case (a), and panel (d) shows the same for case (b). In panels (c,d), the two vertical lines enclose the regime of the frequencies in which the LA-DGB exhibits the strong real instability.

This is also important with respect to the experimental observation in [5]. As we have previously discussed, the DGB in the *nearly continuum* regime are very similar to the linear lower optical cutoff mode, and thus potentially difficult to detect. Following that regime, to this *moderately discrete* regime, both LA and HS-DGB are characterized by strong instabilities down to $f_b \approx 8400$ Hz. The HS-DGB continue to be characterized by a strong instability. As we showed in figure 4.6 the HS-DGB will transform to a LA-DGB below this region of strong instability. Furthermore, as we showed in figure 4.8 a LA-DGB in the strong instability region can transform to a LA-DGB of frequency either above or below the region of strong instability. It is natural then, as a more stable solution that is of significantly distinct profile, that the DGB observed in [5] is a LA-DGB in the *moderately discrete* regime with $f_b \approx 8280$ Hz. Although other effects such as dissipation will also play a role into the observability

of the DGB modes, the stability and structural analysis can be the beginnings of a guide for observability in practice.

4.4.4 Region (III): Strongly Discrete Regime ($f_1 \ll f_b \ll f_2$)

In regime (III), which we call *strongly discrete*, the localization length l of the DGB solutions is the smallest possible over the whole gap (i.e. is of the same order as ξ) and $\max \frac{|u_i - u_{i+1}|}{\delta_0} \gg 1$. The LA-DGB is subject only to weak oscillatory instabilities while the HS-DGB continues to be subject to the real instability, which has been considerably strengthened.

The spatial profile of the DGB solutions is now quite different from those in regimes (I) and (II) and hence from those of DGBs in a standard diatomic FPU-like system [154]. In figure 4.9, we show examples of both families of DGBs at $f_b = 7210$ Hz, the characteristic frequency of the linear surface mode (see Table 4.1), at $t = 0$ and $t = T/2$.

Comparing these solutions to their siblings in regimes (I) and (II) (for example, comparing figure 9a to figure 5a and figure 9c to figure 7a) reveals a remarkable change in their spatial profiles. We observe, in addition to their more narrow profile, that for both families of DGB at this particular frequency, near the center of the DGB there exist adjacent pairs with small relative displacements (they move together). This qualitative shape is now reminiscent of the linear surface modes in equations (4.9, 4.10) instead of the spatial profiles characterizing the DGB in the other regimes.

A possible explanation for the change of the spatial profiles of the DGBs is the following. Near the center of the strongly discrete DGBs, we find that

$$\frac{|u_{i-1} - u_i|}{\delta_0} \gg 1. \quad (4.12)$$

From a physical perspective, this means that there is a large amount of time (in contrast to what we observe in the moderately discrete regime) during which some beads near the center of the DGB lose contact with each other due to the tensionless Hertzian potential. The system thus experiences effectively free boundaries conditions

in the bulk as new “surfaces” are temporarily generated near the center of the DGB. However, as we have already mentioned for this type of system, a surface mode with a frequency in the gap (and now near this regime of DGB) exists only for free boundary conditions with light mass (aluminum) end particles. We observe, that for certain portions of the period of both HS and LA-DGB families, these conditions supporting a gap surface mode are satisfied. For this reason, in figure 4.9(b,c,d), we plot the spatial profile of the surface mode using equations (4.9, 4.10) and a corresponding visualization of our system which shows the location of gap openings and the newly created boundaries. For portions of the chain which have a light mass particle at the newly generated surface we overlay the displacement profile of the linear gap surface mode, with amplitude B of equations (4.9,4.10) fitted to match the displacement of the DGB solution.

At the particular frequency where the linear surface mode exists (see figure 4.9, equations (4.9, 4.10) and associated discussion), we can observe the following phenomenology. As gap openings arise, there is a very good agreement between the surface mode displacement profile and the corresponding portion of DGB solution. On the other side of the chain (by necessity terminating in a heavy particle), the waveform cannot form such a surface gap mode. Importantly, the reader should be cautioned that this is a dynamical process during the oscillation period of the “composite” (of the above chain parts) breather where the gap openings arise and disappear during different fractions of the breather period. Furthermore, it should be indicated that if the frequency deviates from the frequency of a linear surface gap mode, this phenomenology persists with the sole modification being that instead of the linear surface gap mode, during gap openings, we observe a nonlinear variant thereof with a progressively modified spatial profile.

Computation of the Floquet spectrum associated with linear stability shows that the HS-DGB modes in this regime continue to be subject to the strong real instability. Additionally, the HS-DGB and the LA-DGB modes each possess 7 quadruplets of eigenvalues that have left the unit circle. The maximum magnitude of these unstable Floquet multipliers is only about 1.02, so the corresponding instabilities are very

weak. In order to address the question of how such instabilities manifest, we perform long-time simulations using as an initial condition the numerically exact LA-DGB with frequency $f_b = 7000\text{Hz}$, which we perturb with white noise whose amplitude is 10% of that of the LA-DGB. The final result is the destruction of the DGB at $t \approx 0.075$ seconds soon following the generation of new internal frequencies and corresponding increase in the background noise. Thus, the corresponding LA-DGB has a finite lifetime of about $525T$, where $T = 1/f_b$ is the period of the breather. This long-time evolution is reminiscent of that observed when DNLS single-site breathers are destroyed by standing-wave instabilities [179].

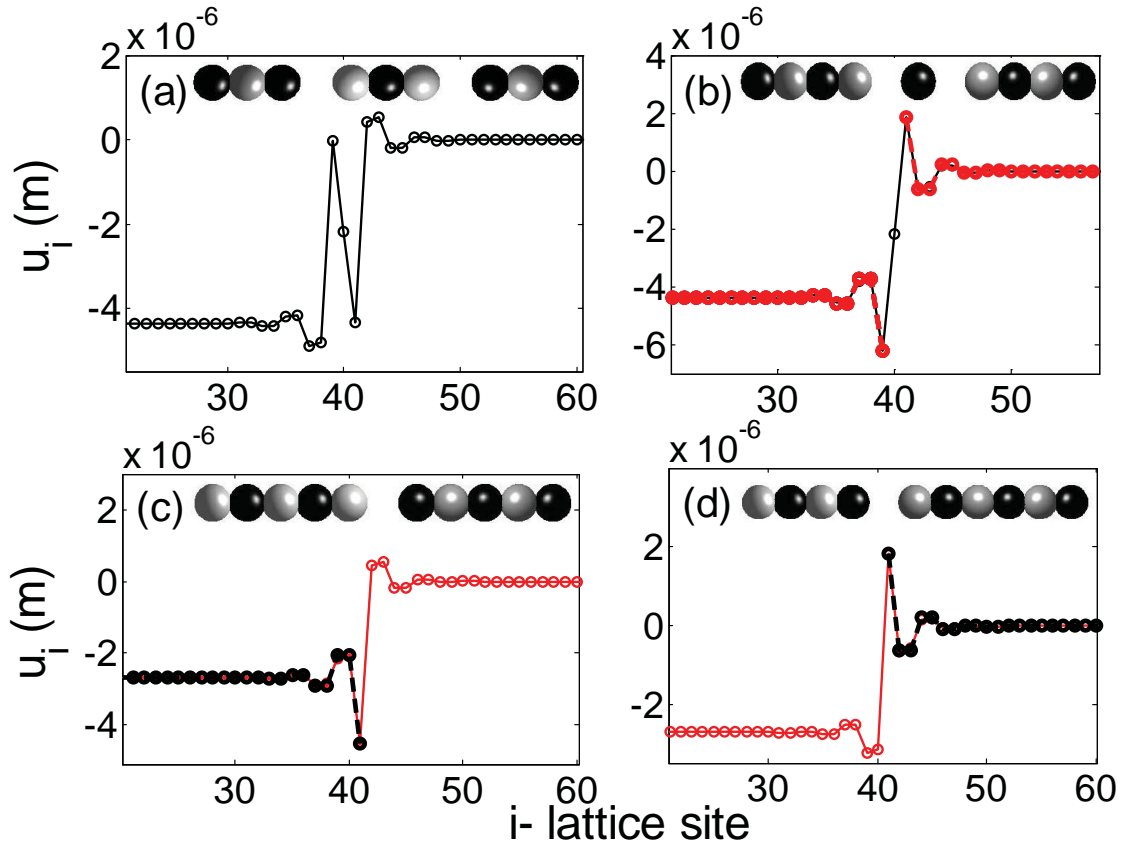


Figure 4.9: Top panels: Spatial profile of an HS-DGB with frequency $f_b = 7210$ Hz at $t = 0$ (a) and at $t = T/2$ (b). Bottom panels: As with the top panels, but for LA-DGB solutions. The dashed curves correspond to the spatial profile of the surface mode obtained using equations (4.9,4.10). In each panel, we include a visualization of particle positions, and gap openings, for the corresponding time and DGB solution.

4.4.5 Region (IV): Close to and Slightly Inside the Acoustic Band

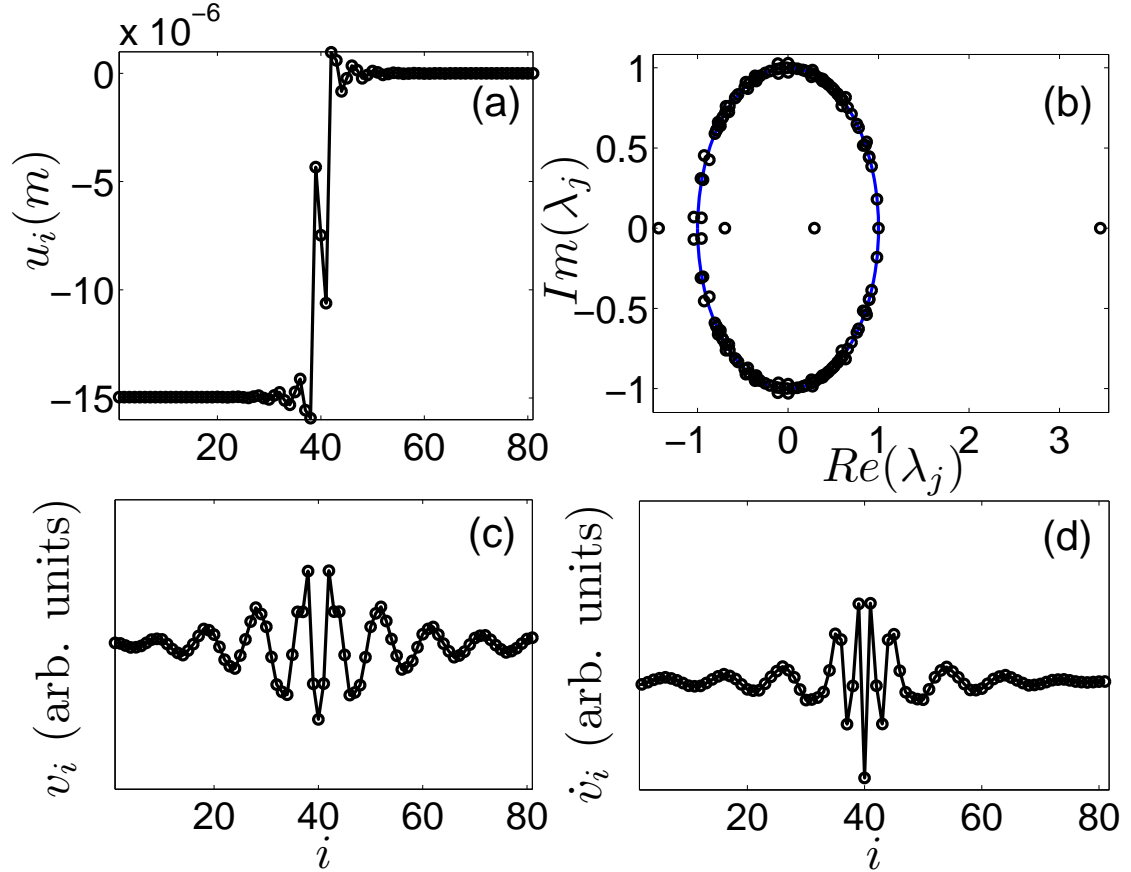


Figure 4.10: (a) Spatial profile of an HS-DGB with frequency $f_b = 5500$ Hz. (b) Corresponding locations of Floquet multipliers λ_j in the complex plane. We show the unit circle to guide the eye. (c) Displacement and (d) velocity components of the Floquet eigenvectors associated with the second real instability (which, as described in the text, is a subharmonic instability).

Finally, in regime (IV), which is close to and slightly inside the acoustic band, both DGB solutions are delocalized (which implies that $l \gg \xi$) due to resonance with the upper acoustic mode while the amplitude $\max \frac{|u_i - u_{i+1}|}{\delta_0} \gg 1$. In this regime, both solutions are subject to strong oscillatory instabilities, and the HS-DGB solutions are still subject to strong real instabilities. However, there is also an interval—specifically from $f_b \approx 5940$ Hz to $f_b \approx f_1$ —in which the HS-DGB family of breathers is subject

to a second real instability. This, so-called, subharmonic instability is caused by the collision of a quadruplet of unstable Floquet multipliers at the $(-1, 0)$ point on the unit circle. One pair of unstable Floquet multipliers returns to the unit circle but the second remains on the real axis. We show the displacement and velocity components of the associated unstable Floquet eigenvector at $f_b = 5500\text{Hz}$ in the bottom panels of figure 4.10. As one can see, the displacement and velocity components of the Floquet eigenvectors are extended. Perturbing the solution along this subharmonic instability eigendirection and focusing only on short term dynamics to avoid the manifestation of the stronger real instability, we observe a period doubling bifurcation (oscillations of the central bead with twice the period of that of the oscillations of the adjacent beads).

Finally, we examine what happens at and slightly inside the acoustic band. In contrast to the optical gap boundary, at which the DGB solutions delocalize and then vanish, we find in the acoustic boundary of the gap that the solutions delocalize, but persist with the addition of non-zero oscillating tails (see top panels of figure 4.11). These arise from resonance of the DGBs with the upper acoustic cutoff mode. The new bifurcated solutions are called *discrete out-gap breathers* (DOGBs). More about DOGBs and their possible bifurcations in a binary DNLS model can be found in Ref. [174]. In figure 4.11, we show the profiles of both families of DOGBs. In both cases, the DGBs transform into DOGB solutions with non-zero tails that have the form of the upper acoustic cutoff mode. The appearance of such modes, which are associated with resonances of the DGBs with the linear mode, can occur in general in finite-size systems in which the phonon spectrum is discrete. They can be observed when the DGB frequency (or one of its harmonics) penetrates the phonon band. Other kinds of DGB solutions with different non-zero tails are generated when the second harmonic of the DGB penetrates the optical band from above. These solutions, which are called *phonobreathers* [180], have tails of the form of the optical upper cutoff mode and oscillate at a higher frequency (of about f_3).

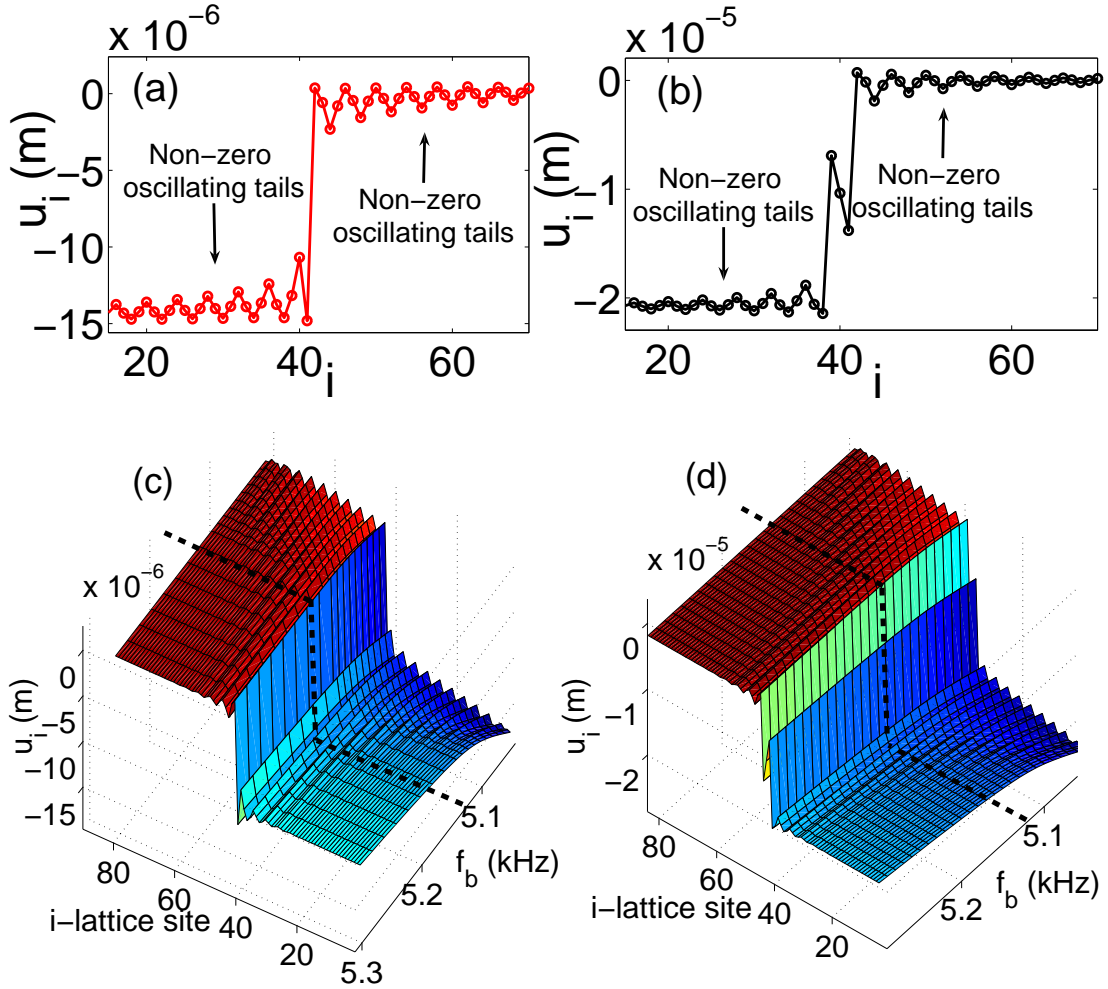


Figure 4.11: Spatial profile of a LA-DGB (a) and an HS-DGB (b) with frequency $f_b = 5210$ Hz. (c,d) Continuation of the DGBs into their discrete out gap siblings as the frequency crosses the upper end of the acoustic band (denoted by dashed lines). The delocalization of the solution profile as the upper acoustic band edge is crossed is evident for both the LA-DGB solutions (c) and the HS-DGB solutions (d).

4.5 Conclusions

In this work, we have presented systematic computations of the intrinsically localized excitations that diatomic granular crystals can support in the gap of its spectrum between the acoustic and optical band of its associated linearization (linearizable under the presence of static compression). We have examined two families of discrete gap breather (DGB) solutions. One of them consists of heavy-symmetric DGBs (HS-DGB), and the other consists of light-asymmetric DGB (LA-DGB), where the

symmetric/asymmetric characterization arises from the spatial profiles of their energy distributions. We found that the HS-DGB branch of localized states is always unstable through the combination of an omnipresent real Floquet-multiplier instability and occasional oscillatory instabilities. We showed that the LA-DGB solutions have the potential to be stable as long as their frequency lies sufficiently close to the optical band edge. For lower frequencies, we observe within a small frequency interval that a real instability and also more broadly weak oscillatory instabilities render this solution weakly unstable, although in this case the solutions still might be observable for very long times. We explored the progressive localization of the solutions upon decreasing the frequency within the gap, and we discussed the regimes of weak, moderate, and strong discreteness at length. We showed a unique spatial profile of DGB with strong discreteness, and their similarity to linear gap surface modes. Finally, in a specific frequency interval near the acoustic band edge of the linear gap, we also found a period-doubling bifurcation and described its associated instability. In the future it should be interesting to explore whether additional families of DGBs (including solutions that do not bifurcate from the linear limit) can exist in 1D or higher dimensional granular crystals.

4.6 Author Contributions

This chapter is based on [148]. G.T. led the theoretical and numerical analysis and wrote the paper. N.B., P.G.K., S.J., M.A.P., and C.D. contributed to the analysis throughout the project and to the editing of the manuscript.

Chapter 5

Defect Modes in Granular Crystals

We study the vibrational spectra of one-dimensional statically compressed granular crystals (arrays of elastic particles in contact) containing defects. We focus on the prototypical settings of one or two spherical defects (particles of smaller radii) interspersed in a chain of larger uniform spherical particles. We measure the near-linear frequency spectrum within the spatial vicinity of the defects, and identify the frequencies of the localized defect modes. We compare the experimentally determined frequencies with those obtained by numerical eigen-analysis and by analytical expressions based on few-site considerations. We also present a brief numerical and experimental example of the nonlinear generalization of a single-defect localized mode.

5.1 Introduction

Defect modes in crystals have long been studied in the realm of solid state physics [68, 181]. The presence of defects or “disorder” is known to enable localized lattice vibrations, whose associated frequencies have been measured in the spectra of real crystals (see [68, 69, 182] and references therein). More recently, this study has been extended to include other examples, including superconductors [70, 71] and electron-phonon interactions [72, 73]. Similar phenomena have also been observed in nonlinear systems, including photonic crystals [74, 75], optical waveguide arrays [76–78], dielectric superlattices (with embedded defect layers) [79], micromechanical cantilever arrays [65, 80], and Bose-Einstein condensates of atomic vapors [81, 82].

Granular crystals are nonlinear systems composed of densely packed particles interacting through Hertzian contacts [21, 52, 84, 102]. These systems present a remarkable ability to tune their dynamic response from linear to strongly nonlinear regimes [21]. This has allowed the exploration of fundamental nonlinear waveforms such as traveling waves [21, 52, 102, 130] and discrete breathers [5]. Granular crystals have also been proposed for several engineering applications, such as energy absorbing layers [99, 100, 138, 139], actuating devices [140], and sound scramblers [127, 128].

The presence of defects in statically uncompressed (or weakly compressed, as compared to the relative dynamic displacements) granular chains excited by impulsive loading has been studied in a number of previous works that have reported the existence of interesting dynamic responses such as the fragmentation of waves, anomalous reflections, and energy trapping [97–100, 118, 119, 138, 139, 183–185]. In this paper, we study the response of strongly compressed granular crystals, with one or two defects (extending our earlier theoretical work [136]), excited by continuous signals. We measure the frequency response of the system and reveal localized modes due to the presence of defects. We report that the number of localized modes mirrors that of the defects, and note that the frequencies of such modes depend on (i) the ratio of the defect mass to the mass of the particles in the uniform chain, (ii) the relative proximity of multiple defects, (iii) the geometric and material properties of the particles composing the crystal, and (iv) the static load. We compare our experimental findings with numerical computations and with theoretical analysis approximating the behavior of a few sites in the vicinity of the defect(s). Finally, we demonstrate that as we go from the linear to the nonlinear regime, nonlinear “deformations” of the linear defect modes (with appropriately downshifted frequencies) are sustained by the system.

5.2 Experimental Setup

We assemble 1D granular crystals, similar to those described in [5, 143], composed of $N = 20$ statically compressed stainless steel spherical particles (316 type, with elastic

modulus $E = 193$ GPa and Poisson ratio $\nu_b = 0.3$ [3]), as shown in figure 5.1(a). The chain is composed of uniform particles of (measured) radius $R = 9.53$ mm and mass $M = 28.84$ g, except for one (or two) light-mass stainless steel defect particles. The spheres are held in a 1D configuration using four polycarbonate bars (12.7 mm diameter) that are aligned by polycarbonate guide plates spaced at approximately 12 cm intervals along the axis of the crystal. The defect particles, which are of smaller radii than the rest of the particles of the chain, are aligned with the axis of the crystal using polycarbonate support rings. Dynamic perturbations are applied to the chain by a piezoelectric actuator mounted on a steel cube (which acts as a rigid wall). The particles are statically compressed by a load of $F_0 = 20$ N. The static load is applied using a soft spring (of stiffness 1.24 kN/m), which is compressed between the last particle in the chain and a second steel cube bolted to the table. The applied static load is measured by a calibrated load cell placed between the spring and the steel cube. We measure the dynamic force signals of the propagating waves with custom-made force sensors consisting of a piezoelectric disk embedded inside two halves of a stainless steel particle with radius $R = 9.53$ mm. The sensor particles are carefully constructed to resemble the mass, shape, and contact properties of the other spherical particles composing the rest of the crystal [116, 127, 128, 138, 145].

5.3 Theoretical Model

We consider the 1D inhomogeneous crystal of N beads as a chain of nonlinear oscillators [21]:

$$\begin{aligned} m_n \ddot{u}_n &= A_n [\Delta_n + u_{n-1} - u_n]_+^p \\ &\quad - A_{n+1} [\Delta_{n+1} + u_n - u_{n+1}]_+^p, \end{aligned} \tag{5.1}$$

where $[Y]_+$ denotes the positive part of Y (which signifies that adjacent particles interact only when they are in contact), u_n is the displacement of the n th sphere (where $n \in \{1, \dots, N\}$) around the static equilibrium, m_n is the mass of the n th particle, and the coefficients A_n depend on the exponent p and the geometry/material properties of adjacent beads. The exponent $p = 3/2$ represents the Hertz law potential

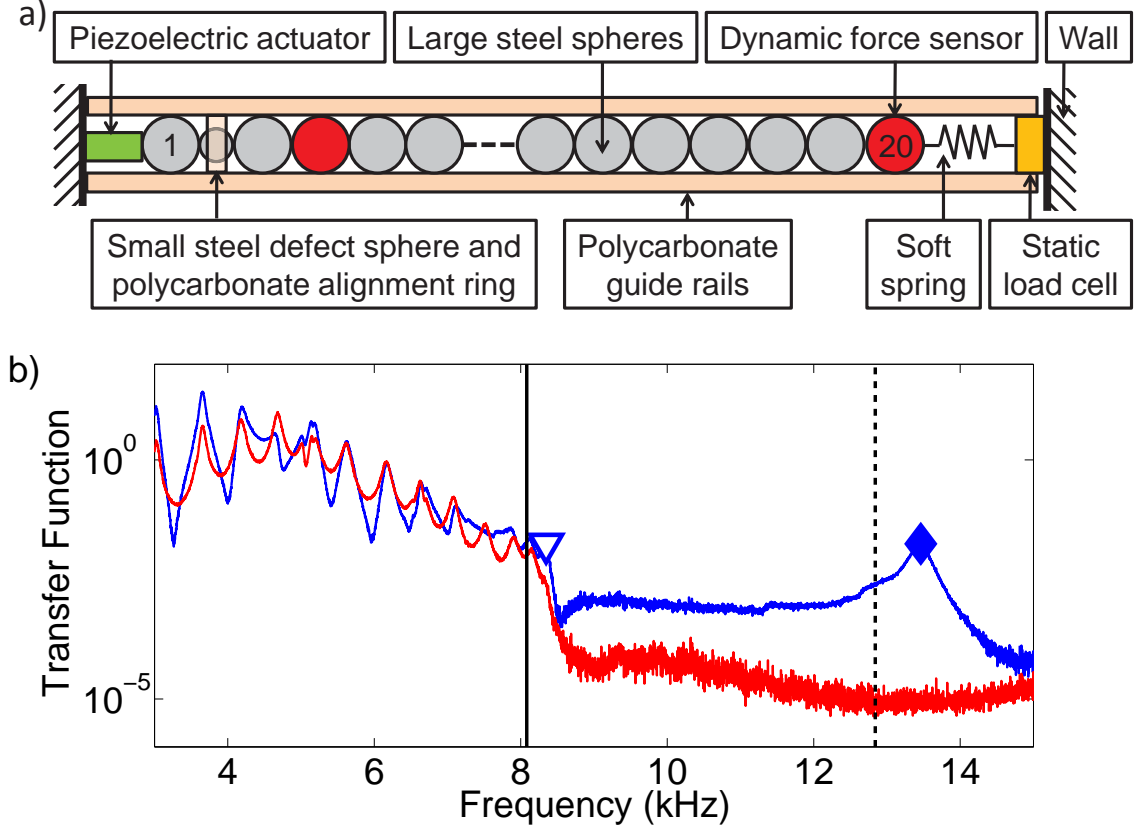


Figure 5.1: a) Schematic diagram of the experimental setup for the homogeneous chain with a single defect configuration. b) Experimental transfer functions (as defined in the “single-defect: near linear regime” section) for a granular crystal with a static load of $F_0 = 20$ N and a defect-bead of mass $m = 5.73$ g located at site $n_{def} = 2$. Blue (dark-grey) [red (light-grey)] curves corresponds to transfer function obtained from the force signal of a sensor particle placed at $n = 4$ [$n = 20$]. The diamond marker is the defect mode. The triangle marker is the upper acoustic cutoff mode. The vertical black dashed line is the theoretically predicted defect mode frequency, and the vertical solid black line is the theoretically predicted upper acoustic cutoff frequency.

between adjacent spheres [84]. In this case, $A_n = \frac{2E}{3(1-\nu^2)} \left(\frac{R_{n-1}R_n}{R_{n-1}+R_n} \right)^{1/2}$, and the static displacement obtained from a static load F_0 is $\Delta_n = (F_0/A_n)^{2/3}$ [21, 84], where R_n is the radius of the n th particle.

In order to study the linear spectrum of the inhomogeneous granular crystal, we linearize equation (5.1) about the equilibrium state under the presence of the static

load. This yields the following linear system [5, 136, 137]:

$$m_n \ddot{u}_n = K_n(u_{n-1} - u_n) - K_{n+1}(u_n - u_{n+1}), \quad (5.2)$$

where $K_n = \frac{3}{2} A_n^{2/3} F_0^{1/3}$. Following [136], we simplify equation(5.2) to the eigensystem:

$$-\omega^2 \mathbf{M} \mathbf{u} = \mathbf{\Lambda} \mathbf{u}, \quad (5.3)$$

where \mathbf{M} is a $N \times N$ diagonal matrix with elements $M_{nn} = m_n$, and \mathbf{u} is the displacement vector. $\mathbf{\Lambda}$ is a $N \times N$ triagonal matrix with elements $\Lambda_{mn} = -[K_n + (1 - \delta_{nN})K_{n+1}]\delta_{mn} + K_{n+1}(\delta_{mn-1} + \delta_{mn+1})$, where δ is the Kronecker delta and we consider left-fixed and right-free boundary conditions. The right-free boundary assumption derives from the low stiffness of the static compression spring (figure 5.1(a)) as compared to the stiffness of the particles in contact.

5.4 Single Defect: Near-Linear Regime

In this section, we study 1D granular crystals that are homogeneous except for one light-mass defect bead at site n_{def} , as shown in figure 5.1(a). Solving the eigenvalue problem of equation (5.3), for such a granular crystal, we obtain the eigenfrequencies and the corresponding spatial profile of the modes of the system. The presence of the single light-mass defect generates a localized mode (see also [118, 136]), centered at the defect site, which we will refer to as the defect mode. The defect mode amplitude decays exponentially away from the defect site and its frequency f_d is such that $f_d > f_c$, where $f_c = \frac{1}{2\pi} \sqrt{\frac{4K_{RR}}{M}}$ is the upper cutoff frequency of the acoustic band of the homogeneous host crystal (where $K_{RR} = \frac{3}{2} A_{RR}^{2/3} F_0^{1/3}$ is the linear stiffness of the contact between two beads with radius R). The spatial profile of this mode consists of adjacent particles oscillating out of phase (see inset in figure (5.2)). As the radius of the defect bead becomes smaller, the difference between f_d and f_c becomes larger, while the defect mode becomes more spatially localized. We observe that for the granular crystals studied here, with radii ratios of $\frac{r}{R} < 0.7$, the defect mode involves the motion of up to approximately three beads, i.e., the displacements of the beads at $n \geq n_{def} + 2$ and $n \leq n_{def} - 2$ are negligible. Because in this range of radii ratio the motion of the particles can be accurately approximated by three beads, we

consider the particles at $n = n_{def} \pm 2$ as fixed walls, in order to find an analytical approximation for the frequency of the defect mode. Solving for the eigenfrequencies of this reduced three-bead system, we find that the mode corresponding to the out of phase motion can be analytically approximated by equation (5.4)

$$f_{3bead} = \frac{1}{2\pi} \sqrt{\frac{2K_{Rr}M + K_{RR}m + K_{Rr}m + \sqrt{-8K_{Rr}K_{RR}mM + [2K_{Rr}M + (K_{RR} + K_{Rr})m]^2}}{2mM}} \quad (5.4)$$

where $K_{Rr} = \frac{3}{2}A_{Rr}^{2/3}F_0^{1/3}$ is the linear stiffness of the contact between a defect-bead and a bead of radius R .

We conduct experiments to identify the frequency of the defect mode in granular crystals with a single light-mass defect as shown in figure 5.1(a). We place the defect particle at site $n_{def} = 2$ (close to the actuator) so that the energy applied by the actuator, at the defect mode frequency, will not be completely attenuated by the uniform crystal, which acts as a mechanical frequency filter before it arrives at the defect site. Because of the localized nature of the defect mode, placing a defect particle (of radius $r \leq 7.14$ mm) at site $n_{def} = 2$ or further into the chain makes nearly no difference on the frequency of the defect mode. For instance, for a defect particle of radius $r = 7.14$ mm, we numerically calculate (using equation 5.3) the difference in the defect mode frequency for the cases where a defect particle is placed at site $n_{def} = 2$ or $n_{def} = 10$, to be 3 Hz. Conversely, because of the presence of the fixed boundary and the larger localization length of the defect mode, for a defect particle of $r = 8.73$ mm, we calculate the difference in defect mode frequency, between sites $n_{def} = 2$ and $n_{def} = 10$, to be 68 Hz. The defect particles are stainless steel spheres of smaller radii, $r = [3.97, 4.76, 5.56, 6.35, 7.14, 7.94]$ mm, and measured masses of $m = [2.08, 3.60, 5.73, 8.54, 12.09, 16.65]$ g, respectively. We experimentally characterize the linear spectrum of this system by applying low amplitude (approximately 200 mN) bandwidth limited noise (3 – 25 kHz for the two smallest defect particles, and 3 – 15 kHz otherwise) via the piezoelectric actuator. We calculate the transfer functions, specific to the sensor location, by averaging the Power Spectral Densities (PSD [147]) of 16 force-time histories, measured with the embedded sensors, and dividing by the average PSD level in the 3 – 8 kHz range (corresponding to the acoustic band). We

embed sensors in particles at sites $n = 4$ and $n = 20$. In figure 5.1(b) we show the transfer functions for the granular crystal with defect radius $r = 5.56$ mm. The red (light-grey) and blue (dark-grey) curves are the transfer functions for the sensors at sites $n = 4$ and $n = 20$, respectively. We denote the experimental cutoff frequency by the triangular marker (found by identifying the last peak in the acoustic band) and defect frequency as the diamond marker on the $n = 4$ transfer function. The vertical lines denote the theoretically determined upper cutoff frequency of the acoustic band and the defect frequency (equation 5.4). The presence of the defect mode can be clearly identified in the vicinity of the defect (at $n = 4$), but is not visible far from the defect (at $n = 20$).

We repeat the process of measuring the transfer function and identifying the defect mode frequency 16 times, reassembling the crystal after each repetition. In figure 5.2, we plot the average frequency of the 16 experimentally identified defect modes as a function of the mass ratio $\frac{m}{M}$ (blue [dark-grey] solid line connecting the closed diamonds). We also plot, for comparison, the defect frequency predicted by the analytical expression of equation (5.4) (green [light-grey] dashed line connecting the crosses), and the numerical eigenanalysis of equation (5.3) corresponding to the experimental setup (black solid line connecting the open diamonds). The error bars on the experimental data are $\pm 2\sigma$ where σ is the standard deviation of the identified defect frequencies over the 16 repetitions. Comparing the analytical three-bead approximation with the numerical eigenfrequencies, we find an excellent agreement for mass ratios of $\frac{m}{M} < 0.6$. Comparing the experimental data with the numerics, we find an upshift of 5%-10%, similar to the upshift observed in [5, 143]. For the $r = 5.56$ mm defect, the average experimental defect frequency is $f_d^{exp} = 13.59$ kHz and the average experimental cutoff frequency is $f_c^{exp} = 8.36$ kHz. In comparison, the theoretical three-bead approximation gives a defect frequency of $f_d^{3bead} = 12.84$ kHz and the eigenproblem of equation (5.3) gives a defect frequency of $f_d^{num} = 12.85$ kHz, while the analytically calculated cutoff frequency was $f_c = 8.02$ kHz.

Possible reasons for these upshifts have been identified in [5, 143] and the references therein, such as error in the material parameters, nonlinear elasticity, surface

roughness, dissipative mechanisms and misalignment of the particles. We note that a systematic error in the measurement of the static load could also cause such an upshift. Nevertheless, it is clear from figure 5.2 that the functional dependence of the relevant frequencies on the mass ratio (of defect to regular beads) is accurately captured by our analytical and numerical results.

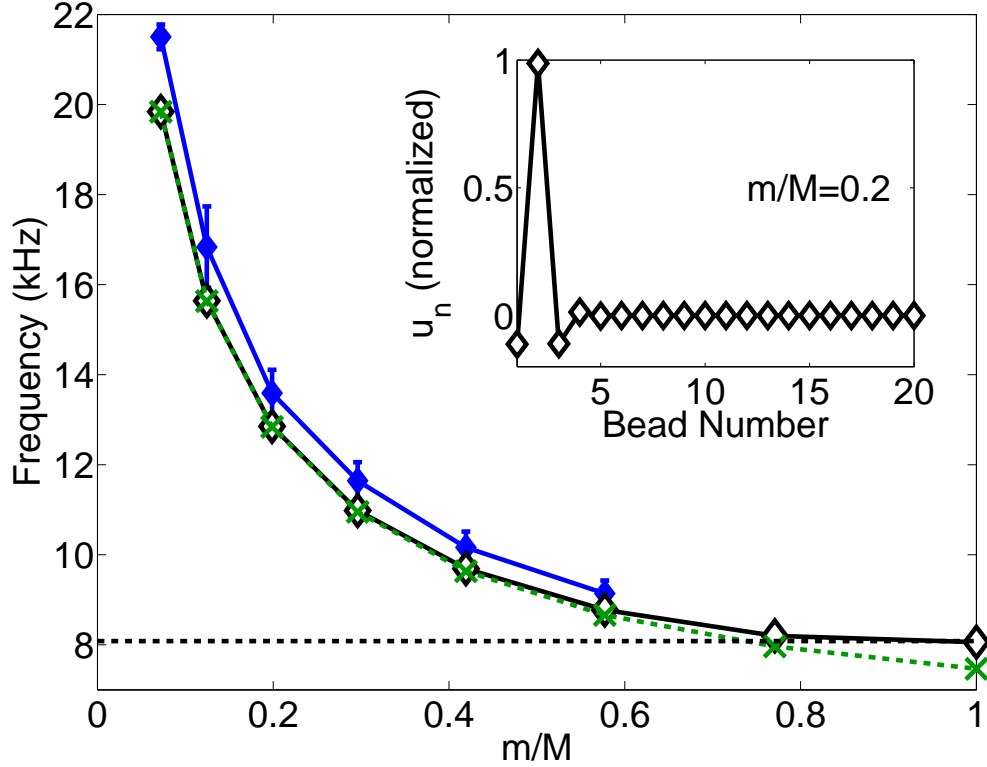


Figure 5.2: Frequency of the defect mode, with defect-bead placed at $n_{def} = 2$, as a function of mass ratio m/M . Solid blue line (dark grey, closed diamonds) corresponds to experiments, solid black line (open diamonds) to numerically obtained eigenfrequencies (see equation (5.3)), and green dashed line (light grey, x markers) to the analytical prediction of the three-beads approximation (see equation (5.4)). The error bars account for statistical errors on the measured frequencies and are $\pm 2\sigma$. Inset: The normalized defect mode for $\frac{m}{M} = 0.2$.

5.5 Two Defects: Near-Linear Regime

We study granular crystal configurations with two identical light-mass defects to better understand the effects of increasing heterogeneity on the spectral response of the system. The localized mode due to the presence of a light-mass defect (for mass ratios $\frac{m}{M} < 0.6$) has a spatial localization length of about three particles (larger particles have a greater localization length, and smaller particles have a shorter localization length), as described in the one-defect case and shown in figure 5.2. We can thus expect that two light-mass defects placed far from each other in a granular crystal (sufficiently outside this localization length) would have similar frequencies and mode shapes independent of the presence of the other. However, as the two defect particles are brought closer together (within the localization length), each mode influences the other. For a sufficiently small mass ratio, this results in the creation of two defect modes at different frequencies; one with the defect particles moving out of phase, and the other with the defect particles moving in phase. For the case of nearest-neighbor identical defects, our theoretical analysis can be extended by using a four-particle analogy. In this case, using the notation $s_1 = K_{Rr}(M + m) + K_{RR}m$, $s_2 = -4K_{Rr}K_{RR}Mm + (K_{RR}m + K_{Rr}(M + m))^2$, $s_3 = s_1 + 2K_{rr}M$ and $s_4 = -4(2K_{rr}K_{RR} + K_{Rr}(2K_{rr} + K_{RR}))Mm + (2K_{rr}M + K_{RR}m + K_{Rr}(M + m))^2$, we obtain the following frequencies

$$f_{4bead}^{(1)} = \frac{1}{2\pi} \sqrt{\frac{1}{2Mm} (s_1 \pm \sqrt{s_2})}, \quad (5.5)$$

$$f_{4bead}^{(2)} = \frac{1}{2\pi} \sqrt{\frac{1}{2Mm} (s_3 \pm \sqrt{s_4})}. \quad (5.6)$$

The two highest frequencies correspond to the linear defect mode frequencies. Naturally, this analytical approach can be extended to more distant defects, although we do not present such algebraically intensive cases here.

In figure 5.3, we show the behavior of two $r = 5.56$ mm defects in a $N = 20$ particle granular crystal under $F_0 = 20$ N static load (similar to the configuration shown in figure 5.1(a)), where the first defect is at site $k = n_{def1} = 2$ and the second

defect is at a variable position between site $l = n_{def2} = 3$ and $l = n_{def2} = 6$. We use the same experimental method as in the single defect case except now we use a noise range between 3 kHz and 20 kHz, and we place the first sensor at $n = l + 1$. We show the experimentally determined PSD transfer function for the case of $l - k = 1$ in figure 5.3(a), with sensors at site $n = 4$ (blue [dark grey]) and $n = 20$ (red [light grey]). As described in [136], the existence of two separate defect modes for the case where the defect particles are adjacent to each other ($l - k = 1$), depends on the mass ratio of the defect particles to those of the rest of the crystal. Here the mass ratio is such that two modes are present, as can be seen in the blue (dark-grey) curve in figure 5.3(a). The two distinct modes, which we denote by the open square and closed circular markers, have frequencies above the acoustic band. The square markers denote the mode with defect beads moving out of phase, and the closed circular marker corresponds to the mode with defect particles moving in phase, as shown by the numerically calculated eigenmodes in figure 5.3(c) and (d) respectively [136]. In figure 5.3(b) we plot the experimentally determined frequencies of both modes as a function of the interdefect particle distance ($l - k$). The solid blue (dark-grey) lines are the experimental data, and the dashed black lines are the frequencies obtained from solving the eigenvalue problem of equation (5.3). The green (light-grey) x-markers denote the frequencies calculated with equations (5.5)-(5.6), for the $l - k = 1$ case. It is evident that the analytical results agree closely with the numerically calculated eigen-frequencies. The error bars on the experimental data correspond to the $\pm 2\sigma$ standard deviation as calculated in the single-defect case. We see close qualitative agreement between the experimental data and the numerical predictions, but also the same systematic upshift as observed in the single defect case and [5, 143]. From figure 5.3(b) we can see that as the defects are placed three or more particles apart, the frequencies of the defect modes converged to approximately the same value, suggesting the defects respond independently of each other.

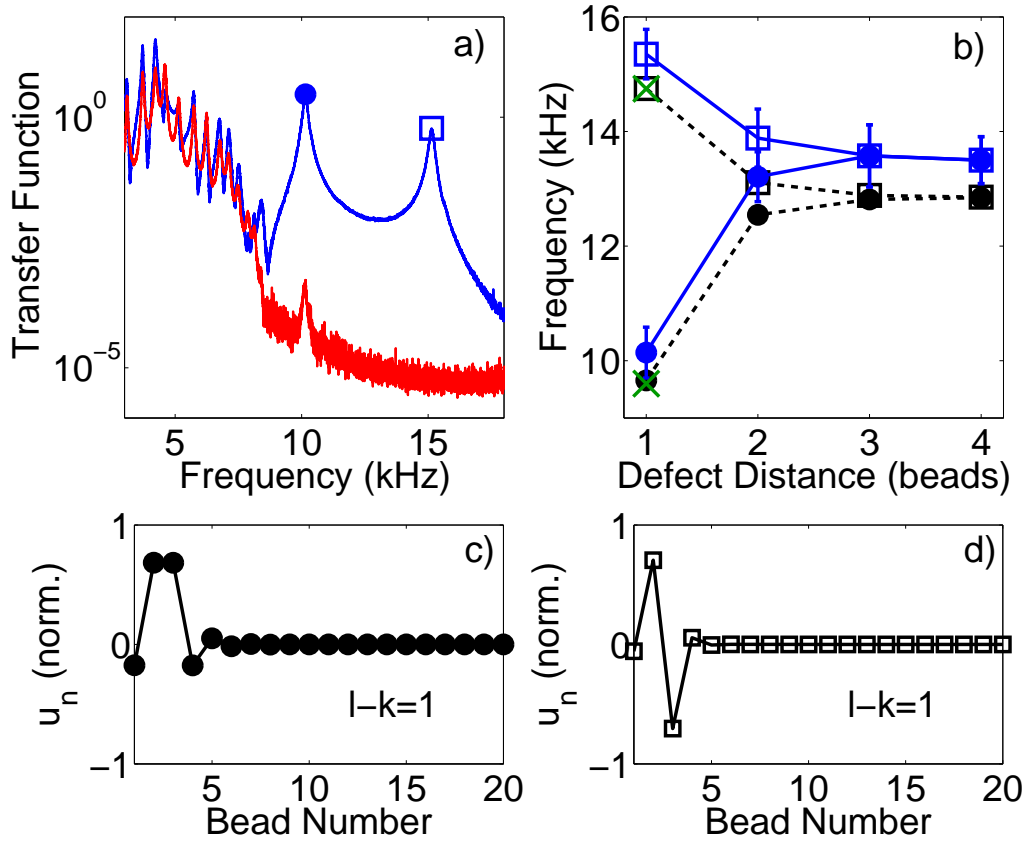


Figure 5.3: (a) Experimental transfer functions for a granular crystal with two defect-beads of mass ratio $\frac{m}{M} = 0.2$ at $n_{def} = 2$ and $n_{def} = 3$ (in contact). Blue (dark grey) [red (light grey)] curve corresponds to transfer function obtained from the force signal of a custom sensor placed at $n = 4$ [$n = 20$]. (b) Frequencies of the defect modes as a function of the distance between them. The solid line denotes experimental data, the dashed line the numerically obtained eigenfrequencies, and the x markers the frequencies from the analytical expressions of equations (5.5)- (5.6). (c),(d) The normalized defect mode shapes corresponding to the defect modes identified in (a) with frequency of the same marker type.

5.6 Single Defect: Nonlinear Localized Modes

As shown in [136], the interplay of the inherent nonlinearity of the granular crystal with the linear localization due to the defect results in the presence of robust nonlinear localized modes (NLMs). The frequency of these modes depends not only on the static load and the material values of the beads, but also on the amplitude of the oscillations. In order to find this dependence, we apply Newton's method (see [136] and references

therein) for the experimental, single-defect, configuration of figure 5.1(a). For the numerical calculations in this section, we calculate experimental contact coefficients following a procedure similar to the one described in [5]. The experimental contact coefficients obtained are $A_{RR}^{exp} = 10.79 \text{ N}/\mu\text{m}^{3/2}$ for the contact between two $R = 9.53 \text{ mm}$ beads and $A_{rR}^{exp} = 9.95 \text{ N}/\mu\text{m}^{3/2}$ for the contact between the $R = 9.53 \text{ mm}$ and the $r = 5.56 \text{ mm}$ beads. In comparison, the values of the coefficient A , as calculated by the material values and used for the previous sections of the paper, are $A_{RR} = 9.76 \text{ N}/\mu\text{m}^{3/2}$ and $A_{Rr} = 8.38 \text{ N}/\mu\text{m}^{3/2}$.

In figure 5.4(a), we show the frequency of the numerically determined NLM as a function of the averaged dynamic force for the particle at site $n = 3$. The latter corresponds to the average of the two dynamic contact forces adjacent to the particle, which is analogous to what is measured experimentally by the dynamic force sensor [128]. In figure 5.4(b), we plot the numerically determined normalized NLM shape at $f_b = 13.28 \text{ kHz}$. Comparing this NLM shape to the linear mode shape of the same frequency (see inset of figure 5.2), we can see that the NLM has a slightly modified (more asymmetric) spatial profile.

The experimental setup used for the study of the NLMs is the same as in the case of the linear single defect experiments (as shown in figure 5.1(a)) except we place sensors in particles at sites $n = 3$, $n = 5$, and $n = 20$. Additionally, we replace the $n = 1$ particle with an embedded actuator particle, so as to apply high amplitude (approximately 10 N), short time pulse (approximately 100 μs) perturbations directly to the defect particle. Exciting such a pulse creates an initial condition in the crystal that resembles the predicted defect NLM shape. The embedded actuator particle is similar in construction to the sensors but with a piezoceramic construction/geometry more appropriate for high force amplitude actuation (Piezomechanik PCh 150/5x5/2 Piezo-chip).

The force-time history of the dynamic force measured by the sensor at site $n = 3$ is shown in figure 5.4(c). A sharp excitation is evident at time $t = 0$, followed by periodic oscillations with a decaying envelope, due to the inherent dissipation in the system. As shown by the parametric continuation in figure 5.4(a), NLMs corresponding to

the defect mode at higher amplitudes have a frequency deeper into the gap than its linear counterpart. However, for the amplitudes observed here this is only a slight shift (up to 200 Hz over 7 N).

We study, in more detail, the response of two selected time regions of the force-time history shown in figure 5.4(c), to experimentally demonstrate the frequency shift characteristic of higher amplitude NLMs. The two non-overlapping time regions are of length $T = 5.1$ ms. The red (light-grey) time region begins immediately following the arrival of the initial actuated pulse, and presents a maximum amplitude of 7 N. The blue (dark-grey) time region starts $T = 6$ ms after the beginning of the previous time region, and presents a maximum amplitude of 1.3 N. We calculate PSDs for both time regions (frequency resolution $\delta f = 195$ Hz) as shown in figure 5.4(d). The PSDs shown in figure 5.4(d) correspond to the time regions of the same color shown in figure 5.4(c). Here, the PSDs are normalized by dividing the PSD by the peak PSD amplitude of the identified defect mode. It is evident that the peak in the PSD spectrum corresponding to the time region with larger force amplitude presents a lower characteristic frequency (i.e., it is further into the gap) with respect to the peak representing the time region with lower force amplitudes. This is in agreement with the shift predicted by the parametric continuation analysis shown in figure 5.4(a). The peak frequency of the PSD of the high force amplitude time region is $f_{def} = 13.28$ kHz, and the peak frequency of the PSD of the low amplitude time region is $f_{def} = 13.48$ kHz, where $f_{def} = 13.48$ kHz is closer to the mean experimentally determined linear defect mode frequency (shown by the dashed line in figure 5.4(d)).

5.7 Conclusions

We studied the response of statically compressed granular crystals containing light-mass defects, and characterized their near-linear spectra by applying continuous excitation. We demonstrated that such chains support localized modes with frequencies above that of their acoustic band cutoff, using approximate few-bead analytical cal-

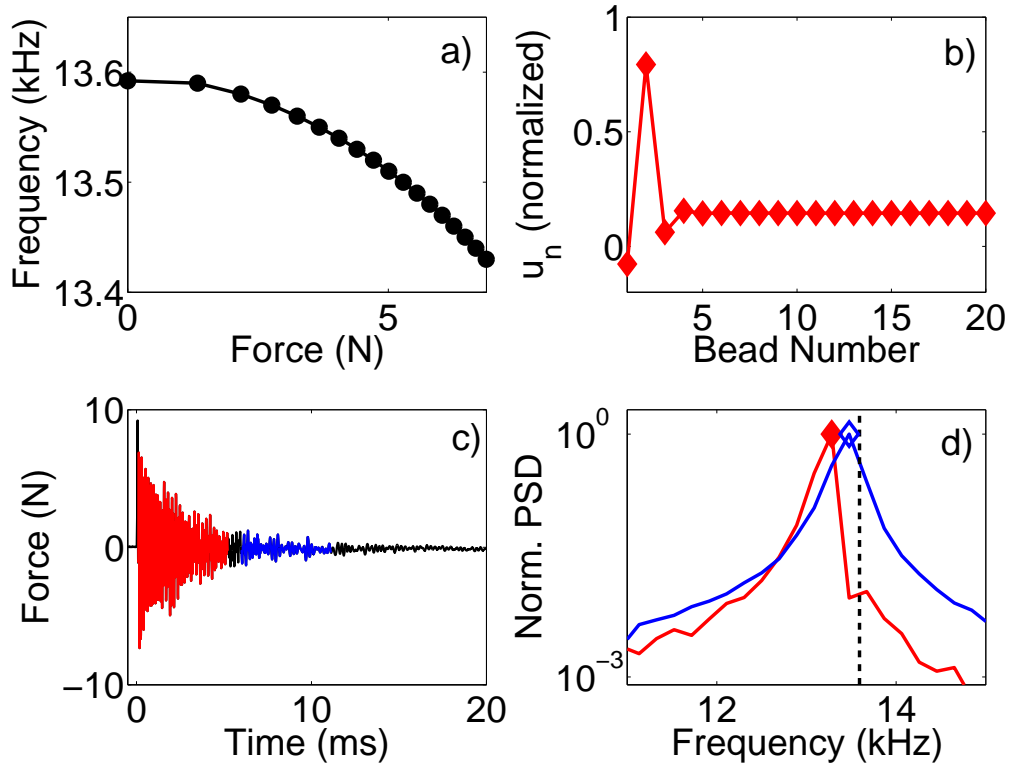


Figure 5.4: (a) Numerical frequency continuation of the nonlinear defect modes corresponding to the experimental setup in figure 5.1(a). (b) Numerically calculated spatial profile of the nonlinear localized mode with frequency $f_{def} = 13.28$ kHz. (c) Measured force-time history of a sensor at site $n = 3$, where a high amplitude, short width, force pulse is applied to the granular crystal. (d) Normalized PSD for the measured time regions of the same color in (c); closed and open diamonds correspond to the high and low amplitude time regions respectively. The vertical dashed line is the mean experimentally determined linear defect mode frequency.

culations, numerics, and experiments. The number of supported localized modes depends on the number of defects, while their frequencies depend on the inter-defect distance, on the ratio $\frac{m}{M}$ of defect to regular masses (and the geometric/elastic properties of the beads), and on the static load. We also briefly described the nonlinear generalizations of such modes, departing from the near-linear regime, and showed a downshift of the corresponding defect mode frequencies with increasing amplitude. This study is important for understanding the interplay of disorder and nonlinearity in discrete systems, and the results reported may be relevant in the design of

applications involving vibrational energy trapping.

5.8 Author Contributions

This chapter is based on [144]. N.B. led the experimental work. G.T. led the theoretical and numerical analysis. Y.M. carried out the experiments and some of the numerical simulations. C.D. and P.G.K. provided guidance and contributed to the design and analysis throughout the project. All authors contributed to the writing and editing of the manuscript.

Chapter 6

Bifurcation-Based Acoustic Switching and Rectification

Switches and rectification devices are fundamental components used for controlling the flow of energy in numerous applications. Acoustic [45, 186] and thermal [187–190] rectifiers have been proposed for use in biomedical ultrasound applications [45], thermal computers [188, 191], energy saving and harvesting materials [188, 189], and direction-dependent insulating materials [187–190]. In all these systems the transition between transmission states is smooth with increasing signal amplitudes. This limits their effectiveness as switching and logic devices, and reduces their sensitivity to external conditions as sensors. Here we overcome these limitations by demonstrating a new mechanism for tunable rectification that utilizes bifurcations and chaos. This mechanism has a sharp transition between states, which can lead to phononic switching and sensing, and can be used in logic devices. It also redistributes the input energy to lower frequencies, which can lead to more flexible energy harvesting systems. We present the first experimental demonstration of this mechanism, applied in a mechanical energy rectifier operating at variable sonic frequencies. The rectifier is a granular crystal, composed of a statically compressed one-dimensional array of particles in contact, containing a light mass defect near a boundary. These systems are nonlinear and contain tunable pass and stop bands in their dispersion relation. Because of the defect, vibrations at selected frequencies cause bifurcations and a subsequent jump to quasiperiodic and chaotic states with broadband frequency

content. We use this combination of frequency filtering and asymmetrically excited bifurcations to obtain rectification. We calculate rectification ratios greater than 10^4 . Because the concepts governing wave propagation in periodic structures and nonlinear/chaotic dynamics are common to many systems, we envision this mechanism to enable the design of advanced photonic, thermal, and acoustic materials and devices.

6.1 Introduction

Periodicity in materials has proven useful for the control of wave propagation in electronic and photonic [28], mechanical [12], acoustic [40], and optomechanical systems [192]. The presence of nonlinearity in periodic dynamical systems makes available an array of useful phenomena (including localization, breathers, bifurcation, and chaos) [15–20]. Here we study how the interplay of periodicity, nonlinearity, and asymmetry in granular crystals results in novel types of switching and rectification devices.

Granular crystals are densely packed arrays of elastic particles that interact nonlinearly via Hertzian contacts, and are periodic and nonlinear systems [21, 84]. These systems are tunable from near-linear to strongly nonlinear dynamical regimes, by changing the ratio of static to dynamic interparticle displacements [21, 22]. Granular crystals have allowed the exploration of fundamental phenomena [5, 21, 22, 102, 108, 118, 137, 144] and have been applied in engineering devices [100, 141, 145]. Here we study a granular crystal that is a statically compressed 1D array of $N = 19$ stainless steel spherical particles (figure 6.1(a)(b)). The particles are of measured radius $R = 9.53$ mm and mass $M = 28.84$ g, except for a single defect particle, of radius $r = 5.56$ mm and mass $m = 5.73$ g placed at the second site from the left boundary. Longitudinal dynamic displacements are applied with a piezoelectric actuator and the crystal is compressed mechanically (see Methods). Two configurations are studied: one with the actuator on the right (“reverse configuration,” figure 6.1(a), and the other with the actuator on the left (“forward configuration,” figure 6.1(b)). The dynamic force-time history of the propagating waves is measured with in-situ piezoelectric sensors [145]. In both configurations, one sensor is placed four sites from

the actuator and the other is placed at the other end.

A statically compressed homogeneous granular crystal acts as a low-pass frequency filter [5, 108, 137]. When the particles are identical, the crystal supports one band of propagating frequencies called the acoustic band, extending from frequency $f = 0$ to the upper acoustic band cutoff frequency f_c . Vibrations with frequencies $f > f_c$ lie in a band gap and cannot propagate through the crystal [12]. The presence of a light-mass defect breaks the periodicity of the crystal and induces an exponentially localized mode with frequency $f_d > f_c$ [118, 144]. Frequencies f_c and f_d depend on the geometric and material properties of the system and are proportionally tunable with static load (see Methods) [5, 108, 118, 137, 144]. The experimental characterization of the linear spectra can be seen in Supplementary figure 6.5.

6.2 Rectifier Concept

A schematic of our rectifier concept is shown in figure 6.1(c)(d). We drive one end of the chain harmonically. We fix the frequency of the driver f_{dr} at a frequency in the gap, below f_d , and increase the amplitude δ . Because of the band gap, in the reverse direction, the energy provided by the actuator does not propagate through the crystal. In the forward configuration, for low driving amplitudes, the actuator excites a periodic (at frequency f_{dr}) vibrational mode localized around the defect. In this case, the energy also does not propagate through the crystal. As the amplitude of the driver is increased, the system jumps from this low amplitude stable periodic solution to a high amplitude stable two-frequency quasiperiodic mode: one frequency is at f_{dr} and the other is at frequency f_N . In our nonlinear system, this results in the distribution of energy to frequencies that are linear combinations of these two frequencies, including energy at low frequencies within the propagating band. Further increase of the driving amplitude induces chaotic vibrations, where the energy is redistributed along broad frequency bands surrounding the peaks of the quasiperiodic state. In both quasiperiodic and chaotic states the energy at low frequencies is transmitted (see figure 6.3).

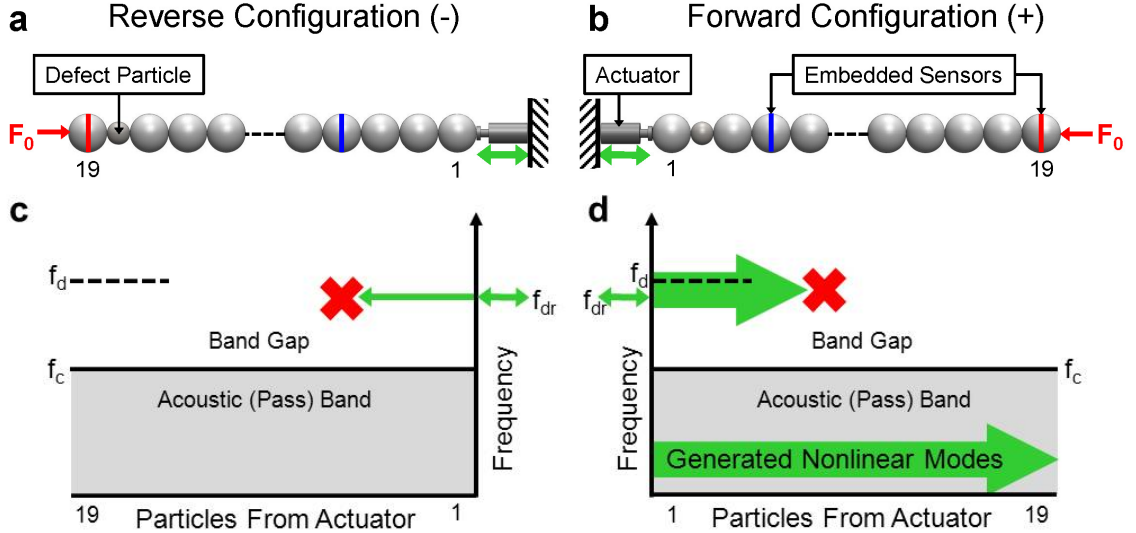


Figure 6.1: Schematics and conceptual diagrams. (a,b) Schematics of the granular crystal used in experiments, composed of 19 stainless steel spherical particles, a light mass defect, and applied static load F_0 . Vertical lines in the spheres indicate the sensor particles. (c,d) Conceptual diagrams of the rectification mechanism. f_d is the defect frequency, f_c is the acoustic (pass) band cutoff frequency, and f_{dr} is the driving frequency. (a,c) Reverse configuration: driving far from the defect, the bad gap filters out vibrations at frequencies in the gap (f_{dr}). (b,d) Forward configuration: driving near the defect, nonlinear modes are generated which transmit through the system.

6.3 Bifurcations

To understand the transition between states occurring in the forward configuration of our system, we conduct parametric continuation using the Newton-Raphson (NR) method in phase space [5] and numerical integration of equation (6.1) (see Methods and Supplementary Information). To account for the dissipation in our system, we use linear damping (a damping timescale $\tau = 1.75$ ms is selected to match experimental results). The actuator boundary is modeled as a moving wall, and the opposite as a free boundary with applied force. Applying NR, we follow the periodic family of solutions as a function of driving amplitude δ and study its linear stability. figure 6.2 shows the maximum dynamic force amplitude ($F_0 = 8$ N, $f_{dr} = 10.5$ kHz, four particles from the actuator) for each solution as a function of the driving amplitude. The stable (unstable) periodic solutions are denoted with solid blue (dashed

black) lines. At turning points 1,2, stable and unstable periodic solutions collide and mutually annihilate (saddle-center bifurcation [15]). At points 3,4, the periodic solution changes stability and a new two-frequency stable quasiperiodic state emerges (Naimark-Sacker bifurcation [16]). Because of the demonstrated bifurcation picture, we predict, with increasing amplitude, a progression of the system response following the low amplitude stable periodic solution up to point 1, where the system will jump past the unstable periodic solution to the high-amplitude stable quasiperiodic state.

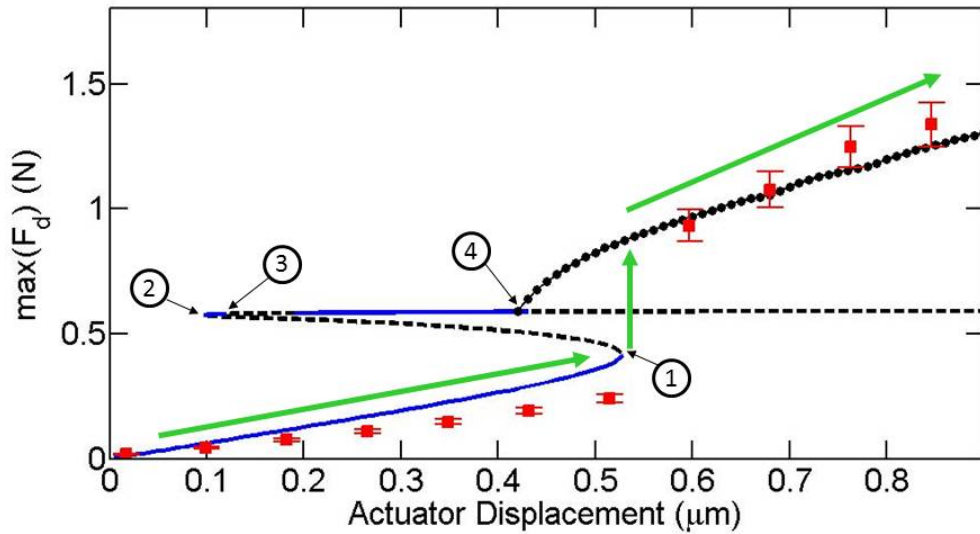


Figure 6.2: Bifurcation and stability. Maximum dynamic force at the fourth particle from the actuator in the forward configuration as a function of driving amplitude δ (i.e. the actuator displacement). Red square markers are experimental data corresponding to the ($f_{dr} = 10.5$ kHz, $F_0 = 8$ N) configuration shown in figures 6.3 and 6.4. Error bars are based on the range of actuator calibration values. The solid blue (dashed black) line corresponds to the numerically calculated stable (unstable) periodic branches. The dotted blue line corresponds to the numerically calculated quasiperiodic branch. Green arrows denote the path (and jump) followed with increasing driving amplitude. The circled numbers correspond to bifurcation points.

6.4 Experimental Response and Power Spectra

To demonstrate this jump, we harmonically drive the granular crystal of figure 6.1, at frequency $f_{dr} = 10.5$ kHz ($\delta f = f_d - f_{dr} \approx 500$ Hz, $f_c = 6.9$ kHz, $F_0 = 8$ N).

The driving amplitude is set to δ for 90 ms, except for the first and last 20 ms where the driving amplitude is linearly increased and decreased, respectively. The linear ramp allows us to follow the low amplitude stable periodic state (see figure 6.2). The maximum dynamic force measured by the sensors is plotted with the red square markers in figure 6.2. The path followed with increasing amplitude is highlighted with the green arrows. figure 6.3 demonstrates each of the states. The dynamic force F_d experimentally measured by the sensor four particles from the actuator is shown in the left panels. The subscript of the driving amplitude δ denotes the direction, where (+) and (-) are the forward and reverse configurations, respectively. The power spectral densities (PSDs) of the highlighted time region are calculated for both sensors (right panels of figure 6.3). Each curve corresponds to the sensor of the same color and configuration as in figure 6.1a,b. In the forward configuration, at low driving amplitude ($\delta_{(+)} = 0.43$ m, figure 6.3a,b), a periodic response is observed, with no energy propagating above the noise floor. At higher driving amplitudes ($\delta_{(+)} = 0.60$ m, figure 6.3c,d) a quasiperiodic response is observed with the generation of a second frequency $f_N = 10.13$ kHz, and the linear combinations thereof. The combinations within the pass band are transmitted. Increasing the amplitude further ($\delta_{(+)} = 0.85$ m, figure 6.3e,f), a chaotic response is seen, where the area between the frequencies in figure 6.3d, is filled in. By reversing the crystal, even at high amplitudes ($\delta_{(-)} = 0.85$ m, figure 6.3g,h) no transmission is observed, which illustrates the rectification effect.

6.5 Experimental Rectifier Tunability

This rectification behavior can also be tuned over a broad range of frequencies by varying the static load. To demonstrate the rectifier tunability, we measure the average transmitted signal power P_{exp} (area under the PSD curves from 0 kHz to 20 kHz) as a function of actuator displacement (figure 6.4a), for two different static loads (and driving frequencies). The black curve corresponds to the configurations in figures 6.1–6.3, and the red curve is for a static load of $F_0 = 13.9$ N ($f_{dr} = 11.4$ kHz,

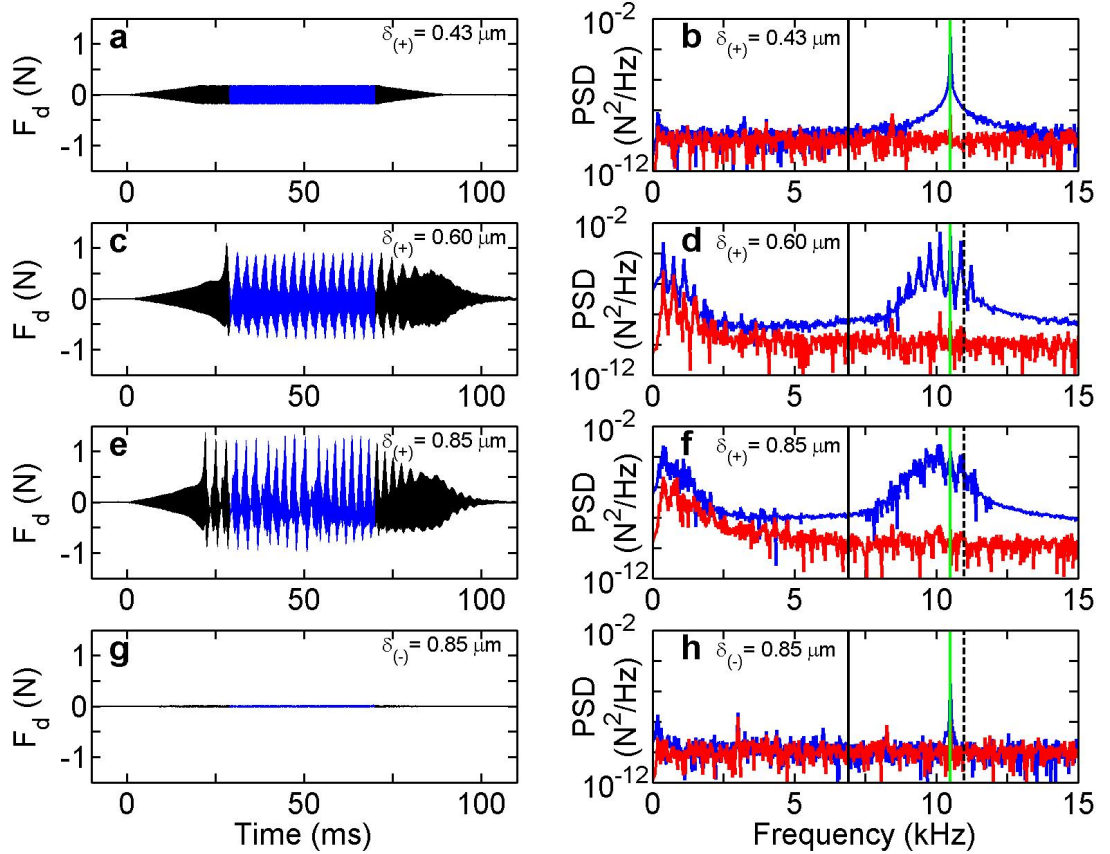


Figure 6.3: Experimental force-time response and power spectra. (a-f) Forward configuration. (g,h) Reverse configuration. (a,c,e,g) Experimentally measured force-time history for the sensor four particles from the actuator ($f_d = 10.5$ kHz, varied amplitudes/configurations). The blue (dark grey) is the time region used to calculate the PSDs. (b,d,f,h) PSD of the measured force-time history for the sensors four (blue [dark grey]) and 19 particles from the actuator (red [light grey]). The vertical black solid line is the upper acoustic band cutoff frequency f_c , the black dashed line the defect mode frequency f_d , and the green (light grey) line the driving frequency f_{dr} .

$\delta f \approx 550$ Hz). For these two configurations the power transmitted is at maximum 1.7% of the input power. Changing the static load causes f_d to change (see Methods). This allows the rectifier to operate within a wide range of driving frequencies. In both cases an asymmetric (with respect to directional configuration) energy transmission is observed, with a sharp transition between periodic and quasiperiodic/chaotic states.

6.6 Numerical Modeling

Numerical integration of equation (6.1) shows the same qualitative response as in the experiments (see figure 6.4b and Supplementary figures 6.6 and 6.7). In figure 6.4b we plot the numerically calculated average transmitted power P_{num} , for the same configurations (corresponding to the same colors) as in figure 6.4a. Below the experimental noise floor, in the reverse configuration, the increasing transmission corresponds to $f_s = f_{dr}/2$ subharmonic generation. This phenomenon is generally present at high amplitudes in nonlinear systems, though it could be avoided by using a sufficiently small defect with subharmonic frequency in the gap. To calculate the energy rectification ratio, we plot the time-averaged energy density (per particle site) as a function of particle number, for the reverse ($E_{avg,(-)}$, figure 6.4c) and forward ($E_{avg,(+)}$, figure 6.4d) configurations. Each curve in figure 6.4c,d corresponds to the numerical run in figure 6.4b of the same marker type. As shown by the square markers in figure 6.4c (figure 6.4d), for high amplitudes, the system decays exponentially down to level of the generated subharmonic (low frequency component of the generated nonlinear mode). In both directions (figure 6.4c,d) at low driving amplitude the system decays exponentially down to the numerical noise floor. In this case the maximum rectification ratio $\sigma = E_{avg,(+)}/E_{avg,(-)}$ for the particle furthest from the actuator is $\sigma \approx 10^4$.

6.7 Conclusions

The combination of the demonstrated rectification and jump phenomena allows the system to function as switching, sensing, and logic devices. By operating close to the bifurcation point, small perturbations cause the system's response to switch from the low-amplitude non-transmitting state to the high-amplitude transmitting state. We also show in the Supplementary Information (figure 6.8) how such rectifiers can be configured as AND and OR logic gates. The demonstrated frequency downshifting is also useful for increased flexibility in energy systems, for instance in energy harvest-

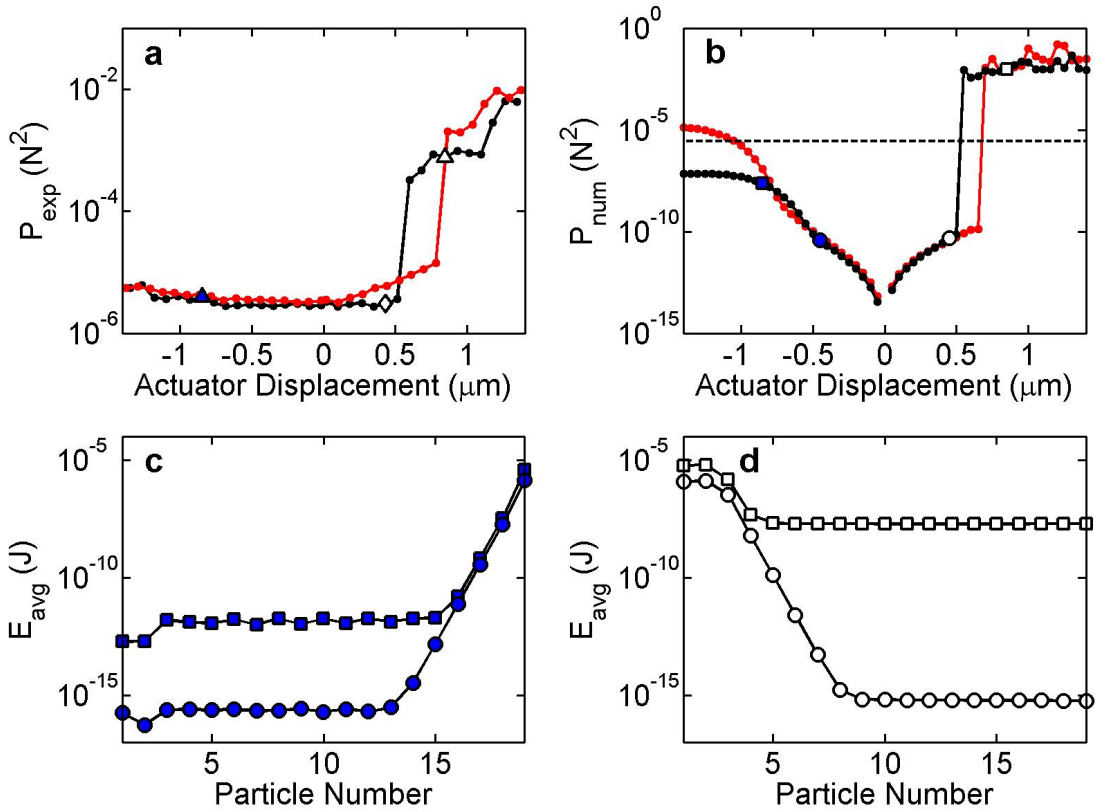


Figure 6.4: Power transmission and energy distribution. (a) Experimental and (b) numerical average transmitted power as a function of driving amplitude δ . The black curve corresponds to $F_0 = 8.0$ N ($f_{dr} = 10.5$ kHz) and the red (light grey) curve to $F_0 = 13.9$ N ($f_{dr} = 11.4$ kHz). Positive/negative displacements denote forward/reverse configurations, respectively. The horizontal black dashed line in (b) is the experimental noise floor. Numerical time-averaged energy density as a function of position for the (c) reverse and (d) forward configurations. (c,d) each curve corresponds to the configuration/amplitude of the same maker type in (b).

ing technologies with frequency dependent absorptivity and emissivity, and in signal encoding/modulation applications. This flexibility is enhanced by the tunability and scalability due to variation of static load, and the geometric and material properties. For instance, by reducing the rectifier particle size to $180 \mu m$ (see analytical expressions in Methods), assuming $F_0 = 0.1$ N and the same configuration and ratio m/M as in figures 6.1-6.3, we predict the rectifier has a defect frequency of $f_d \approx 1$ MHz (characteristic of medical ultrasound) and an overall system length of 6.7 mm. As

our proposed method of energy rectification and bistable switching is achieved by a combination of nonlinear dynamics, bifurcations and frequency filtering, it could be generally applicable to different physical settings, including photonic and nanoscale thermal/phononic devices. This could result in new devices for optical/thermal computation (including logic gates, switches, and modulators), energy harvesting, and sensing.

6.8 Methods

6.8.1 Experimental Setup

The stainless steel particles (316 type, with elastic modulus $E = 193$ GPa and Poisson's ratio $\nu = 0.3$) [5] are positioned on two aligned polycarbonate rods. The defect particle is aligned with the axis of the crystal using a polycarbonate ring. We mount the piezoelectric actuator on a steel cube, and place a soft spring ($K_S = 1.24$ kN/m) at the other end. The spring and crystal are compressed, by positioning a second steel cube with respect to the first. The static load is measured with a load cell placed in between the spring and the steel cube. The displacement of the actuator and embedded strain gage are calibrated optically. We utilize sensors consisting of piezoelectric disks embedded between two halves of a spherical particle, constructed so as to preserve the bulk material properties of the sphere [145]. The output of our sensors is conditioned with voltage amplifiers and analog 30 kHz, 8th-order butterworth low-pass filters. The conditioned sensor output is digitally filtered with 300 Hz 5th-order butterworth high-pass filters to remove 60 Hz electrical noise.

6.8.2 Model

We model our system as a chain of nonlinear oscillators [21]:

$$m_n \ddot{u}_n = A_n [\Delta_n + u_{n-1} - u_n]_+^{3/2} - A_{n+1} [\Delta_{n+1} + u_i - u_{i+1}]_+^{3/2} - \frac{m_n}{\tau} \dot{u}_n, \quad (6.1)$$

where $[Y]_+$ denotes the positive part of Y , u_n is the displacement of the n th sphere around the static equilibrium, m_n is the mass of the n th particle, and $\Delta_n = (\frac{F_0}{A_n})^{2/3}$ is the static overlap. The coefficients $A_n = \frac{2E}{3(1-\nu^2)}(\frac{R_{n-1}R_n}{R_{n-1}+R_n})^{1/2}$ are defined by the Hertz law potential between adjacent spheres, where R_n is the radius of the n th particle [21, 84].

We linearize the conservative ($\tau = \infty$) equation (6.1) about the crystal's equilibrium state [137]. The homogenous crystal contains one band of propagating frequencies extending from $f = 0$ to $f_c = \frac{1}{2\pi} \sqrt{\frac{4K_{RR}}{M}}$. We calculate the frequency of the defect mode [116, 144], by considering a reduced three-particle eigensystem, where $f_d = \frac{1}{2\pi} \sqrt{\frac{2K_{Rr}M + K_{RR}m + K_{Rr}m + \sqrt{-8K_{Rr}K_{RR}mM + [2K_{Rr}M + (K_{RR} + K_{Rr})m]^2}}{2mM}}$, and $K_{Rr} = \frac{3}{2}A_{Rr}^{2/3}F_0^{1/3}$.

6.9 Supplementary Information

6.9.1 Experimental Measurement of Linear Spectra

To measure the linear spectrum of the system, we apply broadband noise via the actuator to the granular crystal [5, 144] statically compressed at $F_0 = 8$ N. We calculate the transfer functions, shown in figure 6.5, by dividing the averaged (over 16 runs) PSD of the force-time history measured at each sensor, by the mean (over all runs) PSD amplitude in the acoustic band (1 kHz to f_c). In both panels, the blue (dark grey) curve corresponds to the sensor four sites from the actuator, while the red (light grey) to the sensor furthest from the actuator (at the ‘‘end’’ of the crystal). In the reverse configuration (figure 6.5), frequencies above the acoustic cutoff are attenuated. Because of this, there is insufficient transmitted energy at the defect frequency remaining to excite the defect mode. Alternatively, in the forward configuration (figure 6.5b) the actuator is placed close to the defect and excites the defect mode, as can be seen in the spectrum of the sensor two sites from the defect (blue curve). The localized nature of this mode is revealed, as this peak is not present at the end of the chain (red curve). The frequency peak observed here agrees closely with the analytically predicted defect mode frequency f_d (vertical dashed line).

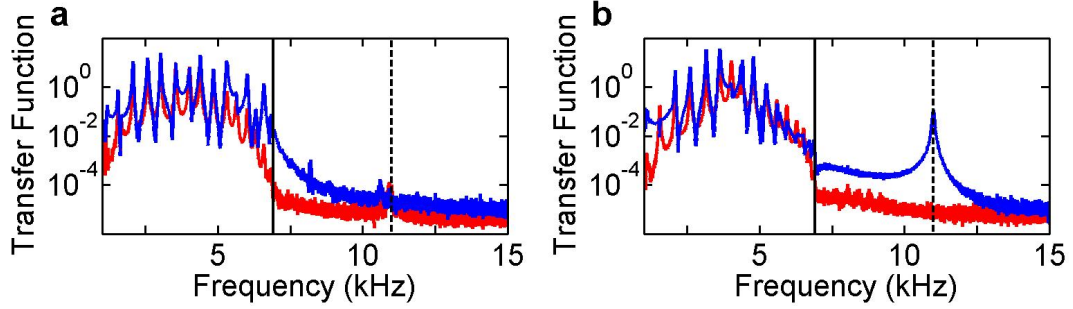


Figure 6.5: Experimentally measured PSD transfer functions. PSD transfer function for the granular crystal rectifiers of figures 6.1-6.4 ($F_0 = 8$ N) in the (a) reverse and (b) forward configurations. Blue (dark grey) curve is the sensor located four particles from the actuator, red (light grey) is the sensor 19 particles from the actuator (corresponding to the sensors of the same color in figure 6.1a,b, respectively). The vertical black line is the acoustic band upper cutoff frequency f_c , and the vertical black dashed line is the defect mode frequency f_d .

6.9.2 Quasiperiodic Vibrations

To understand the fundamental mechanism that leads to quasiperiodic vibrations, we apply the Newton's method in phase space [5] to equation 6.1. This method is utilized for obtaining periodic solutions and their Floquet multipliers λ_j , which can be used to study the linear stability of the solutions. If all $|\lambda_j| < 1$, the periodic solution is stable as small perturbations decay exponentially in time. In figure 6.6a, we show the Floquet spectrum of the periodic solution corresponding to the forward configuration with $F_0 = 8$ N, $\tau = 1.75$ ms, $f_{dr} = 10.5$ kHz, and $\delta_{(+)} = 0.6$ μ m. Here all Floquet multipliers lie on a circle of radius $e^{\frac{-1}{2\tau f_{dr}}}$ except four (two which lie outside the unit circle). Because of these two, the periodic solution corresponding to these parameters is linearly unstable. From a bifurcation point of view, this picture is known as a Naimark-Sacker bifurcation [16]. In this case, the unstable periodic solution decays into a stable two-frequency quasiperiodic solution. In figure 6.6b, we show the time evolution (force-time history of the fourth particle) of the unstable periodic solution of figure 6.6a. We numerically integrate the equations of motion (equation 6.1) using a fourth-order Runge-Kutta scheme with the unstable periodic solution found by Newton's method as the initial condition. After a short transient

period, we see the unstable periodic solution decays into a stable quasiperiodic solution. Multiple frequency peaks based on the linear combinations of two dominant frequencies, characteristic of a quasiperiodic solution, can be seen in the PSD (calculated for times $100 < t < 200$ ms, blue region) shown in figure 6.6c. Similarly, to obtain the quasiperiodic branch of solutions of figure 6.2, we calculate the dynamic force amplitude by using the unstable periodic solution of the same driving amplitude as an initial condition for the numerical integrator. Here we integrate for 50 ms and take the maximum amplitude from 40 to 50 ms.

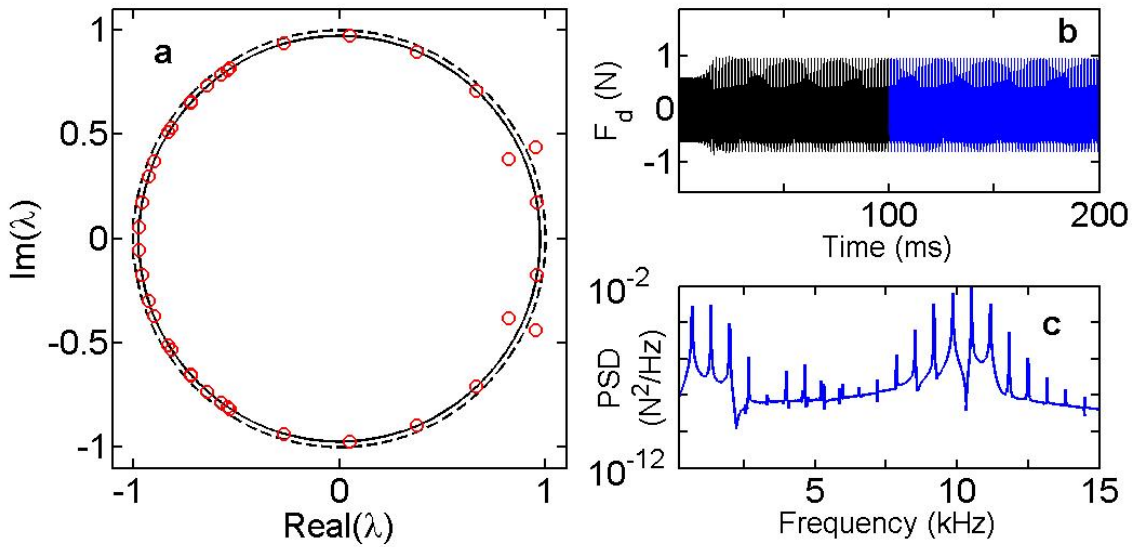


Figure 6.6: Quasiperiodic vibrations. (a) Floquet spectrum of the periodic solution corresponding to $f_{dr} = 10.5$ kHz and $\delta_{(+)} = 0.6 \mu\text{m}$. (b) Numerically calculated force-time history of the fourth particle away from the actuator in the forward configuration, using as an initial condition the periodic solution of panel (a). (c) PSD of the blue (dark grey) time region of panel (b).

6.9.3 Route to Chaos

In this section, we study the transition of the system from quasiperiodic to chaotic dynamics. Using the same method as described for figure 6.6, we take the PSD of the force-time history (four particles from the actuator, forward configuration, $100 < t < 200$ ms) of the time integrated solution using the unstable periodic solutions

found by Newton's method, at increasing amplitudes, as the initial conditions. For the smallest amplitude $\delta_{(+)} = 0.60 \mu\text{m}$ we observe a quasiperiodic solution (figure 6.7a) with a discrete set of frequencies based on the linear combinations of f_{dr} and f_N . As we increase the amplitude ($\delta_{(+)} = 1.0 \mu\text{m}$, figure S3b), we observe the appearance of additional peaks at frequencies based on linear combinations of $f_{dr}/2$ and $f_N/2$, which is a sign of double period bifurcation. Increasing the amplitude further ($\delta_{(+)} = 1.03 \mu\text{m}$, figure 6.7c) we see peaks based on $f_{dr}/4$ and $f_N/4$ (second double period bifurcation). Further increasing the amplitude, a continued cascade of double period bifurcations results in the merging of distinct frequency peaks and the formation of continuous bands, as shown in figure 6.7d.

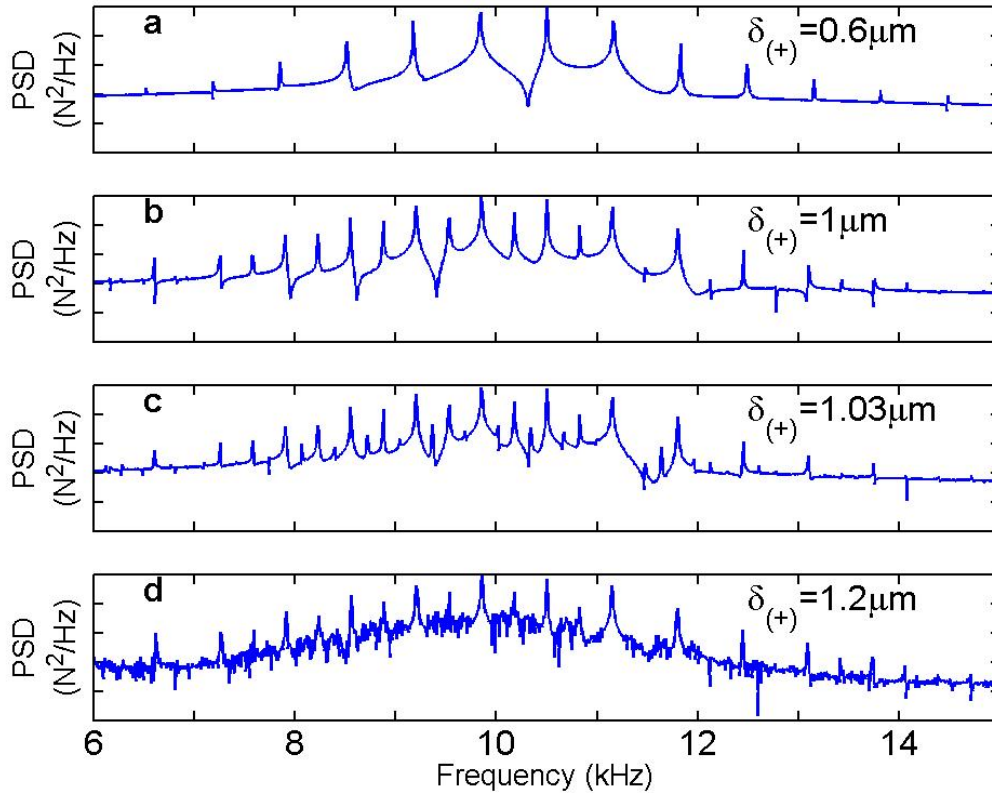


Figure 6.7: The period doubling cascade route to chaos. PSD of the numerically calculated force-time history, corresponding to driving amplitudes $\delta_{(+)} = 0.6 \mu\text{m}$ (a), $\delta_{(+)} = 1 \mu\text{m}$ (b), $\delta_{(+)} = 1.03 \mu\text{m}$ (c) and $\delta_{(+)} = 1.2 \mu\text{m}$ (d) for the fourth particle from the actuator in the forward configuration.

6.9.4 Logic

By configuring the tunable frequency mechanical rectifiers to have multiple inputs, we propose tunable frequency logic devices. We present concepts for two types of logic devices, the AND gate (figure 6.8a) and the OR gate (figure 6.8b). We assume incident harmonic signals from A and B are in phase. For the AND gate, a large signal will pass only if the sum of the signals from A and B are greater than the critical amplitude δ_c where the jump phenomenon occurs. Otherwise, if either A or B is off, the signal will be attenuated and not pass. This configuration can also be used in bifurcation based sensors. For instance, if the signal from A is set near the critical jump phenomena amplitude, a small deviation in B will result in the transmission of a large signal. For the OR gate, a rectifier is placed in each of the A and B branches. If the signal coming from each respective branch is greater than the critical amplitude, this signal will pass and combine with the other signal. Thus a large amplitude signal will pass in all cases except when there is no large signal coming from either A or B.

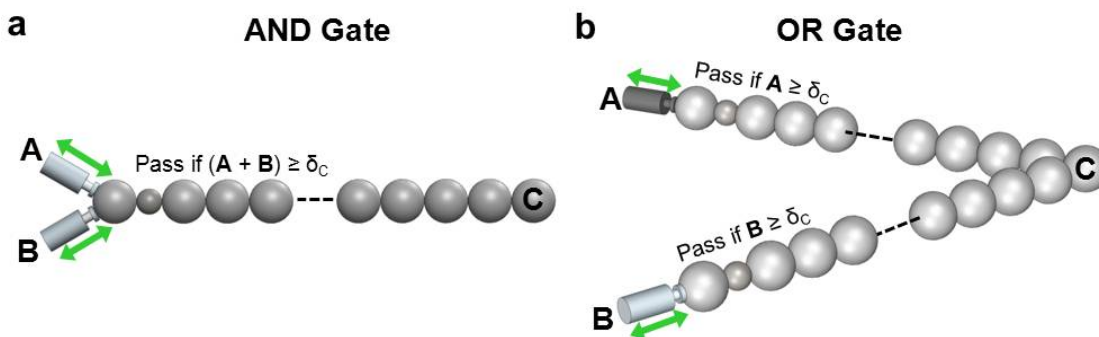


Figure 6.8: Mechanical logic devices based on the tunable rectifier. Incident signals are applied through A and B, and received in C. (a) AND gate. Signals will only pass when combined amplitudes of A and B are greater than the critical rectifier amplitude δ_c . (b) OR gate. Signals will pass when either the amplitude of A or B are greater than the critical rectifier amplitude.

6.10 Author Contributions

This chapter is based on [149]. N.B. and G.T. developed the system concept. N.B. led the experimental work. G.T. led the theoretical and numerical analysis. C.D. provided guidance and contributed to the design and analysis throughout the project. All authors contributed to the writing and editing of the manuscript.

Chapter 7

Conclusion

This thesis described several new ways to control mechanical wave energy utilizing the discreteness and nonlinearity of granular crystals. We focused on one-dimensional (1D) statically compressed granular crystals composed of macroscopic spheres (or cylinders) of up to two particle types (diatomic). This included new ways to engineer the dispersion relation of granular crystals to provide more tunable vibration filtering capabilities, localize energy for energy harvesting applications, and create direction dependent energy flows for energy harvesting, sensing, and logic devices.

In chapter 2 we described the tunable vibration filtering properties of statically compressed 1D granular crystals with of three-particle unit cells composed of elastic beads and cylinders. Tunability of the frequency ranges supported by the crystal were shown with variation of the static load and cylinder mass. We measured the transfer functions of the crystals using state-space analysis and experiments, and we compared the results with the corresponding theoretical dispersion relations. Up to three distinct pass bands and three (two finite) band gaps were shown to exist for selected particle configurations.

We described the discovery and characterization of discrete breathers in occurring 1D granular crystals in chapter 3 and 4. Using theory, simulations, and experiments, we demonstrated the formation of discrete breathers via modulational instability, and provided clear experimental proof of their existence. We followed this demonstration, with a systematic analysis of two discrete breather families that diatomic granular crystals can support in the gap of its linear spectrum. We explored the progressive

localization of the solutions upon decreasing the frequency within the gap, and we discussed the regimes of weak, moderate, and strong discreteness at length. We showed a unique spatial profile of discrete breathers with strong discreteness, and their similarity to linear gap surface modes.

In chapter 5 we studied the response of statically compressed granular crystals containing light-mass defects, and characterized their near-linear spectra by applying continuous excitation. We demonstrated that such chains support localized modes with frequencies above that of their acoustic band cutoff, using approximate few-bead analytical calculations, numerics, and experiments. The number of supported localized modes depends on the number of defects, while their frequencies depend on the inter-defect distance, on the ratio $\frac{m}{M}$ of defect to regular masses (and the geometric/elastic properties of the beads), and on the static load. We also briefly described the nonlinear generalizations of such modes, departing from the near-linear regime, and showed a downshift of the corresponding defect mode frequencies with increasing amplitude.

In chapter 6 we proposed and demonstrated a new mechanism for tunable rectification that utilizes bifurcations and chaos. This mechanism has a sharp transition between states, which can lead to phononic switching, sensing, and can be used in logic devices. It also redistributes the input energy to lower frequencies, which can lead to more flexible energy harvesting and signal processing. We presented the first experimental demonstration of this mechanism, in a granular crystal composed of a statically compressed one-dimensional array of particles in contact, containing a light mass defect near a boundary. These systems are nonlinear and contain tunable pass and stop bands in their dispersion relation. Because of the defect, vibrations at selected frequencies cause bifurcations and a subsequent jump to quasiperiodic and chaotic states with broadband frequency content. We used this combination of frequency filtering and asymmetrically excited bifurcations to obtain rectification. We calculated rectification ratios greater than 10^4 , and investigated the system scalability and tunability using analytical and numerical approaches.

The discovery and characterization of such phenomena will aid in the develop-

ment of practical granular crystal-based devices, for use in vibration filtering and energy harvesting applications. Additionally, the ideas explored here for this setting could in the future be applied to more complex settings (higher degree of freedom granular crystals, other discrete nonlinear systems) and systems of different length scales. Because nonlinearity and discreteness are common elements to many dynamical systems, we also foresee that the phenomena described generally applied to other discrete-nonlinear systems.

Bibliography

- [1] R. Martinez-Sala, J. Sancho, J. Gomez, J. Llinares, and F. Mesegeur, “Sound attenuation by sculpture,” *Nature*, vol. 378, no. 241, p. 241, 1995.
- [2] N. Gomopoulos, D. Maschke, C. Y. Koh, E. L. Thomas, W. Tremel, H. J. Butt, and G. Fytas, “One-dimensional hypersonic phononic crystals,” *Nano Lett.*, vol. 10, no. 3, pp. 980–984, 2010.
- [3] *Metals Handbook, 10th Edition*. Materials Park, OH: ASM International, 1990.
- [4] D. R. Christman, W. M. Isbell, S. G. Babcock, A. R. McMillan, and S. J. Green, *Measurements of Dynamic Properties of Materials, Volume 3: 6061-T6 Aluminum*. Warren, MI: General Motors Technical Center, Materials and Structures Lab, 1971.
- [5] N. Boechler, G. Theocharis, S. Job, P. G. Kevrekidis, M. A. Porter, and C. Daraio, “Discrete breathers in one-dimensional diatomic granular crystals,” *Phys. Rev. Lett.*, vol. 104, no. 244302, 2010.
- [6] T. Gorishnyy, M. Maldovan, C. Ullal, and E. Thomas, “Sound ideas,” *Phys. World*, vol. 18, no. 12, pp. 24–29, 2005.
- [7] P. Hess, “Surface acoustic waves in materials science,” *Phys. Today*, vol. 55, no. 3, pp. 42–47, 2002.
- [8] C. Harris, *Shock and Vibration Handbook, Third Edition*. New York, NY: McGraw-Hill, 1988.

- [9] K. Ogata, *System Dynamics, Fourth Edition*. Upper Saddle River, NJ: Prentice Hall, 2004.
- [10] C. Kittel, *Introduction to Solid State Physics*. New York, NY: John Wiley & Sons, 2005.
- [11] F. Incropera and D. P. Dewitt, *Fundamentals of Heat and Mass Transfer, Fifth Edition*. New York, NY: John Wiley & Sons, 2002.
- [12] L. Brillouin, *Wave Propagation in Periodic Structures*. New York, NY: Dover, 1953.
- [13] F. Duan and J. Guojin, *Introduction to Condensed Matter Physics: Volume 1*. Hackensack, NJ: World Scientific Publishing Company, 2005.
- [14] M. Maldovin and E. L. Thomas, *Periodic Materials and Interference Lithography for Photonics, Phononics and Mechanics*. Weinheim, Germany: Wiley-VCH, 2009.
- [15] S. H. Strogatz, *Nonlinear Dynamics and Chaos*. Cambridge, MA: Perseus Publishing, 1994.
- [16] S. Wiggins, *Introduction to Applied Nonlinear Dynamical Systems and Chaos, Second Edition*. New York, NY: Springer, 2000.
- [17] R. B. Karabalin, R. Lifshitz, M. C. Cross, M. H. Matheny, S. C. Masmanidis, and M. L. Roukes, “Signal amplification by sensitive control of bifurcation topology,” *Phys. Rev. Lett.*, vol. 106, no. 094102, 2011.
- [18] R. Vijay, M. H. Devoret, and I. Siddiqi, “Invited review article: The josephson bifurcation amplifier,” *Rev. Sci. Instrum.*, vol. 80, no. 111101, 2009.
- [19] D. K. Campbell, S. Flach, and Y. S. Kivshar, “Localizing energy through nonlinearity and discreteness,” *Phys. Today*, vol. 57, no. 1, pp. 43–49, 2004.

- [20] M. Soljačić and J. D. Joannopoulos, “Enhancement of nonlinear effects using photonic crystals,” *Nature*, vol. 3, no. 211, 2004.
- [21] V. F. Nesterenko, *Dynamics of Heterogeneous Materials*. New York, NY: Springer, 2001.
- [22] C. Daraio, V. F. Nesterenko, E. B. Herbold, and S. Jin, “Tunability of solitary wave properties in one-dimensional strongly nonlinear phononic crystals,” *Phys. Rev. E.*, vol. 73, no. 026610, 2006.
- [23] Y. C. Fung and P. Tong, *Classical and Computational Solid Mechanics*. Singapore: World Scientific, 2001.
- [24] G. B. Whitham, *Linear and Nonlinear Waves*. New York, NY: John Wiley and Sons, Inc., 1999.
- [25] J. S. Russel, “Report on waves,” *Report of the 14th Meeting of the British Association for the Advancement of Science*, no. 311, 1844.
- [26] I. Newton, *Principia, Book II*. 1686.
- [27] A. M. Kosevich, *The Crystal Lattice: Phonons, Solitons, Dislocations, Superlattices, Second Edition*. Weinheim, Germany: Wiley-VCH, 2005.
- [28] P. Markos and C. M. Soukoulis, *Wave Propagation: From Electrons to Photonic Crystals and Left-Handed Materials*. Princeton, NJ: Princeton University Press, 2008.
- [29] E. Yablonovitch, “Photonic crystals: Semiconductors of light,” *Scientific American*, vol. 285, no. 6, 2001.
- [30] J. D. Joannopoulos, R. D. Meade, and J. N. Winn, *Photonic Crystals: Molding the Flow of Light*. Princeton, NJ: Princeton University Press, 1995.
- [31] M. Brongersma and P. G. Kik, *Surface Plasmon Nanophotonics*. The Netherlands: Springer, 2007.

- [32] C. W. Robinson and G. W. Leppelmeier, “Experimental verification of dispersion relations for layered composites,” *J. Appl. Mech.*, vol. 41, no. 89, 1974.
- [33] V. K. Kinra and E. L. Ker, “An experimental investigation of pass bands and stop bands in two periodic particulate composites,” *Int. J. Solids Structures*, vol. 19, no. 5, 1983.
- [34] E. H. Lee and W. H. Yang, “On waves in composite materials with periodic structure,” *SIAM Journal on Applied Mathematics*, vol. 25, no. 3, 1973.
- [35] A. Bedford, D. S. Drumheiler, and H. J. Sutherland, “On modeling the dynamics of composite materials,” *Mechanics Today*, vol. 3, no. 1-54, 1976.
- [36] Y. Kivshar and G. Agrawal, *Optical Solitons: From Fibers to Photonic Crystals*. San Diego, CA: Academic Press, 2003.
- [37] M. S. Kushwaha, P. Halevi, L. Dobrzynski, and B. Djafari-Rouhani, “Acoustic band structure of periodic elastic composites,” *Phys. Rev. Lett.*, vol. 71, no. 2022, 1993.
- [38] M. M. Sigalas and E. N. Economou, “Elastic and acoustic wave band structure,” *Journal of Sound and Vibration*, vol. 158, no. 2, 1992.
- [39] M. M. Sigalas and E. N. Economou, “Band-structure of elastic waves in 2-dimensional systems,” *Solid State Commun.*, vol. 86, no. 141, 1993.
- [40] M. Sigalas, M. Kushwaha, E. Economou, M. Kafesaki, I. Psarobas, and W. Steurer, “Classical vibrational modes in phononic lattices: Theory and experiment,” *Zeitschrift für Kristallographie*, vol. 220, pp. 765–809, 2005.
- [41] Z. Liu, X. Zhang, Y. Mao, Y. Y. Zhu, Z. Yang, C. T. Chan, and P. Sheng, “Locally resonant sonic materials,” *Science*, vol. 289, no. 1734, 2000.
- [42] W. Cheng, J. Wang, U. Jonas, G. Fytas, and N. Stefanou, “Observation and tuning of hypersonic band gaps in colloidal crystals,” *Nature Materials*, vol. 5, no. 830, 2006.

- [43] L. Fok, M. Ambati, and X. Zhang, “Acoustic metamaterials,” *MRS Bulletin*, vol. 33, pp. 931–934, 2008.
- [44] J. S. Jensen, “Phononic band gaps and vibrations in one- and two-dimensional mass-spring structures,” *Journal of Sound and Vibration*, vol. 266, no. 1053, 2003.
- [45] B. Liang, X. S. Guo, J. Tu, D. Zhang, and J. C. Cheng, “An acoustic rectifier,” *Nature Mater.*, vol. 9, no. 989, 2010.
- [46] H. Y. Hao and H. J. Maris, “Experiments with acoustic solitons in crystalline solids,” *Phys. Rev. B*, vol. 64, no. 064302, 2001.
- [47] P. Hess and A. M. Lomonosov, “Solitary surface acoustic waves and bulk solitons in nanosecond and picosecond laser ultrasonics,” *Ultrasonics*, vol. 50, no. 167, 2010.
- [48] P. G. Kevrekidis, “Non-linear waves in lattices: Past, present, future,” *IMA Journal of Applied Mathematics*, no. 1-35, 2011.
- [49] E. Fermi, J. Pasta, and S. Ulam, “Studies of nonlinear problems,” *LASL Report LA-1940*, 1955.
- [50] M. Porter, N. Zabusky, B. Hu, and D. Campbell, “Fermi, Pasta, Ulam and the birth of experimental mathematics,” *American Scientist*, vol. 97, no. 6, 2009.
- [51] S. Flach and A. V. Gorbach, “Discrete breathers—advances in theory and applications,” *Phys. Rep.*, vol. 467, no. 1, pp. 1–116, 2008.
- [52] S. Sen, J. Hong, J. Bang, E. Avalos, and R. Doney, “Solitary waves in the granular chain,” *Phys. Rep.*, vol. 462, no. 21, 2008.
- [53] S. Flach and C. R. Willis, “Discrete breathers,” *Phys. Rep.*, vol. 295, no. 5, pp. 181–264, 1998.

- [54] S. Aubry, “Breathers in nonlinear lattices: Existence, linear stability and quantization,” *Physica D*, vol. 103, no. 1-4, pp. 201–250, 1997.
- [55] R. S. MacKay, “Discrete breathers: Classical and quantum,” *Physica A*, vol. 288, no. 1-4, pp. 174–198, 2000.
- [56] A. J. Sievers and S. Takeno, “Intrinsic localized modes in anharmonic crystals,” *Phys. Rev. Lett.*, vol. 61, no. 970, 1988.
- [57] J. B. Page, “Asymptotic solutions for localized vibrational modes in strongly anharmonic periodic systems,” *Phys. Rev. B*, vol. 41, no. 7835, 1990.
- [58] R. S. MacKay and S. Aubry, “Proof of existence of breathers for time-reversible or hamiltonian networks of weakly coupled oscillators,” *Nonlinearity*, vol. 7, no. 1623, 1994.
- [59] B. I. Swanson, J. A. Brozik, S. P. Love, G. F. Strouse, and A. P. Shreve, “Observation of intrinsically localized modes in a discrete low-dimensional material,” *Phys. Rev. Lett.*, vol. 82, no. 3288, 1999.
- [60] U. T. Schwarz, L. Q. English, and A. J. Sievers, “Experimental generation and observation of intrinsic localized spin wave modes in an antiferromagnet,” *Phys. Rev. Lett.*, vol. 83, no. 223, 1999.
- [61] E. Trias, J. J. Mazo, and T. P. Orlando, “Discrete breathers in nonlinear lattices: Experimental detection in a Josephson array,” *Phys. Rev. Lett.*, vol. 84, no. 741, 2000.
- [62] P. Binder, D. Abraimov, A. V. Ustinov, S. Flach, and Y. Zolotaryuk, “Observation of breathers in Josephson ladders,” *Phys. Rev. Lett.*, vol. 84, no. 745, 2000.
- [63] A. Xie, W. Hoff, and R. H. Austin, “Long-lived amide I vibrational modes in myoglobin,” *Phys. Rev. Lett.*, vol. 84, no. 5435, 2000.

- [64] M. Peyrard, “Nonlinear dynamics and statistical physics of DNA,” *Phys. Rev. Lett.*, vol. 17, no. R1, 2004.
- [65] M. Sato, B. E. Hubbard, and A. J. Sievers, “Colloquium: Nonlinear energy localization and its manipulation in micromechanical oscillator arrays,” *Rev. Mod. Phys.*, vol. 78, no. 137, 2006.
- [66] A. H. Nayfeh and D. T. Mook, *Nonlinear Oscillations*. New York, NY: John Wiley and Sons, Inc., 1995.
- [67] P. W. Anderson, “Absence of diffusion in certain random lattices,” *Phys. Rev.*, vol. 109, no. 5, 1958.
- [68] A. A. Maradudin, E. W. Montroll, and G. H. Weiss, *Theory of Lattice Dynamics in the Harmonic Approximation*. New York: Academic, 1963.
- [69] G. Lucovsky, M. Brodsky, and E. Burstein, “Extension of a linear diatomic-chain model for the calculation of local-mode frequencies in real crystals,” *Phys. Rev. B*, vol. 2, no. 3295, 1970.
- [70] A. F. Andreev, “Exotic superconductivity of the twinning planes,” *JETP Lett.*, vol. 46, no. 584, 1987.
- [71] A. V. Balatsky, “From obscurity to impurity,” *Nature*, vol. 403, no. 717, 2000.
- [72] M. I. Molina and G. P. Tsironis, “Nonlinear impurities in a linear chain,” *Phys. Rev. B*, vol. 47, no. 15330, 1993.
- [73] G. P. Tsironis, M. I. Molina, and D. Hennig, “Generalized nonlinear impurity in a linear chain,” *Phys. Rev. E*, vol. 50, no. 2365, 1994.
- [74] S. Y. Jin, E. Chow, V. Hietala, P. R. Villeneuve, and J. D. Joannopoulos, “Experimental demonstration of guiding and bending of electromagnetic waves in a photonic crystal,” *Science*, vol. 282, no. 274, 1998.

- [75] M. G. Khazhinsky and A. R. McGurn, “Green’s function method for waveguide and single impurity modes in 2D photonic crystals: H-polarization,” *Phys. Lett. A*, vol. 237, no. 175, 1998.
- [76] U. Peschel, R. Morandotti, J. S. Aitchison, H. S. Eisenberg, and Y. Silberberg, “Nonlinearly induced escape from a defect state in waveguide arrays,” *Appl. Phys. Lett.*, vol. 75, no. 1348, 1999.
- [77] R. Morandotti, H. S. Eisenberg, D. Mandelik, Y. Silberberg, D. Modotto, M. Sorel, C. R. Stanley, and J. S. Aitchison, “Interactions of discrete solitons with structural defects,” *Opt. Lett.*, vol. 28, no. 834, 2003.
- [78] E. Smirnov, C. E. Rüter, M. Stepić, V. Shandarov, and D. Kip, “Dark and bright blocker soliton interaction in defocusing waveguide arrays,” *Opt. Express*, vol. 14, no. 11248, 2006.
- [79] E. Lidorikis, K. Busch, Q. Li, C. T. Chan, and C. M. Soukoulis, “Optical nonlinear response of a single nonlinear dielectric layer sandwiched between two linear dielectric structures,” *Phys. Rev. B*, vol. 56, no. 15090, 1997.
- [80] M. Sato, B. Hubbard, A. Sievers, B. Ilic, and H. Craighead, “Optical manipulation of intrinsic localized vibrational energy in cantilever arrays,” *Europhys. Lett.*, vol. 66, no. 318, 2004.
- [81] P. Engels and C. Atherton, “Stationary and nonstationary fluid flow of a Bose-Einstein condensate through a penetrable barrier,” *Phys. Rev. Lett.*, vol. 99, no. 160405, 2007.
- [82] T. Neely, E. Samson, A. Bradley, M. Davis, and B. Anderson, “Observation of vortex dipoles in an oblate Bose-Einstein condensate,” *Phys. Rev. Lett.*, vol. 104, no. 160401, 2010.
- [83] H. Hertz, “On the contact of elastic solids,” *J. reine angew. Math*, vol. 92, no. 156, 1881.

- [84] K. L. Johnson, *Contact Mechanics*. Cambridge, UK: Cambridge University Press, 1985.
- [85] H. M. Jaeger, S. R. Nagel, and R. P. Behringer, “The physics of granular materials,” *Phys. Today*, vol. 49, no. 4, 1996.
- [86] V. F. Nesterenko, “Propagation of nonlinear compression pulses in granular media,” *JAMTP*, vol. 24, no. 5, pp. 733–734, 1983.
- [87] A. N. Lazaridi and V. F. Nesterenko, “Observation of a new type of solitary waves in a one-dimensional granular medium,” *JAMTP*, vol. 26, no. 3, pp. 405–408, 1985.
- [88] A. Chatterjee, “Asymptotic solution for solitary waves in a chain of elastic spheres,” *Phys. Rev. E*, vol. 59, no. 5, 1999.
- [89] G. Friesecke and J. Wattis, “Existence theorem for solitary waves on lattices,” *Commun. Math. Phys.*, vol. 161, no. 391, 1994.
- [90] J. Y. Ji and J. Hong, “Existence criterion of solitary waves in a chain of grains,” *Phys. Lett. A*, vol. 260, no. 60, 1999.
- [91] R. S. MacKay, “Solitary waves in a chain of beads under hertz contact,” *Phys. Lett. A*, vol. 251, no. 191, 1999.
- [92] A. Shuckla, C. Y. Zhu, and M. H. Sadd, “Angular dependence of dynamic load transfer due to explosive loading in granular aggregate chains,” *Journal of Strain Analysis*, vol. 23, no. 3, 1988.
- [93] A. Shuckla, M. H. Sadd, Y. Xu, and Q. M. Tai, “Influence of loading pulse duration on dynamic load transfer in a simulated granular medium,” *J. Mech. Phys. Solids*, vol. 41, no. 11, 1993.
- [94] Y. Zhu, A. Shuckla, and M. H. Sadd, “The effect of microstructural fabric on dyanmic load transfer in two dimensional assemblies of elliptical particles,” *J. Mech. Phys. Solids*, vol. 44, no. 8, 1996.

- [95] Y. Zhu, F. Sienkiewicz, A. Shuckla, and M. H. Sadd, "Propagation of explosive pulses in assemblies of disks and spheres," *Journal of Engineering Mechanics*, vol. 123, no. 10, 1997.
- [96] M. Manciu, S. Sen, and A. J. Hurd, "Crossing of identical solitary waves in a chain of elastic beads," *Phys. Rev. E*, vol. 63, no. 016614, 2000.
- [97] M. Manciu, S. Sen, and A. J. Hurd, "The propagation and backscattering of soliton-like pulses in a chain of quartz beads and related problems. (I). Propagation," *Physica A*, vol. 274, no. 588, 1999.
- [98] S. Sen, M. Manciu, and J. D. Wright, "Solitonlike pulses in perturbed and driven hertzian chains and their possible applications in detecting buried impurities," *Phys. Rev. E*, vol. 57, no. 2386, 1998.
- [99] R. Doney and S. Sen, "Decorated, tapered, and highly nonlinear granular chain," *Phys. Rev. Lett.*, vol. 97, no. 155502, 2006.
- [100] J. Hong, "Universal power-law decay of the impulse energy in granular protectors," *Phys. Rev. Lett.*, vol. 94, no. 108001, 2005.
- [101] S. Sen and T. R. Mohan, "Dynamics of metastable breathers in nonlinear chains in acoustic vacuum," *Phys. Rev. E*, vol. 79, no. 036603, 2009.
- [102] C. Coste, E. Falcon, and S. Fauve, "Solitary waves in a chain of beads under hertz contact," *Phys. Rev. E*, vol. 56, no. 6104, 1997.
- [103] C. Coste and B. Gilles, "On the validity of hertz contact law for granular material acoustics," *Eur. Phys. J. B*, vol. 7, no. 155, 1999.
- [104] B. Gilles and C. Coste, "Low-frequency behavior of beads constrained on a lattice," *Phys. Rev. Lett.*, vol. 90, no. 17, 2003.
- [105] C. Coste and B. Gilles, "Sound propagation in a constrained lattice of beads: High-frequency behavior and dispersion relation," *Phys. Rev. E*, vol. 77, no. 021302, 2008.

- [106] A. Merkel, V. Tournat, and V. Gusev, “Elastic waves in noncohesive frictionless granular crystals,” *Ultrasonics*, vol. 50, no. 133, 2010.
- [107] V. Tournat, B. Castagnède, V. Gusev, and P. Biquin, “Self-demodulation acoustic signatures for nonlinear propagation in glass beads,” *C. R. Mécanique*, vol. 331, no. 119, 2003.
- [108] A. C. Hladky-Hennion and M. de Billy, “Experimental validation of band gaps and localization in a one-dimensional diatomic phononic crystal,” *J. Acoust. Soc. Am.*, vol. 122, no. 2594, 2007.
- [109] A. C. Hladky-Hennion, G. Allan, and M. de Billy, “Localized modes in a one-dimensional diatomic chain of coupled spheres,” *J. Appl. Phys.*, vol. 98, no. 054909, 2005.
- [110] M. de Billy, “Experimental study of sound propagation in a chain of spherical beads,” *J. Acoust. Soc. Am.*, vol. 108, no. 1486, 2000.
- [111] A. C. Hladky-Hennion, F. Cohen-Tenoudji, A. Devos, and M. de Billy, “On the existence of subresonance generated in a one-dimensional chain of identical spheres,” *J. Acoust. Soc. Am.*, vol. 112, no. 054850, 2002.
- [112] A. C. Hladky-Hennion, J. Vasseur, B. Djafari-Rouhani, and M. de Billy, “Sonic band gaps in one-dimensional phononic crystals with a symmetric stub,” *Phys. Rev. B*, vol. 77, no. 104304, 2008.
- [113] A. C. Hladky-Hennion, C. Granger, and J. Vasseur, “Propagation of elastic waves in one-dimensional periodic stubbed waveguides,” *Phys. Rev. B*, vol. 82, no. 104307, 2010.
- [114] F. J. Sierra-Valdez, F. Pacheco-Vázquez, O. Carvente, F. Malloggi, J. Cruz-Damas, R. Rechtman, and J. C. Ruiz-Surez, “Acoustic gaps in a chain of magnetic spheres,” *Phys. Rev. E*, vol. 81, no. 011301, 2010.

- [115] F. Melo, S. Job, F. Santibanez, and F. Tapia, “Experimental evidence of shock mitigation in a hertzian tapered chain,” *Phys. Rev. E*, vol. 73, no. 041305, 2006.
- [116] S. Job, F. Melo, A. Sokolow, and S. Sen, “How hertzian solitary waves interact with boundaries in a 1D granular medium,” *Phys. Rev. Lett.*, vol. 94, no. 178002, 2005.
- [117] S. Job, F. Santibanez, F. Tapia, and F. Melo, “Nonlinear waves in dry and wet hertzian granular chains,” *Ultrasonics*, vol. 48, no. 506, 2008.
- [118] S. Job, F. Santibanez, F. Tapia, and F. Melo, “Wave localization in strongly nonlinear hertzian chains with mass defect,” *Phys. Rev. E*, vol. 80, no. 025602(R), 2009.
- [119] E. Hascoet and H. J. Hermann, “Shocks in non-loaded bead chains with impurities,” *Eur. Phys. J. B*, vol. 14, no. 183, 2000.
- [120] A. Rosas and K. Lindenberg, “Pulse dynamics in a chain of granules with friction,” *Phys. Rev. E*, vol. 68, no. 041304, 2003.
- [121] A. Rosas, A. Romero, V. F. Nesterenko, and K. Lindenberg, “Observation of two-wave structure in strongly nonlinear dissipative granular chains,” *Phys. Rev. Lett.*, vol. 98, no. 164301, 2007.
- [122] A. Rosas and K. Lindenberg, “Pulse velocity in a granular chain,” *Phys. Rev. E*, vol. 69, no. 037601, 2004.
- [123] U. Harbola, A. Rosas, M. Esposito, and K. Lindenberg, “Pulse propagation in tapered granular chains: An analytic study,” *Phys. Rev. E*, vol. 80, no. 031303, 2009.
- [124] U. Harbola, A. Rosas, A. H. Romero, and K. Lindenberg, “Pulse propagation in randomly decorated chains,” *Phys. Rev. E*, vol. 82, no. 011306, 2010.

- [125] Y. Starosvetsky and A. Vakakis, “Traveling waves and localized modes in one-dimensional homogeneous granular chains with no pre-compression,” *Physical Review E*, vol. 82, no. 026603, 2010.
- [126] K. R. Jayaprakash, Y. Starosvetsky, A. Vakakis, M. Peeters, and G. Kerschen, “Nonlinear normal modes and band gaps in granular chains with no pre-compression,” *Nonlinear Dynamics*, 2010.
- [127] V. F. Nesterenko, C. Daraio, E. B. Herbold, and S. Jin, “Anomalous wave reflection at the interface of two strongly nonlinear granular media,” *Phys. Rev. Lett.*, vol. 95, no. 158702, 2005.
- [128] C. Daraio, V. F. Nesterenko, E. B. Herbold, and S. Jin, “Strongly nonlinear waves in a chain of teflon beads,” *Phys. Rev. E*, vol. 72, no. 016603, 2005.
- [129] C. Daraio and V. F. Nesterenko, “Strongly nonlinear waves in a chain of polymer coated beads,” *Phys. Rev. E*, vol. 73, no. 026612, 2006.
- [130] M. A. Porter, C. Daraio, E. B. Herbold, I. Szelengowicz, and P. G. Kevrekidis, “Highly nonlinear solitary waves in periodic dimer granular chains,” *Phys. Rev. E*, vol. 77, no. 015601(R), 2008.
- [131] M. A. Porter, C. Daraio, I. Szelengowicz, E. B. Herbold, and P. G. Kevrekidis, “Highly nonlinear solitary waves in heterogeneous periodic granular media,” *Physica D*, vol. 238, no. 666, 2009.
- [132] L. Ponson, N. Boechler, Y. M. Lai, M. A. Porter, P. G. Kevrekidis, and C. Daraio, “Nonlinear waves in disordered diatomic granular chains,” *Phys. Rev. E*, vol. 82, no. 021301, 2010.
- [133] R. Carretero-González, D. Khatri, M. Porter, P. Kevrekidis, and C. Daraio, “Dissipative solitary waves in granular crystals,” *Phys. Rev. Lett.*, vol. 102, no. 024102, 2009.

- [134] A. Molinari and C. Daraio, “Stationary shocks in periodic highly nonlinear granular chains,” *Phys. Rev. E*, vol. 80, no. 056602, 2009.
- [135] C. Daraio, D. Ngo, V. F. Nesterenko, and F. Fraternali, “Highly nonlinear pulse splitting and recombination in a two dimensional granular network,” *Phys. Rev. E*, vol. 82, no. 036603, 2010.
- [136] G. Theocharis, M. Kavousanakis, P. G. Kevrekidis, C. Daraio, M. A. Porter, and I. G. Kevrekidis, “Localized breathing modes in granular crystals with defects,” *Phys. Rev. E*, vol. 80, no. 066601, 2009.
- [137] E. B. Herbold, J. Kim, V. Nesterenko, S. Wang, and C. Daraio, “Pulse propagation in a linear and nonlinear diatomic periodic chain: effects of acoustic frequency band-gap,” *Acta Mechanica*, vol. 205, no. 85, 2009.
- [138] C. Daraio, V. F. Nesterenko, E. B. Herbold, and S. Jin, “Energy trapping and shock disintegration in a composite granular medium,” *Phys. Rev. Lett.*, vol. 96, no. 058002, 2006.
- [139] F. Fraternali, M. A. Porter, and C. Daraio, “Optimal design of composite granular protectors,” *Mech. Adv. Mat. Struct.*, vol. 17, no. 1, 2010.
- [140] D. Khatri, C. Daraio, and P. Rizzo, “Coupling of highly nonlinear waves with linear elastic media,” *Proc. SPIE*, vol. 6934, no. 69340U, 2008.
- [141] A. Spadoni and C. Daraio, “Generation and control of sound bullets with a nonlinear acoustic lens,” *Proc. Natl. Acad. Sci. USA*, vol. 107, no. 7230, 2010.
- [142] G. Huang and B. Hu, “Asymmetric gap soliton modes in diatomic lattices with cubic and quartic nonlinearity,” *Phys. Rev. B*, vol. 57, no. 5746, 1998.
- [143] N. Boechler, J. Yang, G. Theocharis, P. G. Kevrekidis, and C. Daraio, “Tunable vibrational band gaps in diatomic granular crystals with a three particle unit cell (in press),” *J. Appl. Phys.*, vol. 109, no. 074906, 2011.

- [144] N. Boechler, G. Theocharis, Y. Man, P. G. Kevrekidis, and C. Daraio, “Defect modes in one-dimensional granular crystals,” *arXiv*, no. 1103.2483, 2011.
- [145] V. F. Nesterenko, A. N. Lazaridi, and E. B. Sibiriyakov, “The decay of soliton at the contact of two “acoustic vacuums”,” *J. Appl. Mech. Tech. Phys.*, vol. 36, no. 166, 1995.
- [146] L. Pickelmann, “Piezomechanik gmbh,” 2011.
- [147] A. Oppenheim and R. Schaffer, *Discrete-Time Signal Processing*. Englewood Cliffs, NJ: Prentice-Hall, 1989.
- [148] G. Theocharis, N. Boechler, P. G. Kevrekidis, S. Job, M. A. Porter, , and C. Daraio, “Intrinsic energy localization through discrete gap breathers in one-dimensional diatomic granular crystals,” *Phys. Rev. E.*, vol. 82, no. 056604, 2010.
- [149] N. Boechler, G. Theocharis, and C. Daraio, “Bifurcation-based phononic switching and rectification,” *Nature Mater. (under review)*, 2011.
- [150] F. Duang and J. Guojin, *Intoduction to Condensed Matter Physics: Volume 1*. Singapore: World Scientific Publishing, 2005.
- [151] N. Boechler and C. Daraio, “An experimental investigation of acoustic band gaps and localization in granular elastic chains,” in *Proceedings of the 22nd Biennial Conference on Mechanical Vibration and Noise VIB-5*, (San Diego, CA, USA), ASME, 2009.
- [152] S. A. Kiselev, S. R. Bickham, and A. J. Sievers, “Anharmonic gap modes in a perfect one-dimensional diatomic lattice for standard two-body nearest-neighbor potentials,” *Phys. Rev. B*, vol. 48, no. 13508, 1993.
- [153] R. Livi, M. Spicci, and R. S. MacKay, “Breathers on a diatomic FPU chain,” *Nonlinearity*, vol. 10, no. 1421, 1997.

- [154] P. Maniadis, A. V. Zolotaryuk, and G. P. Tsironis, “Existence and stability of discrete gap breathers in a diatomic Fermi–Pasta–Ulam chain,” *Phys. Rev. E*, vol. 67, no. 046612, 2003.
- [155] G. James and M. Kastner, “Bifurcations of discrete breathers in a diatomic Fermi-Pasta-Ulam chain,” *Nonlinearity*, vol. 20, no. 631, 2007.
- [156] T. Dauxois and M. Peyrard, “Energy localization in nonlinear lattices,” *Phys. Rev. Lett.*, vol. 70, no. 3935, 1993.
- [157] T. Dauxois, R. Khomeriki, F. Piazza, , and S. Ruffo, “The anti-FPU problem,” *Chaos*, vol. 15, no. 015110, 2005.
- [158] A. V. Gorbach and M. Johansson, “Discrete gap breathers in a diatomic klein-gordon chain: Stability and mobility,” *Phys. Rev. E*, vol. 67, no. 066608, 2003.
- [159] S. Aubry, “Discrete breathers: Localization and transfer of energy in discrete hamiltonian nonlinear systems,” *Physica D*, vol. 216, no. 1, 2006.
- [160] A. Bikaki, N. Voulgarakis, S. Aubry, and G. Tsironis, “Energy relaxation in discrete nonlinear lattices,” *Phys. Rev. E*, vol. 59, no. 1234, 1999.
- [161] R. Reigada, A. Sarmiento, and K. Lindenberg, “Energy relaxation in nonlinear one-dimensional lattices,” *Phys. Rev. E*, vol. 64, no. 066608, 2001.
- [162] R. Reigada, A. Sarmiento, and K. Lindenberg, “Energy relaxation in Fermi-Pasta-Ulam arrays,” *Physica A*, vol. 305, no. 467, 2002.
- [163] E. Kenig, B. A. Malomed, M. C. Cross, and R. Lifshitz, “Intrinsic localized modes in parametrically driven arrays of nonlinear resonators,” *Phys. Rev. E*, vol. 80, no. 046202, 2009.
- [164] O. Morsch and M. Oberthaler, “Dynamics of Bose-Einstein condensates in optical lattices,” *Rev. Mod. Phys.*, vol. 78, no. 179, 2006.

- [165] J. Cuevas, L. Q. English, P. G. Kevrekidis, and M. Anderson, “Discrete breathers in a forced-damped array of coupled pendula: Modeling, computation, and experiment,” *Phys. Rev. Lett.*, vol. 102, no. 224101, 2009.
- [166] Y. B. Jeon, R. Sood, J. H. Jeong, and S. G. Kim, “Mems power generator with transverse mode thin film PZT,” *Sensors and Actuators A: Physical*, vol. 122, no. 16, 2005.
- [167] F. Cottone, H. Vocca, and L. Gammaitoni, “Nonlinear energy harvesting,” *Phys. Rev. Lett.*, vol. 102, no. 080601, 2009.
- [168] H. A. Sodano, G. Park, and D. Inman, “Estimation of electric charge output for piezoelectric energy harvesting,” *Strain*, vol. 40, no. 49, 2004.
- [169] R. F. Wallis, “Effect of free ends on the vibration frequencies of one-dimensional lattices,” *Phys. Rev.*, vol. 105, no. 540, 1957.
- [170] M. G. Cottam and D. R. Tilley, *Introduction to Surface and Superlattice Excitations*. Cambridge, UK: Cambridge University Press, 1989.
- [171] P. B. Allen, S. Aubin, and R. B. Doak, “Surface phonons and other localized excitations,” *Am. J. Phys.*, vol. 68, no. 3, 2000.
- [172] D. K. Campbell, P. Rosenau, and G. Zaslavsky, “Introduction: The Fermi–Pasta–Ulam problem—The first fifty years,” *Chaos*, vol. 15, no. 015101, 2005.
- [173] J. Ford, “The Fermi–Pasta–Ulam problem: Paradox turns discovery,” *Phys. Rep.*, vol. 213(5), no. 273, 1992.
- [174] A. V. Gorbach and M. Johansson, “Gap and out-gap breathers in a binary modulated discrete nonlinear Schrodinger mode,” *Eur. Phys. J. D.*, vol. 29, no. 77, 2004.
- [175] D. V. Skryabin, “Energy of internal modes of nonlinear waves and complex frequencies due to symmetry breaking,” *Phys. Rev. E*, vol. 64, no. 055601(R), 2001.

- [176] J. L. Marín and S. Aubry, “Finite size effects on instabilities of discrete breathers,” *Physica D*, vol. 119, no. 163, 1998.
- [177] S. Flach and A. Gorbach, “Discrete breathers in Fermi-Pasta-Ulam lattices,” *Chaos*, vol. 15, no. 015112, 2005.
- [178] C. Baesens, S. Kim, and R. S. MacKay, “Localised modes on localised equilibria,” *Physica D*, vol. 113, no. 242, 1998.
- [179] M. Johansson and S. Aubry, “Growth and decay of discrete nonlinear Schrödinger breathers interacting with internal modes or standing-wave phonons,” *Phys. Rev. E*, vol. 61, no. 5864, 2000.
- [180] A. M. Morgante, M. Johansson, S. Aubry, and G. Kopidakis, “Breatherphonon resonances in finite-size lattices: ‘phantom breathers’?,” *J. Phys. A*, vol. 35, no. 4999, 2002.
- [181] I. M. Lifschitz and A. M. Kosevich, “The dynamics of a crystal lattice with defects,” *Rep. Progr. Phys.*, vol. 29, no. 217, 1966.
- [182] M. Brodsky and G. Lucovsky, “Infrared reflection spectra of $ga_{1-x}in_xas$: A new type of mixed-crystal behavior,” *Phys. Rev. Lett.*, vol. 21, no. 990, 1968.
- [183] E. J. Hinch and S. Saint-Jean, “The fragmentation of a line of balls by an impact,” *Proc. R. Soc. Lond. A*, vol. 455, no. 3201, 1999.
- [184] J. B. Hong and A. G. Xu, “Nondestructive identification of impurities in granular medium,” *App. Phys. Lett.*, vol. 81, no. 4868, 2002.
- [185] M. Manciu, S. Sen, and A. J. Hurd, “The propagation and backscattering of soliton-like pulses in a chain of quartz beads and related problems. (II). Backscattering,” *Physica A*, vol. 274, no. 607, 1999.
- [186] X. F. Li, X. Ni, L. Feng, M. H. Lu, C. He, and Y. F. Chen, “Tunable unidirectional sound propagation through a sonic-crystal-based acoustic diode,” *Phys. Rev. Lett.*, vol. 106, no. 084301, 2011.

- [187] M. Terraneo, M. Peyrard, and G. Casati, “Controlling the energy flow in non-linear lattices: a model for a thermal rectifier.,” *Phys. Rev. Lett.*, vol. 88, no. 094302, 2002.
- [188] B. Li and L. Wang, “Phononics gets hot,” *Phys. World*, vol. 21, no. 2729, 2008.
- [189] C. W. Chang, D. Okawa, A. Majumdar, and A. Zettl, “Solid-state thermal rectifier,” *Science*, vol. 314, no. 1121, 2006.
- [190] W. Kobayashi, Y. Teraoka, and I. Terasaki, “An oxide thermal rectifier,” *Appl. Phys. Lett.*, vol. 95, no. 171905, 2009.
- [191] L. Wang and B. Li, “Thermal logic gates: computation with phonons,” *Phys. Rev. Lett.*, vol. 99, no. 177208, 2007.
- [192] M. Eichenfield, J. Chan, R. M. Camacho, K. J. Vahala, and O. Painter, “Optomechanical crystals,” *Nature*, vol. 462, no. 78, 2009.